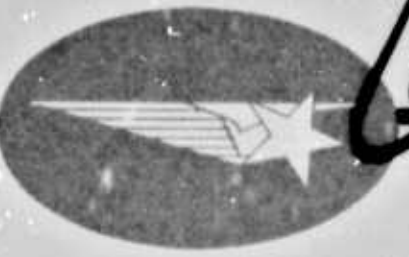


6-75-65-27 • JUNE 1965

6-75-65-27

AD6222874



METAL DIFFUSION
IN
PYROLYTIC GRAPHITE

DDC

NOV 8 1965

TSA

by
MARTIN LEWIS HAMMOND

DISTRIBUTION OF THIS
DOCUMENT IS UNLIMITED

GENERAL SOURCE
FOR FEDERAL SCIENTIFIC AND
TECHNICAL INFORMATION

6-60 3125 207 as

ARCHIVE COPY

SEARCHING COPY

METAL DIFFUSION
IN
PYROLYTIC GRAPHITE

A DISSERTATION
SUBMITTED TO THE DEPARTMENT OF MATERIALS SCIENCE
AND THE COMMITTEE ON THE GRADUATE DIVISION
OF STANFORD UNIVERSITY
IN PARTIAL FULFILLMENT OF THE REQUIREMENTS
FOR THE DEGREE OF
DOCTOR OF PHILOSOPHY

By

Martin Lewis Hammond

June 1965

DISTRIBUTION OF
THIS DOCUMENT IS
UNLIMITED

FOREWORD

**This report is identical to the dissertation submitted to the
Materials Science Department of Stanford University by the author
in partial fulfillment of the requirements for the degree of Doctor
of Philosophy.**

ABSTRACT

The diffusion coefficients of Nb-95 in PG were measured between 1450 and 1950°C in three different types of PG which were chosen to represent substrate nucleated, combination substrate and regeneratively nucleated, and regeneratively nucleated microstructures. The diffusion coefficients parallel and perpendicular to the deposition surface were determined in as-deposited and partially graphitized PG. Autoradiography was used to observe the distribution of diffusing atoms. The structure of the PG was characterized by the application of many techniques of metallography, x-ray diffraction, small angle scattering of x-rays, and density determinations. A mathematical analysis of diffusion in layered structures was made and correlations between the structure and diffusion parameters noted.

The activation energies for Nb diffusion in PG depended only upon direction and were independent of microstructure and state of graphitization. The activation energy for Nb diffusion parallel to the deposition plane was 96.2 kcal/mole and that perpendicular to it was 73.1 kcal/mole. The pre-exponential factors for a given direction differed only slightly for the various PG's used in this study; these factors were altered by the graphitizing heat-treatment. Parallel to the deposition plane, the pre-exponential factors were all approximately $3.2 \times 10^2 \text{ cm}^2/\text{sec}$ for the as-deposited PG's and $1.8 \times 10^3 \text{ cm}^2/\text{sec}$ for the heat-treated PG's. For diffusion perpendicular to the deposition plane, these

factors were approximately $1.2 \times 10^{-2} \text{ cm}^2/\text{sec}$ for the as-deposited PG's and $6.5 \times 10^{-3} \text{ cm}^2/\text{sec}$ for the heat-treated material. Autoradiography demonstrated that diffusion perpendicular to the layer planes occurs in the primary cone boundaries while the radioactivity is uniformly distributed in the autoradiographs taken for diffusion parallel to deposition plane.

Diffusion mechanisms within the crystallites were rejected on the bases of valence and relative atom size. An examination of mechanisms external to the crystallites, combined with an analysis of the relative values of the pre-exponential factors, revealed that the fundamental jump distance for diffusion parallel to the deposition plane is the crystallite diameter, while the jump distance perpendicular to the deposition plane is the layer plane separation distance. This model was confirmed quantitatively by applying the results of an analysis of diffusion in the primary cone boundaries and by utilizing elementary interstitial diffusion theory.

In another set of experiments with Re-PG diffusion couples, a metastable carbide of Re was discovered. The carbide has a simple cubic crystal structure with a unit cell edge of 2.8+ Å and reacts with Re to form a eutectic at $\sim 2000^\circ\text{C}$ ($\pm 200^\circ\text{C}$).

ACKNOWLEDGMENTS

The author wishes to thank the following people who contributed to the success of this dissertation in many ways:

Professor D.A. Stevenson and Dr. R.H. Bragg for their advice and guidance as joint advisors to this investigation.

Professors J.C. Shyne and V.G. Macres for their comments and discussions concerning the dissertation.

Drs. M.A. Steinberg and E.C. Burke for their generous support.

All of his friends of the Lockheed Research Laboratory and in the Department of Materials Science of Stanford University. Individuals who contributed to specific areas in the dissertation are noted in the text.

The Lockheed Missiles & Space Company and the staff of the Graduate Study Program for supporting his studies at Stanford University.

Messrs. C.O. Mathews and E.S. Wright for their support, which was instrumental in permitting the author's participation in the LMSC Graduate Study Program.

Mr. C.M. Packer for proof-reading the manuscript.

Mr. M. Ingram for his assistance on all phases of the editorial tasks in preparing the manuscript for publication.

Finally, the author thanks his wife and family who patiently waited while always offering encouragement.

This work was supported by the Independent Research Program of the Lockheed Missiles & Space Company.

TO

THE MEMORY OF

MY FATHER

TABLE OF CONTENTS

	Page
ABSTRACT	iii
ACKNOWLEDGMENTS	v
TABLES	xi
ILLUSTRATIONS	xii
 CHAPTER	
I INTRODUCTION	1
A. Preliminary Comments	1
B. Technological Aspects of PG	2
C. Scientific Aspects of PG	3
D. Brief Review of Diffusion in PG	4
E. Structure of PG	5
F. Description of Research Problem	6
II REVIEW OF DIFFUSION IN GRAPHITES	7
A. Introduction	7
B. Theoretical Analyses of Self-Diffusion in Graphite	7
C. Carbon Self-Diffusion - Experimental Data	12
D. Impurity Diffusion	13
E. Contributions of Wolfe, McKenzie and Borg	19
F. Contribution of Hennig	22
G. Summary	23

Chapter		Page
III	STRUCTURE OF PYROLYTIC GRAPHITE	25
	A. Introduction	25
	B. Structural Chemistry of Carbon	25
	C. Manufacture of PG	31
	D. Metallographic Structure of PG	32
	E. X-Ray Structure of PG	34
	F. Other Structural Parameters	41
	G. Graphitization in PG	43
	H. Summary	45
IV	EXPERIMENTAL APPROACH	47
	A. Statement of Problem	47
	B. Program Summary	47
	C. Choice of PG	49
	D. Choice of Metal	50
	E. Summary	51
V	EXPERIMENTS WITH RHENIUM AND PYROLYTIC GRAPHITE	53
	A. Introduction	53
	B. Phase Reactions of Re with PG	53
	C. Diffusion Studies with Re	60
VI	EXPERIMENTAL PROCEDURES	64
	A. Structural Characterizations	64
	1. Microstructure	64

Chapter		Page
	2. Transmission Electron Microscopy	65
	3. X-Ray Diffraction Studies	65
	4. Small Angle Scattering	70
	5. Other Structural Parameters	71
	B. Diffusion Measurements	71
	1. Method of Measuring Diffusion Coefficients	71
	2. Sample Preparation Prior to Diffusion	73
	3. Furnace Description and Annealing Procedure	75
	4. Sectioning Techniques	78
	5. Autoradiography	81
VII	EXPERIMENTAL RESULTS – STRUCTURE	82
	A. Microstructure	82
	B. Transmission Electron Microscopy	85
	C. X-Ray Structure	92
	D. Small Angle Scattering	103
	E. Other Structural Parameters	109
	F. Summary	109
VIII	EXPERIMENTAL RESULTS – DIFFUSION	112
	A. General Behavior of Data	112
	B. Computation of Diffusion Coefficients	114
	C. Measured Diffusion Coefficients	119

Chapter		Page
	D. Temperature Dependence of Diffusion Coefficients	121
	E. Autoradiography	126
IX	DISCUSSION	132
	A. Summary of Results	132
	B. Correlation With Structure	133
	C. Possible Mechanisms for Metal Diffusion in PG	137
	D. Model for Diffusion of Metals in PG	143
	E. Grain Boundary Diffusion Theories	152
	F. Discussion of the Model and Comparison with the Data of Wolfe, McKenzie and Borg	153
	G. Relevance of Model to Diffusion in Other Graphites and Pyrolytic Graphites	157
	H. Comments Concerning Diffusion-Alloying in PG	160
X	SUMMARY	162
	APPENDIX – Mathematics of Diffusion in Layered Structures	168
	REFERENCES	185

TABLES

	Page
1 Calculated Activation Energies for Carbon Self-Diffusion	9
2 Summary of Studies of the Migration of Fission Fragments in Graphites	16
3 Summary of the Data of Wolfe, McKenzie and Borg	21
4 Estimates of Activation Energies for Various Diffusion Processes in Graphite	24
5 Comparison of Methods of Computing Crystallite Thicknesses in PG	39
6 X-Ray Density as a Function of Interlayer Spacing and Comparison with Experiment	43
7 List of Diffusion Couples of Re vs PG and Other Graphites	54
8 Compilation of Discontinuous Debye-Scherrer Lines Obtained from Material Taken from Re vs PG Diffusion Couples	57
9 Stacking Error Probabilities for PG Used in This Study	95
10 Crystallite Sizes for PG Used in This Study	96
11 Summary of Preferred Orientation Data	101
12 Comparison of Observed Densities and Densities Computed from Observed Interlayer Spacings	110
13 Diffusion Coefficients for Nb-95 in Various Types of PG	120
14 Temperature Dependence of Diffusion Coefficients	124
15 Summary of Structure and Diffusion Data	134
16 Comparison of Data from This Investigation with Those of Wolfe, McKenzie, and Borg	154

ILLUSTRATIONS

Figure		Page
1	Crystal Structure of Ideal Hexagonal Graphite	27
2	Interlayer Spacing vs Stacking Error Probability for Graphitic Carbons	38
3a	Melted Structure in Rhenium-PG Diffusion Couple. Polarized Light. 1000X.	55
3b	Reaction Zone in Rhenium-PG Diffusion Couple. Bright Field. 500X.	55
4	Schematic Concentration Profiles for Re-186 Diffusion in PG	62
5	Photomicrographs at 10X Magnification of As-Deposited PG's Used in Study	83
6	Photomicrographs at 10X Magnification of Heat-Treated PG's Used in Study	84
7	Photomicrographs Parallel to Deposition Plane of R165 PG	86
8	Photomicrographs Perpendicular to Deposition Plane of R165 PG	87
9	Photomicrographs Parallel to Deposition Plane of R277 PG	88
10	Photomicrographs Perpendicular to Deposition Plane of R277 PG	89
11	Photomicrographs Parallel to Deposition Plane of R1 PG	90
12	Photomicrographs Perpendicular to Deposition Plane of R1 PG	91
13	Transmission Electron Micrographs of R277 PG Taken Near Beginning of Nb Concentration Gradient	93
14	Uncorrected <u>hk</u> Bands in PG	97

Figure		Page
15	0002 Pole Figures for R165 and R1 PG	99
16	0002 Pole Figures for R277 PG	100
17	Orientation Dependence of Stacking Error Probability	102
18	Small Angle Scattering by R165 PG.	105
19	Guinier Analysis of Small Angle Scattering Curves.	107
20	Typical Composition Profiles Perpendicular and Parallel to Deposition Plane	113
21	Behavior of Instantaneous Source (a) and Constant Surface Composition (b) Solutions to Fick's Diffusion Laws for Semi-Infinite Solid	116
22	Arrhenius Plots of Nb Diffusion Coefficient in PG. Diffusion Parallel to Deposition Plane	122
23	Arrhenius Plots of Nb Diffusion Coefficient in PG. Diffusion Perpendicular to Deposition Plane	123
24	Direct Comparison of Structure and Autoradiographs Parallel to Deposition Surface for R165 and R1 As-Deposited PG	127
25	Direct Comparison of Structure and Autoradiographs Parallel to the Deposition Surface for R277 PG, As-Deposited and Heat-Treated	128
26	Comparison of Structure and Autoradiography Perpendicular to the Deposition Surface for R277 PG, As-Deposited and Heat-Treated	130
27	Idealized Model for Diffusion Perpendicular to Layer Planes in Pyrolytic Graphite	169
28	Mathematical Model for Diffusion Perpendicular to Layer Planes in Pyrolytic Graphite	170

Chapter I

INTRODUCTION

A. Preliminary Comments

Massive pyrolytic graphite (PG), a recent development in the field of chemical vapor deposition (1, 2) has aroused considerable interest because of its high-temperature properties. PG exhibits a very high tensile strength at temperatures in excess of 3000°C (3, 4, 5), is highly anisotropic in its electrical (6) and thermal (3) conduction properties, and has nearly theoretical density (1). The major limitations of PG for high temperature service are its low oxidation resistance at high temperature and its low shear stress parallel to the plane of the deposit. Efforts to alleviate these problems and to produce material with controllable electrical properties have been made by co-depositing metals with PG (7, 8); to date, however, no other methods have been investigated. Although the diffusion of metals in PG could be important relative to its behavior in high temperature environments, no studies of this kind had been reported at the time this investigation began.

In addition to the above, PG possesses a unique and interesting anisotropic structure, and many techniques have been developed recently to characterize it. Thus, diffusion studies in PG are of value from both practical and theoretical viewpoints. The practical value of such studies lies in the possibility of

diffusion-alloying PG to improve its oxidation and mechanical properties and to alter its electrical properties. The theoretical value lies in studying diffusion in this unique anisotropic structure, using the recently developed techniques for structural characterization to further the understanding of the structure of PG and to determine the underlying mechanisms of metal diffusion in PG.

B. Technological Aspects of PG

Graphite has a sublimation temperature considerably in excess of 3000°C, the triple point occurring at approximately 3700°C and 105 Kg/mm² (9, 10, 11). The high sublimation temperature combined with a very high degree of covalent bonding within the layers makes graphite a highly refractory material, i.e., a material that retains its strength and is capable of providing service at high temperature. Normal synthetic graphites begin to lose strength around 2500°C (3), but PG actually begins to increase in tensile strength parallel to the layer planes at this temperature (3, 5, 12). Furthermore, PG is anisotropic in all of its properties, being a good conductor of electricity and heat parallel to its layer planes and a fairly good insulator perpendicular to them (3).

These highly refractory and highly anisotropic properties make PG a good material for many high temperature uses, including rocket nozzles, and re-entry vehicles. Nuclear applications include such items as control rod housings (12), structural members in high temperature nuclear reactors, and coatings on small particles of reactor fuel (13, 14).

The diffusion of metals in PG can play an important role in many of the above applications; for example, it may be possible to diffusion-alloy PG with metals to alter its mechanical and oxidation properties. It has been observed that high temperature deformation of PG occurs by crystallites sliding past each other (5) and that oxidation of graphite occurs principally at the edges of the crystallites (15). One of the conclusions of this investigation is that the diffusion of metals in PG takes place along the crystallite surfaces, suggesting that the high temperature properties of PG could be improved by diffusion alloying. A proper selection of metal could interfere with both crystallite sliding and the peripheral oxidation mechanisms to improve PG's performance at high temperature. As noted above, alloying of PG by co-deposition of metals is presently being accomplished (7, 8).

C. Scientific Aspects of PG

PG is a unique material. It offers a high degree of anisotropy in both defect structure and properties and nearly theoretical density with very low porosity and permeability. Furthermore, it is the closest approximation presently available to large single crystals of graphite. The layer structure of graphite and the method of production make for an unusual anisotropic defect structure which will be important in mass transfer as well as many other properties.

This structure, which will be discussed fully in Chapter III, is unique to PG. However, some of the conclusions reached in this study will also apply to diffusion in other oriented, layer structures such as BN and Bi_2Te_3 . Diffusion

in BN has not been investigated, but its structure is very similar to that of graphite (9). The diffusion of copper in single crystal Bi_2Te_3 was found to be highly anisotropic (16), and impurity diffusion in oriented, polycrystalline material might well behave in the same fashion as that in PG.

D. Brief Review of Diffusion in Graphites

Diffusion in graphites will be reviewed in more detail and referenced in Chapter II; however, a brief summary will be given here to acquaint the reader with the literature. Carbon self-diffusion in an ideal graphite lattice has been treated theoretically and C-14 tracer diffusion experiments have been carried out, with relatively little success, on natural single crystals and bulk synthetic graphite. The migration of carbon atoms displaced by radiation damage has been studied extensively and some data on carbon diffusion have been derived from electron microscopy studies on quenched-in dislocation loops in graphite.

There have been several investigations of the migration of fission products from individual graphite fuel cells, but these experiments do not generally lend themselves to unequivocal interpretation because the graphites consist of varying amounts of "amorphous" and "crystalline" carbon with widely varying orientations and also are subject to radiation damage. These factors, combined with the presence of a large number of elements in differing amounts, make a fundamental interpretation regarding the diffusion mechanisms impossible.

Under more controlled conditions, the diffusion rates of U, B, and Th in various forms of carbon have been studied and, recently, an extensive study of

the diffusion of Ag, Ni, U, Th, and Ra in PG and other forms of carbon was made. To date, this latter study is the only investigation of metal diffusion in graphite using standard radioactive tracer techniques and resulting in reasonably clear interpretations. Although this study showed how the diffusion kinetics varied for different atoms, the role of the structure of the PG and graphites in the diffusion process was not investigated except that it was shown that the diffusion rate of Ni-63 in extremely well annealed PG is quite small compared to that in as-deposited PG.

E. Structure of PG

The structure of PG has recently been investigated in some detail, as will be discussed in Chapter III. X-ray diffraction yields information concerning the degree of perfection within the crystallites, their size in the $\langle a \rangle$ and $\langle c \rangle$ directions, the degree of preferred orientation, and the variation of crystallite size and perfection with orientation relative to the deposition plane normal. Small angle scattering (SAS) provides information concerning the void size and distribution and transmission electron microscopy can be used to observe small aggregates of crystallites. Optical microscopy provides information concerning the manner in which the PG has nucleated and grown during its manufacture and, because of the optical anisotropy of PG, the relative orientation of major structural features can be determined. Density measurements and externally connected porosity measurements permit a comparison with the theoretical x-ray density and thereby provide a link between the x-ray diffraction and SAS information. Techniques have been developed for all of the above measurements and

their combined application to a particular PG results in a very detailed description of the structure that can be correlated with many properties.

F. Description of Research Problem

This program was initiated to examine the possibility of diffusion-alloying PG and to determine the role of structure in metal diffusion in PG

The purpose of the investigation was to determine how the structure of PG affects the diffusion of metal atoms in PG. To do this, three different kinds of PG were selected and the diffusion coefficient of Nb-95 was measured perpendicular and parallel to the deposition plane, in the as-deposited and in one heat-treated condition for each of the PG's. The structure of the PG's was characterized by analysis of x-ray diffraction and small angle scattering data, by optical and electron microscopy, and by density determinations. Correlations with the defect structure of the PG deposits and the changes of this structure with heat-treatment were made with the observed diffusion coefficients in the two principal directions.

Chapter II

REVIEW OF DIFFUSION IN GRAPHITES

A. Introduction

Carbon self-diffusion has been studied both theoretically and experimentally, while high temperature impurity diffusion in graphites has been examined only experimentally. The different theoretical treatments of carbon self-diffusion are in fair agreement, but the experimental determinations of self-diffusion are open to question. In addition, most of the high temperature impurity diffusion studies have very questionable value. Many of these investigations have been concerned with the migration of fission fragments in poorly characterized graphites under very complex conditions; the few less complicated experiments are marked by a considerable lack of data or rather questionable interpretations. Only the recent data of Wolfe, McKenzie, and Borg (17) and possibly that of Hennig (18) warrant serious discussion regarding the mechanisms of diffusion in graphites; the other data, however, will be reviewed here for general reference.

B. Theoretical Analyses of Self-Diffusion in Graphite

Carbon self-diffusion in graphite has been theoretically analyzed by Dienes (19). Using arguments based on the variation of bond strength with distance, he calculated the activation energies of self-diffusion for the layer

vacancy mechanism, the direct interchange of carbon atoms within a layer plane, and the interlayer or interstitial migration mechanism. Dienes defines interstitial migration as the motion of atoms between the layers of the graphite lattice and not as passage through the hexagon rings. Although physically there is a hole in the center of each hexagon, the electronic interactions probably make this a very high energy path. A better term for the motion of atoms between the layers would be "interlayer migration" which will be used here to describe any atoms residing between the layers. The calculated activation energy for the interlayer diffusion mechanism included a term for removing an atom from the edge of the layer and a term involving repulsive force interaction of the interlayer atom with the layers. The repulsive force was represented as an exponential function of distance and the parameters were evaluated using experimentally determined elastic constants.

All of Dienes' calculations were based on early data by Pauling (20) concerning the dependence of the bond strength on the carbon-carbon equilibrium distance for singly bonded, resonance bonded, and doubly and triply bonded carbon atoms. Kanter (21, 22) pointed out that more recent data reported by Coulson (23) on the bond strength and carbon-carbon distance raise Dienes' value of 79.6 kcal/mole for the bond energy in graphite (C-C distance of 1.42A) to 113 kcal/mole. Table 1 contains the results of Dienes' calculations, corrected by Kanter (21). The very high value for the formation of an interlayer carbon atom should be noted. More recently, Dienes (24) has estimated the energy for motion of an interlayer carbon atom to be about 2.6 kcal/mole.

Table 1
**CALCULATED ACTIVATION ENERGIES FOR CARBON
 SELF-DIFFUSION IN GRAPHITE^(a)**

<u>Process</u>	<u>Energy (kcal/mole)</u>
Formation of vacancy within hexagon layer	170
Motion of vacancy within layer	93
Total energy for vacancy mechanism	263
Direct interchange within a layer	113
Formation of an interlayer interstitial carbon atom	467
Motion of an interlayer carbon atom	not discussed

(a) Originally calculated by Dienes (19) and corrected by
 Kanter (21, 22)

The energies of formation and motion of interlayer C and Xe in the graphite lattice have been calculated by Iwata et al. (25) using, as a model of the graphite layers, thin elastic sheets subjected to bending due to the presence of the interlayer atom. Their results are as follows:

<u>Process</u>	<u>Activation Energy - kcal/mole</u>
Formation of interlayer carbon atom	57.6
Formation of interlayer xenon atom	346
Motion of interlayer carbon atom	0.368
Motion of interlayer xenon atom	0.691

The value obtained by Iwata et al. for forming the carbon interlayer atom differs considerably from that by Dienes. This difference is partly due to the fact that Iwata did not include the energy to remove an atom from the surface and partly because Iwata's calculations allow for relaxation of the layer sheets about the interlayer atom while Dienes' calculations do not. Experimental determination of these energies should be possible by observing the annealing behavior of neutron-irradiated graphite; however, this behavior is quite complex (26, 27). Many different processes occur during the annealing of radiation-damaged graphite and interpretation of the change of a property with time at temperature is not simple (27). In any case, the annealing of relatively light radiation damage can be accomplished below about 200°C , indicating that the simplest types of radiation damage have rather low migration energies. Using a model based on the migration of single interlayer carbon atoms produced by neutron irradiation, Schweitzer (28) determined the activation energy for motion of these atoms to be 1.6 ± 0.1 kcal/mole between 77 and 490°K .

The energies for the formation and motion of layer vacancies have been estimated by Baker and Kelly (29) using observations with the electron microscope of dislocation loops formed in graphite single crystals. The loops were formed by quenching the crystals from 3000°C and then annealing between 1200 and 1400°C at which temperatures the excess vacancies should coalesce and condense into basal plane dislocation loops. With arguments based on the distance vacancies must travel to coalesce into dislocation loops, Baker and Kelly

estimated the vacancy formation energy to be about 78 kcal/mole and the motion energy to be 69 kcal/mole, giving an activation energy for self-diffusion of 150 kcal/mole. Wooley (30) has taken the ideas of Baker and Kelly somewhat further and calculated the energy to form a vacancy-interlayer atom pair in graphite as 138 ±55 kcal/mole. Several configurations such as interlayer clusters were also examined. In addition, Wooley cites a value for the motion energy of an interlayer carbon atom of less than 9 kcal/mole.

Hennig (31) was unable to reproduce the results given by Baker and Kelly and came to the conclusion that the lower limit for the formation of a vacancy should be about 140 kcal/mole. Hennig's observations were supported somewhat by theoretical calculations made by Coulson and co-workers (32, 33) on the energy to form layer vacancies. Their calculations, based on electron configurational energies in a carbon macro-molecular layer with and without vacancies, gave 246 kcal/mole for the energy to form a single vacancy (32). They further showed that a divacancy is more stable than two single vacancies by 110 kcal/mole of divacancy (33).

To summarize, calculations and estimates of the energy to form a single layer vacancy in graphite vary from 78 to 246 kcal/mole with the more likely value being in the middle of the range. The energy to move a vacancy is estimated to be between 69 and 93 kcal/mole. Estimates of the energy to form an interstitial carbon atom range from 58 to 467 kcal/mole, but the lower value is more probable because it takes relaxation into account and does not include a term for removing an atom from one of the layers. The energy of an atom between the edges of two crystallites is probably rather high, and the energy to remove

it from its environment would not be as great as removing an atom from the edge of a layer. The formation of an interlayer foreign atom, such as Xe, requires about 350 kcal/mole, and the energy for motion of an interlayer atom, C or Xe, is very small, being less than 10 kcal/mole and more likely less than 1 kcal/mole.

There are no specific theoretical treatments for the diffusion of atoms other than carbon in the graphite lattice except that given for Xe. Many metals can enter into directional bonds with carbon and other atoms, as in the case of the metal-organic compounds (34); however, the large size of nearly all metal atoms would prevent diffusion by direct substitution and direct vacancy-atom exchange in the graphite lattice. Boron is the only "metallic" atom that might be expected to enter the graphite lattice substitutionally.

C. Carbon Self Diffusion - Experimental Data

Two studies of tracer self-diffusion in graphite have been reported. Feldman et al. (35) studied tracer self diffusion in National Carbon AUF grade graphite by depositing a slurry of carbon and water, containing C-14, on the ends of small graphite rods and annealing for various times near 2000°C. The cylindrical surfaces of the rods were machined before and after annealing and sections along the rod axis were cut with a microtome. It was not clear whether the data were best interpreted as log concentration vs. distance to the first or second power. After some justifications regarding activation energies, the data were interpreted on the basis of an analysis of simultaneous grain boundary

and volume diffusion proposed by Fisher (36). Assuming a value for the activation energy for volume diffusion of 90 kcal/mole, Feldman et al. obtained 75.4 kcal/mole as the activation energy for grain boundary diffusion.

Kanter (21, 22) studied tracer self diffusion in natural graphite crystals by heating them in an atmosphere of radioactive carbon monoxide and then measuring the concentration profile by a controlled burning process. The profiles could not be measured conveniently in any other way due to the small size of the natural graphite crystals (~1mm diameter). Experiments utilizing conditions that approximated the instantaneous source solution to the diffusion equations did not yield meaningful information, but experiments approximating a constant surface composition produced seemingly better data: an activation energy of 163 kcal/mole was determined for layer plane diffusion in graphite, based on the assumption that carbon self-diffusion occurs only perpendicular to the c-axis of the crystal.

D. Impurity Diffusion

Investigation of impurity diffusion in graphites includes studies of the formation of lamellar compounds, migration of fission fragments in graphite, and direct measurement of the diffusivity, using different methods for measuring the concentration profiles produced by diffusion.

A phenomenon related to impurity diffusion is the formation of lamellar compounds with graphite in which foreign atoms enter into the graphite lattice at certain position between the layers (9, 37). The process of entering the lattice is

termed intercalation and such lamellar compounds are also termed intercalation compounds. Formation of these compounds does not have a direct bearing on high temperature diffusion in graphites but these compounds will be discussed briefly for the sake of completeness. A great many elements and compounds will intercalate the layer structure of graphite and form lamellar or intercalation compounds. The formation of the compounds requires the migration or diffusion of the element or compound into the graphite lattice; however, the process is complicated by the formation of the new compound and therefore kinetic studies of the formation of these compounds would not be directly applicable to the study of metal diffusion in graphites. Lamellar compounds can be formed directly with the alkali metals when they are molten, and with the halogens when heated to 400 to 500°C (37). In addition, aqueous solutions of many metal chlorides, oxides, and sulfides (38) will intercalate the graphite structure. Although the process of lamellar compound formation is not well understood, one theory is that the metal atom must be sufficiently ionized to accept a π electron from the graphite before it can enter the region between the layers (38). Two phenomena occur with the formation of lamellar compounds. The first is a large expansion of the lattice (9) perpendicular to the layer planes which is accompanied with some visible swelling of the graphite body. The second is the marked tumescence (9) produced if the intercalated graphite structure is heated to a few hundred degrees C. Expansions of ten fold are not uncommon.

Studies of the migration of fission fragments in graphite are all based upon measuring the fraction of activity remaining for any or all the fission fragments. These studies can be divided into two groups, those in which only the concentration vs. time at temperature data are reported and those in which the authors thought the data were of sufficient quality to warrant computing activation energies. In the first group (39, 40, 41) the loss of Sr, Y, Zr, Nb, Mo, Ru, Rh, Te, I, Cs, Ba, Ce, and most of the actinides and lanthanides was measured for various times at temperatures between 900 and 2600°C. The general conclusion was that the more volatile, lower melting elements migrated out of the graphite rather rapidly and the more refractory metals Zr, Nb, Mo, Ru, Rh, and U demonstrated very little tendency to leave graphite when heated as long as 10 minutes at 2400°C.

Table 2 contains a summary of the studies of the migration of fission fragments in graphite in which the authors felt they could determine an activation energy. Rates for the Arrhenius plots were determined by a variety of methods, the most common one being to plot the log of the time required to reach a certain relative composition vs. reciprocal temperature. Although the numbers given in these investigations have some engineering utility, they are of little use in determining the fundamental mechanisms of diffusion in graphite because of the complicated and varied structure of the graphite used and the presence of many different chemical species.

Table 2
SUMMARY OF STUDIES OF THE MIGRATION OF
FISSION FRAGMENTS IN GRAPHITE

Diffusing Species	Apparent Activation Energy, Q (kcal/mole)	Reference	Remarks
Total Activity	20.7	42	Q varied with temperature, being lower at higher temperatures
Ba-140	68.2		
Sr-189	26.4		
As-77	32	43	
Br-83	27		
Pd-109, 112	9		
Cd-115	30		
Sb-127	50		
Te-18	18		
I-131, 133	42		
Xe-135	49	44	$D_o = 3 \times 10^{-5}$
I-131	46 - 49	45	
Cs	18	46	$D_o \sim 10^{-2}$
Sr	10		$D_o \sim 10^{-4}$
Ba	9		$D_o \sim 10^{-4}$
Xe-135	23	47	Natural Graphite 1
Xe-135	23		Natural Graphite 2
Xe-135	27		Natural Graphite 3
Xe-135	23		Synthetic Graphite
Xe-135	49		Amorphous Carbon

The remaining impurity diffusion studies discussed in this section were made without the additional complications associated with the presence of many different elements but, for various reasons, the results are subject to question.

The diffusion of U from an U-impregnated graphite (0.25 gm U/cm^3) into an unimpregnated graphite (National Carbon grade AGOT) has been studied by Loftness (48). The diffusion coefficient was measured at three temperatures and the data represented by

$$D_{U(G)} = 1.28 \times 10^{-5} \exp - 53,000/RT$$

The data were inadequate because only 2 or 3 points were determined in each composition profile. Diffusion of U into graphite from a UC_2 deposit on the surface was examined by Loch et al. (49) who postulated two mechanisms for the process. His concentration profiles were divided into two regions: a low-concentration high-penetration tail, and a high-concentration low-penetration beginning. The large penetration portion was attributed to migration in the graphite pores and the steeper profile to volume diffusion. The volume diffusion portion was analyzed and the data represented by

$$D_{U(G)} = 7.6 \times 10^{-3} \exp - 87,000/RT$$

between 1800 and 2300°C . Above 2300°C , the apparent diffusivity was observed to increase sharply and no good explanation was given.

Kisiyi and Samsanov (50) measured the diffusion of B in synthetic graphite, using standard sectioning techniques combined with chemical analysis, and found the following relationship

$$D_{B(G)} = 3.02 \exp - 57,250/RT$$

to hold. They claimed extensive substitutional solubility (up to 26 wt %) of B in graphite based on a smooth increase in the (0006) x-ray diffraction peak of graphite with increasing B content. However, no other x-ray evidence was cited, and a shift in an (000l) line would more likely signify interlayer penetration. Aside from this, the diffusion data seem to be reasonable but very little information was given.

Truitt et al. (51) measured the diffusion of Th in synthetic and pyrolytic graphite. Specimens were coated with Th-232 by ionically bombarding them with singly charged ions, and following the diffusion anneals, the specimens were exposed to a thermal neutron flux to produce Th-233 which decayed rapidly to Pa-233. The specimens were then sectioned, and the residual Th content was taken to be proportional to the Pa-233 assay. The authors state that the data "suggest 60 and 70 kcal/mole, respectively, as the energy of activation for diffusion of Th in porous and pyrolytic graphite, c-direction." They further note the similarity of predicted diffusivities for U in graphite (48, 49) and carbon in graphite (35). The authors do not mention that the latter data for carbon in graphite were interpreted on the basis of grain boundary diffusion while their Th data were interpreted as volume diffusion. In a note

added in proof, the diffusion of Th perpendicular to the c-axis in PG was given as 2.5 orders of magnitude greater than that parallel to the c-axis.

E. Contributions of Wolfe, McKenzie, and Borg

Wolfe, McKenzie and Borg (WMB) (17) recently completed the first investigation of metal diffusion in graphites under carefully controlled conditions. They measured the diffusion coefficients of Ag, Ni, U, Th, and Ra in PG (perpendicular and parallel to the c-axis), National Carbon grade ZTA graphite (a high density synthetic graphite), and Speers grade S-700 (a porous, low density graphite). Diffusion specimens were prepared by evaporating an aqueous solution of a salt of the tracer, by flashing from a heated filament, and by vacuum evaporation. The technique of deposition by evaporation of an aqueous salt solution was not suitable for the more porous synthetic graphites due to capillary action but functioned quite well for the PG. The difficulty with the salt deposit is the lack of knowledge regarding the chemical state of the diffusing species. WMB did not find any anomalies caused by this deposition technique, which is to be expected when one considers the high temperature instability of many metal salts and the high affinity of most metals for carbon.

Diffusion anneals were made in vacuum and sectioning accomplished by attaching the sample to a piston-in-cylinder arrangement and abrading. The amount removed and penetration distance were determined by the loss of weight of the sample and piston. Penetration profiles were established by counting the activity remaining after each sectioning. In addition, autoradiographs were taken to demonstrate any non-uniform distribution of the diffusing atoms.

A summary of WMB's data is given in Table 3. Besides these summary data, WMB also noted that, in PG, there is a slight increase in the c-axis diffusion coefficient perpendicular to the deposition plane near the substrate surface (see Chapter III) as compared with that near the terminal deposition surface. In autoradiographs of Ag, Ni, and U in PG, WMB observed that, when diffusion occurred perpendicular to the deposition plane, the diffusing specie was concentrated at the cone boundaries (see Chapter III and IX); while parallel to the deposition plane, the diffusing atoms are uniformly distributed. In the synthetic graphites, the autoradiographs showed inhomogenieties on a very small scale ($\sim 1\text{mm}$) but this did not seem to affect the results. WMB also found that the diffusion coefficient of Ni in very well annealed PG (3000°C , 15 minutes) was about 3×10^{-4} times that of as-deposited PG.

Some general conclusions concerning the data of WMB are as follows:

- Lower melting metals (Ag, Ni) have lower activation energies (Q) and much higher diffusivities than do the higher melting metals at a given temperature.
- For Ni and U, $Q_a > Q_c$ but for Th, $Q_a < Q_c$.
- For Ni, U and Th, $D_{o-a} > D_{o-c}$, but by varying amounts.
- For diffusion perpendicular to the deposition plane, the diffusing species tends to concentrate at the cone boundaries of the PG but for diffusion parallel to the deposition plane, it seems to be uniformly distributed.

Table 3
SUMMARY OF THE DATA OF WOLFE, MCKENZIE AND BORG^(a)
 $D = D_0 e^{-Q/RT}$

Element	Graphite	Direction	Temp. Range (°C)	D_0 cm ² /sec	Q kcal/mole	Avg. Deviation From Predicted Diffusivity (%)
Ag-110	PG	<a>	600- 800	9.28×10^3	64.3 ± 2.6	6.4
Ni-63	PG	<a>	550-1000	1.02×10^2	47.2 ± 2.2	9.3
Ni-63	PG	<c>	750-1050	2.2	53.3 ± 4.8	14.8
U-232 ^(b)	PG	<a>	1400-2200	6.76×10^3	115.0 ± 2	6.0
U-232	PG	<c>	1800-2200	3.85×10^2	129.5 ± 5	25.0
Th-228	PG	<a>	1650-2150	1.33×10^5	145.4 ± 3	10.5
Th-228	PG	<c>	1800-2300	2.48	114.7 ± 3	5.1
Ra-224 ^(c)	PG	<a>	1650-2150	1.18×10^4	99.4 ± 3	5.2
U-232	ZTA	-	1600-2100	6.22×10^5	135.1 ± 3	7.9
U-232	S-700	-	1600-2100	9.29×10^5	136.6 ± 3	16.0
Th-228	ZTA	⊥ and to extru- sion direction	1889	$D_y/D_x = 2.68$		

(a) Ref. 17

(b) U-232 freshly prepared to avoid complications caused by daughter products

(c) Impurity present in Th-228 tracer

- The D_0 's for U in synthetic graphite are appreciably higher than either D_0 in PG but the activation energies in synthetic graphite are comparable to that parallel to the deposition plane in PG.
- Diffusion of Ni parallel to the deposition plane in very well annealed PG is considerably less than in as-deposited PG.

F. Contribution of Hennig

Hennig (18) has recently reported data on the diffusion of B in graphite single crystals. The measurements are based on the influence B has on the chemical activity of graphite and the technique is essentially one of etch pit decoration and quantitative electron-metallurgy. Several arguments were put forth that B enters the graphite lattice substitutionally. The diffusion coefficients of B in graphite were determined between 1760 and 2290°C as

$$D_{\parallel c} = 6320 \exp(-157,000/RT)$$

$$D_{\perp c} = 7.1 \exp(-153,000/RT)$$

The agreement with Kanter's carbon self-diffusion data (21, 22) ($Q = 163,000$ kcal/mole) was noted, but Hennig did not think that B diffuses by a vacancy mechanism. The question of mechanism was deferred until his work on lattice vacancy mobilities is complete.

G. Summary

Theoretical calculations for self-diffusion in graphite are far from complete and considerable differences exist between the various authors. Furthermore, even though graphite single crystals larger than a few millimeters are not available, there have been no theoretical treatments or even a listing of the many possible planar defect diffusion mechanisms such as along the layer edges, down the edges, across the surfaces of crystallites, and adjacent to the the crystallites but in the region where the bonding differs from that of nearly ideal hexagonal graphite. Some other mechanisms for diffusion within the crystallites which have not been examined are:

- Interstitial diffusion along the c-axis by going through the center of the benzene rings which compose the layers of graphite
- Vacancy-atom interchange between layers, especially at internal defects
- Atomic transfer from one layer to the next at the edges of internal defects consisting of many missing atoms arranged as "vacancy" benzene rings (52).

Table 4 lists the probable values of the activation energies of the processes which have been treated theoretically.

Tracer self-diffusion experiments have not been very successful. The only activation energy with any degree of reliability is that due to Kanter (21, 22) of 163 kcal/mole, which was subject to many assumptions. Hennig's activation energies for B in graphite of 155 kcal/mole lend considerable credence to

Table 4
**ESTIMATES OF ACTIVATION ENERGIES FOR
 VARIOUS DIFFUSION PROCESSES IN GRAPHITE**

<u>Process</u>	<u>Activation Energy (kcal/mole)</u>
Formation of layer vacancy	140 ± 60
Motion of layer vacancy	80 ± 20
Formation of divacancy	~ 150
Direct interchange within layer	~ 100
Formation of interlayer carbon atom	> 60
Formation of interlayer xenon atom (4.4 Å diameter)	~ 350
Motion of interlayer atom, carbon or xenon	~ 1

Kanter's data, but a careful tracer experiment with large single crystals, perhaps produced pyrolytically at very high temperature, is still needed.

The understanding of metal diffusion in graphites is even less than that for self-diffusion. The many studies of the migration of fission fragments have been hopelessly complicated by radiation damage, the complex nature of synthetic graphites, and the presence of many chemical species. With the exception of WMB's data, studies of metal diffusion in graphite are marked by an absence of careful characterization of the graphite, a lack of use of the full spectrum of analytical tools, such as autoradiography, and generally poor data. Even if attention had been given to these details, the complexity of synthetic graphite would have made fundamental interpretations difficult. Although WMB's investigation was generally of high quality, it did not delve deeply into the structural dependence of metal diffusion in graphites but did demonstrate that PG is the least complicated graphite available for study.

Chapter III

STRUCTURE OF PYROLYTIC GRAPHITE

A. Introduction

PG is one of many forms of pure carbon. Thus, the structural chemistry of carbon must be understood before examining PG whose structure is directly related to the manner in which it is made, and whose properties depend upon that structure. This structure can be characterized using metallographic and x-ray techniques, with additional information available through density and porosity measurements. Studies of the structure-sensitive properties of PG and their change with heat-treatment also provide information concerning the nature of the PG deposit.

In this chapter, the structural chemistry of carbon will be discussed, as will the techniques for manufacturing PG. Following this, the details of the structural characterizations of PG using metallography, x-ray diffraction, and other techniques will be outlined, and a short discussion of graphitization in PG will be given.

B. Structural Chemistry of Carbon

The element carbon is capable of participating in a wide variety of structures. In inorganic compounds, carbon reacts with metals and semi-metals to form solid solutions and simple compounds (53, 54, 55). Carbon also provides

Chapter III

STRUCTURE OF PYROLYTIC GRAPHITE

A. Introduction

PG is one of many forms of pure carbon. Thus, the structural chemistry of carbon must be understood before examining PG whose structure is directly related to the manner in which it is made, and whose properties depend upon that structure. This structure can be characterized using metallographic and x-ray techniques, with additional information available through density and porosity measurements. Studies of the structure-sensitive properties of PG and their change with heat-treatment also provide information concerning the nature of the PG deposit.

In this chapter, the structural chemistry of carbon will be discussed, as will the techniques for manufacturing PG. Following this, the details of the structural characterizations of PG using metallography, x-ray diffraction, and other techniques will be outlined, and a short discussion of graphitization in PG will be given.

B. Structural Chemistry of Carbon

The element carbon is capable of participating in a wide variety of structures. In inorganic compounds, carbon reacts with metals and semi-metals to form solid solutions and simple compounds (53, 54, 55). Carbon also provides

the foundation for organic chemistry by reacting with itself, hydrogen, and to a lesser extent, with other elements to produce a wealth of organic compounds. These compounds are divided into four general types: aliphatic, aromatic, alicyclic, and hetero-cyclic (56), each of which contains many different structures. The aliphatic compounds are based upon carbon-bonded chains and the aromatics are based upon six-membered benzene rings. Alicyclic compounds are composed of different-sized carbon-bonded ring structures with alicyclic properties; hetero-cyclic compounds are ring compounds which incorporate other atoms — usually nitrogen, oxygen, and sulfur — into the rings and behave generally as either aromatic or alicyclic compounds. Carbon can further combine with itself to produce macro-molecules or networks of carbon atoms which are the structural units of the solid carbons. Solid carbon products are divided into two general categories (57); graphitic carbons and non-graphitic or "amorphous" carbons. The graphitic carbons consist of approximately planar nets of carbon hexagon rings which have a tendency, upon heating, to produce the ideal hexagonal graphite lattice. Non-graphitic or "amorphous" carbons result when these macro-molecules include many different kinds of carbon bonds. They are termed amorphous because, although there is some tendency for the macro-molecules to lie parallel to each other, there is a very high degree of disorder which produces a very broad, diffuse x-ray diffraction pattern.

The ideal, hexagonal graphite structure, first proposed by Bernal (58) and shown in Fig. 1, consists of parallel sheets of carbon hexagons arranged in

a = 2.4612 Å
c = 6.7076 Å
c/2 = 3.3538 Å
carbon-carbon separation = 1.415 Å
4 atoms per unit cell
X-ray density = 2.267 gm/cm³

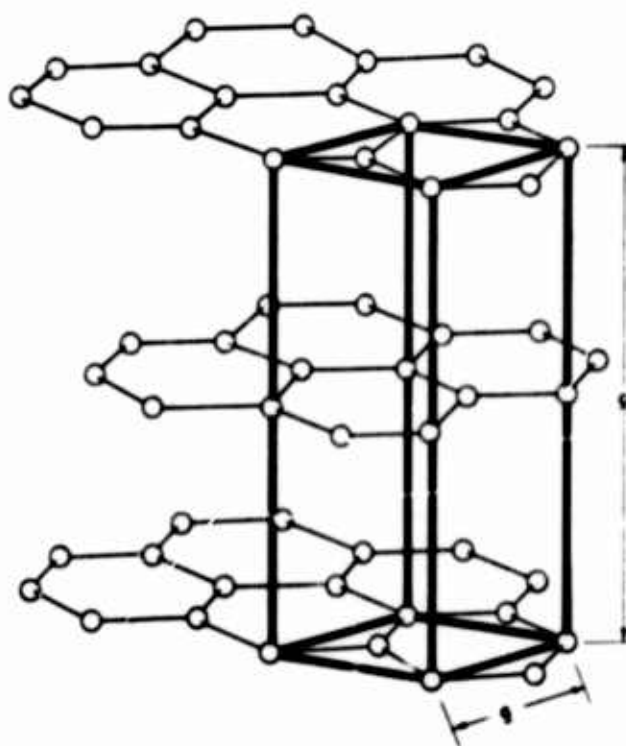


Fig. 1 Crystal Structure of Ideal Hexagonal Graphite

an abab... stacking sequence. In this structure, the interlayer separation is 3.3538 Å, and the carbon-carbon distance within each layer is 1.415 Å (9, 59). The carbon-carbon distance within the sheet is virtually independent of interactions with other layers (60) because of the bond structure. Carbon has four valence electrons per atom; three of which are used to form regular covalent bonds with each of the three nearest neighbors in the hexagonal network, while the fourth electron (called the π electron) is free to form resonance bonds over the entire layer (32, 59). These π electrons are responsible for the electrical, thermal, and magnetic properties of graphite and for the interlayer bonding which permits the graphite structure to exist (9).

A slightly less stable form is rhombohedral graphite which has an abcabc... stacking sequence. The heat of transformation of rhombohedral to hexagonal graphite has been estimated to be -144 ± 41 cal/mole (61). The hexagonal form is, by far, the most prevalent; however, hexagonal graphite can be partially converted into rhombohedral graphite by grinding (62). The macro-molecular layers are considered to be held together by van der Waal's forces; however, interlayer charge transfer bonds have also been postulated (9). The interlayer bond energy for either structure is estimated to be between 8 and 20 kcal/mole depending upon the method used to compute it (9). The small difference in energies for the two stacking sequences, the large interlayer separation, and the rather low interlayer bonding energy combine to permit the partial or complete lack of a layer stacking sequence. This lack of order is known as

"turbostratic" disorder (63). Its principal effect, to be discussed later, is to increase the interlayer spacing. When the spacing is greater than the ideal 3.3538 Å, the structure is referred to as nearly ideal hexagonal graphite (9).

Carbon can exist in still another form, the diamond structure, in which the atoms are situated symmetrically with four equal tetrahedral bonds to nearest neighbors. The diamond structure is unstable relative to the hexagonal graphite structure, with the heat of transformation at 298 K estimated to be 453 ± 20 cal/mole (9).

Graphite products are available in many forms. Their differences result from the relative proportions of "amorphous" carbon and nearly ideal hexagonal graphite. Natural graphite consists principally of large crystallites with perfectly stacked layers, while carbon blacks, soots, and hard-baked carbons consist of randomly bonded carbon macro-molecules, with some regions of small stacks of nearly parallel hexagon sheets. For reviews and listings of some of the many different forms of carbon see references 27, 59, 64, 65, 66.

Synthetic graphites of widely variable properties are produced by heating organic cokes with suitable binders to high temperature in the absence of air to drive off the non-carbon atoms and produce the various macro-molecules of carbon described above. The resulting body contains crystallites of approximately ideal graphite surrounded by somewhat less organized carbon. This material is relatively porous and soft, rubbing off onto other objects easily (the reason why graphite-clay mixtures are used in pencils). The less

graphitized carbon products do not mark other objects as readily, because they contain smaller volume fractions of the soft, nearly ideal, graphite particles.

Synthetic carbon products can also be produced by the pyrolytic decomposition of simple organic compounds like methane under controlled pressure and temperature conditions (1, 67, 68, 69). The resulting bodies differ from the other graphites in that there is very little truly disorganized carbon and the crystallites tend to lie parallel to the deposition substrate, producing a high degree of anisotropy in many properties. The density of pyrolytic graphite is a function of the deposition temperature, being higher the higher the temperature. Deposits made above about 2100°C (1, 67) approach the theoretical x-ray density.

All the as-deposited PG's have a high degree of turbostratic disorder, leading some authors to term this material pyrolytic carbon (PC). There is no definite distinction between PG and PC, but the less ordered material with very small crystallite size produced by deposition below about 1900°C should be called PC and the material with the larger crystallite size and nearly theoretical density deposited above 1900°C should be termed PG.

In contrast with the other forms of synthetic graphite, PG is hard and dense, and pieces of PG a few inches square produce a "metallic ring" when dropped on a hard surface.

C. Manufacture of PG

Methods of making PG were described as early as 1880 by Sawyer (70) and 1883 by Edison (12). The technique involves thermally decomposing a carbon-bearing gas at or near a substrate, causing carbon to be deposited on the substrate. Until the mid-1950's the size of deposits was limited, and the only use for carbon made by this process was the carbon electrical resistor (71). In 1958, Brown and Watt (1) gave the first report on the production of massive PG. Their work was followed closely by Diefendorf (67, 68, 69) of General Electric, and Pappis and Blum (3) of Raytheon Company. PG technology advanced very rapidly, and by 1963 at least four companies were manufacturing many different forms (66).

PG is deposited at low gas pressure with substrate temperatures between 800 and 2800°C (12, 67, 68, 69). For structural use, it is generally deposited above 2100°C to provide high density and good mechanical properties. Two methods of heating the substrate are used: self-resistance heating and induction heating (67, 72). Two other variations in furnace design are the use of cold wall and hot wall furnaces (67). The cold wall furnace generally produces non-homogeneous material because of large temperature gradients through the thickness of the PG and large gradients in composition and temperature in the gas (67). As a result, most commercial facilities use hot wall furnaces.

The important parameters controlling the structure of the deposit are the deposition temperature and gas pressure. Both of these control the rates at which nucleation and growth occur at the deposition surface, and these rates

control the degree of crystalline perfection (72), the degree of preferred orientation (73), the crystallite size (73), and many other structural parameters (67).

D. Metallographic Structure of PG

In physical appearance, PG is dark gray and can be polished to a dark metallic luster. The surface away from the substrate, the terminal deposition surface, is covered with slightly rounded nodules of a size characteristic of the deposition process. The substrate surface (the surface at which nucleation first started) is covered with much smaller circular dimples which reveal, approximately, the original nucleation sites. The structure of PG is formed by the competitive nucleation and growth of cones or paraboloids with their major axes perpendicular to the deposition surface. Two major types of cone growth are recognized (12), substrate nucleated and regeneratively nucleated. Substrate nucleated PG consists principally of cones that were nucleated at the substrate and continued to grow throughout the thickness of the deposit, while regeneratively nucleated PG is characterized by a recurring nucleation of cones through the deposit. Material representative of both structures was used in this study, and photomicrographs of the different PG's are shown and discussed in Chapter VII. In the substrate nucleated material, other cones or paraboloids will occasionally nucleate in the middle of the deposit and grow in a fashion similar to the substrate nucleated cones. The presence of soot or other foreign matter on the advancing deposition surfaces causes this nucleation (67) which results in the extra cones and in the regeneratively nucleated structure.

Actually, the structure of PG deposits ranges from that in which the substrate nucleated cones are dominant to that dominated by the regeneratively nucleated cones.

PG microstructure is further complicated by the presence of a fine, secondary substructure that is presumably associated with many inefficient nucleation sites on the advancing deposition surface. Pappis (74) has characterized the PG microstructure according to the following scheme:

Primary Structure Dominant (substrate nucleated)

- (A) Straight sided cones - A1, A2, A3*
- (B) Curved sided cones - B1, B2, B3

Secondary Structure Dominant (combination substrate and regenerative nucleated)

- (C) Straight sided cones - C2, C3 (no C1 observed)
- (D) Curved sided cones - D1, D2, D3

Intra-layer Structure (regeneratively nucleated)

- (E) Straight sided cones - E1, E2, E3
- (F) Curved sided cones - F1, F2, F3

and this scheme was employed to characterize the material used in this investigation. The anisotropy of PG is reflected in its optical behavior under crossed polarized light; photomicrographs are generally taken at 15 degrees from

*1, 2, 3 correspond to coarse, medium, and fine cone sizes, respectively.

extinction to provide maximum resolution of the structure. The fact that the cone structure is clearly observed under polarized light is proof that the boundaries seen in the microscope represent the boundaries between groups of crystallites having different orientations; however, within the major cones and within the secondary cones, there is a uniform variation in the optical activity with sample rotation, demonstrating that the crystallographic orientation within even the minor cones varies from one side of the cone to the other.

High magnification transmission electron microscopy studies (75, 76, 77) have shown that PG consists of stacks of overlapping wrinkled sheets a few hundred Å thick, with facets on the wrinkled sheets about 200 Å wide. Dislocation structures such as the networks observed in graphite single crystals (78) and synthetic graphite (79) have not been observed in PG. As will be discussed in the next section, the crystallite diameter of PG is about 200 Å while that of other graphites is about 3000 Å. Because it is difficult to resolve structural details within a 200 Å diameter region, no dislocation structure has been observed in PG.

E. X-ray Structure of PG

In this section, the structure of PG, as determined by x-ray diffraction, will be discussed, using the interpretations of diffraction patterns developed for carbon blacks and graphitic carbons. First, the layer structure and layer stacking will be discussed, followed by discussions of crystallite size and preferred orientation. Next, the variation of structure with orientation will be noted and a discussion of small angle scattering in PG will be given.

Brown and Watt (1) first demonstrated that PG has an x-ray structure similar to that of graphitic carbon so the detailed theories developed for these carbon materials can be applied to PG. For instance, Warren (80) showed that graphitic carbons are made up of small regions of approximately parallel layer planes which, in turn, are composed of hexagonal benzene rings, just like the graphite structure. Warren (81) further demonstrated that such carbons show only two kinds of diffraction peaks: $000l$ reflections from the parallel layer planes, and two-dimensional hk bands which are the result of a relaxation of the crystalline order in the c -direction. This concept was further developed by Biscoe and Warren (63) to prove that carbon blacks consist of graphite-like layers stacked in parallel groups but otherwise without mutual orientation. The concept of a stacking order in carbon black has no meaning because the layers are randomly rotated about their mutual layer plane normal. As a result of this structure, the $000l$ diffraction peaks are symmetric, while the hk bands are asymmetric with the intensity falling off very steeply on the low 2θ side and decreasing very gradually on the high 2θ side.

The concept of a crystallite size in carbon blacks is still valid, being a measure of the range over which the layer planes are parallel (L_c) and the average diameter of the layers in the stack (L_a). This will be discussed in more detail shortly.

Carbon blacks are grouped in two general classes (57, 82), those which approach the graphite layer stacking order upon heat treatment and those that

do not. Carbons in the first class are called graphitizing and those in the second, non-graphitizing. When graphitizing carbons have become partially graphitized, the hk bands show modulations which indicate the beginning of diffuse hkl reflections. At the same time, the interlayer spacing computed from the 000ℓ diffraction lines is found to decrease, following the decrease in the degree of disorder in the blacks. This observation has been treated by Franklin (82), Bacon (83), Bacon and Franklin (84) and Bacon alone (60) in some detail with the conclusion that four different interlayer spacings exist in a stack of graphitic layers. A description of these layers and their spacings is given below:

1. Between two oriented layers; e.g., with the corners of the hexagons in one layer directly above the centers of the hexagons of the other (d = 3.354 Å)
2. Between two disoriented layers, each of which is disoriented with respect to its neighbor (d = 3.440 Å)
3. Between two disoriented layers, one of which is oriented with respect to its neighbor (d = 3.408 Å)
4. Between two disoriented layers, both of which are oriented with respect to their neighbors (d = 3.376 Å)

Franklin (82) and Bacon (60) were able to show that the probability of a stacking error, p , as determined from analyses of the diffraction breadths and shapes of hkl diffraction peaks, could be related to the observed interlayer spacing.

d_{0002} . This relationship is shown in Fig. 2. Various theoretical expressions were derived to fit the observed curve (60) and they agree fairly well over certain ranges of p . Although a direct comparison of p versus d_{002} in PG has not been made, it is reasonable to assume that the same relations hold, provided accurate determinations of d_{0002} are made.

The a parameter of PG can be obtained from the 10 and 11 bands, using the hexagonal d-spacing relationship

$$1/d^2 = 4/3a^2 (h^2 + k^2 + hk) + l^2/c^2$$

Warren (81) has derived a correction factor for the peak shift of an hk band from the theoretical position of the corresponding hko peak. The shift is to higher angles and of magnitude

$$\Delta \sin \theta = 0.16 \lambda/L_a$$

For PG, L_a is typically greater than 100 Å, making this shift negligibly small. A precision extrapolation is possible if several hk bands are observed but the data invariably yield 2.46 Å, regardless of the condition of the PG, indicating the relative stability of the intra-planar bonds over the inter-planar bonds.

Estimates of the crystallite sizes, L_a and L_c , of graphitic carbons using the Scherrer equation, with appropriate modification (60, 85, 86) or using a Fourier analysis of the diffraction peaks (72, 86, 87, 88) have been made. The

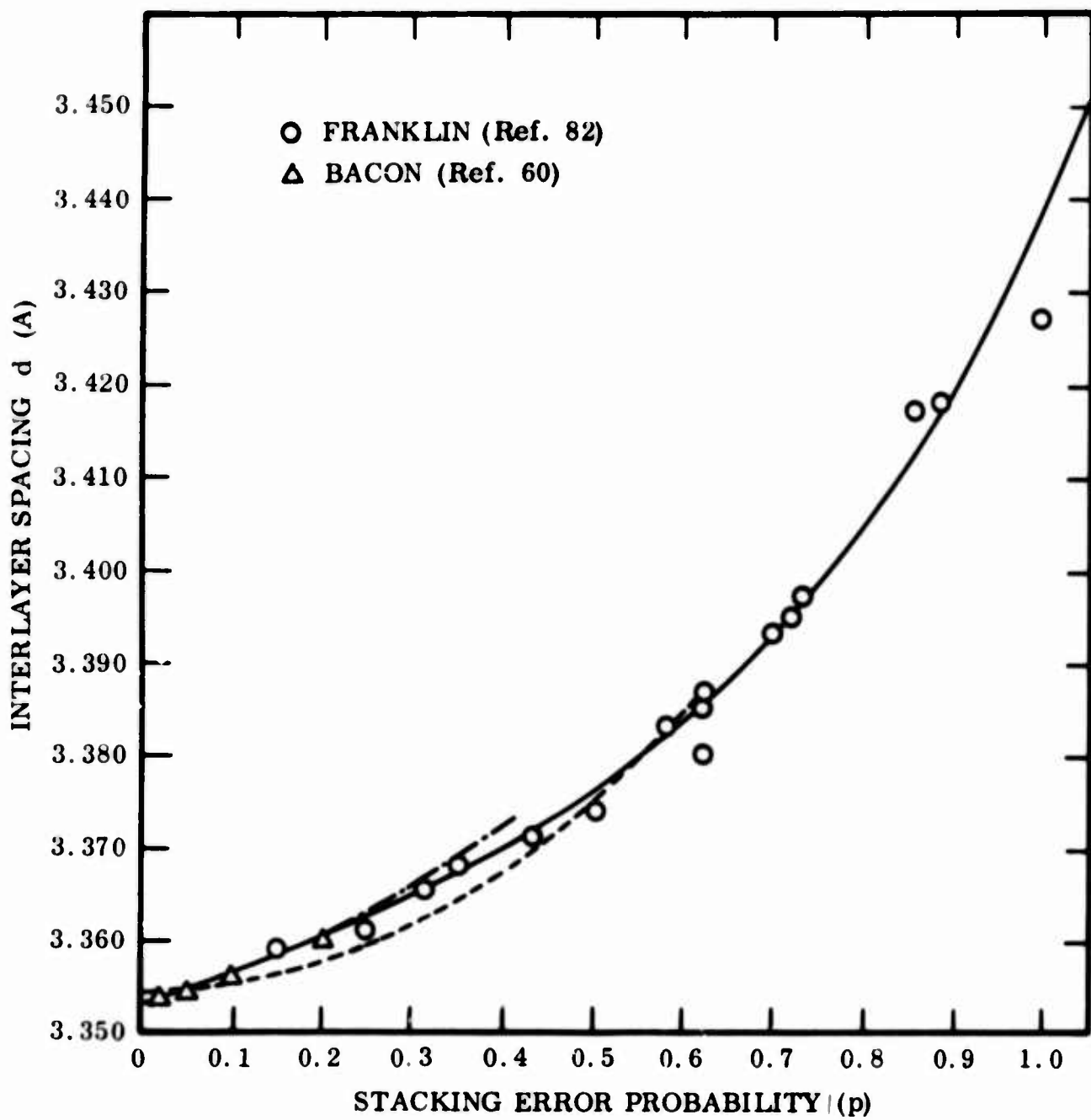


Fig. 2 Interlayer Spacing vs. Stacking Error Probability for Graphitic Carbons

difficulty of estimating crystallite thickness lies in establishing the definition of a crystallite in graphitic carbon and interpreting the effect of the four interplanar spacings postulated by Bacon and Franklin on the line breadth and shape. Houska and Warren (88) have attempted to account for the effect of two layer spacings in carbon black and Guentert and Cvikovich (72, 86) have applied the rigorous Warren-Averbach method (89) to PG. Guentert and Cvikovich (GC) (86) reported their data with sufficient detail to make possible a comparison of their Fourier results with those from the more convenient Scherrer equation. Table 5 shows the results of this comparison. For crystallite thicknesses below about 700 Å, the 0002 line breadths with the Warren correction (90)

Table 5
COMPARISON OF METHODS OF COMPUTING
CRYSTALLITE THICKNESS IN PG

Specimen Number	Crystallite Thickness - L_c (b) (Fourier Analysis)	Crystallite Thickness - L_c (Warren Correction) (b)		
		0002 (c)	0004 (c)	0006 (c)
AD	200 Å	190 Å	100 Å	70 Å
25	310	310	180	120
27	380	380	230	170
28	700	600	350	300
30	850	1120	680	630

-
- (a) Specimen designation and Fourier analysis by
Guentert and Cvikovich (Ref. 86)
(b) $\beta^2 = B^2 - b^2$, $L_c = \lambda/\beta \cos \theta$
(c) Different orders from (000l) planes

give fairly good agreement with the more rigorous Fourier treatment. GC (86) further showed that the line broadening of the hk bands in PG is due only to particle size so the Warren modification (81) of the Scherrer equation

$$L_a = \frac{1.84\lambda}{\beta \cos \theta}$$

is directly applicable; however, the peak should be corrected (86), for instrumental broadening (90), $\alpha_1\alpha_2$ doublet broadening (91), preferred orientation effects (86, 92), and absorption broadening (93). Although a correction factor for the hk bands for preferred orientation effects has been derived by GC (86, 92), they did not apply it to their earlier (86) data because they estimated the effect to be less than 20%. The effect of the preferred orientation correction is to increase the line width while the absorption correction tends to decrease it; thus, if the corrections are ignored, their effects tend to be cancelled. Partial ordering leads to modulations in the hk bands of PG and carbons (72, 86, 87), and line broadening theories for this condition have not been fully developed (86).

The layer structure of graphite causes it to exhibit a high degree of preferred orientation when pyrolytically deposited (67). The preferred orientation in PG has been studied by GC (72, 86, 87), Bragg with Hammond and co-workers (5, 94), and Noda, et al. (73). Because they find it convenient to use in their calculations, Noda and Guentert represent the preferred orientation with a $\cos^m\alpha$ function, where α is the inclination angle of the crystallite

layer planes relative to the deposition surface. On the other hand, Bragg and Packer (94) found that the preferred orientation had a Gaussian distribution over two orders of magnitude in pole density, and they represent their data as an exponential function of α^2 . Both functions are approximations, with the $\cos^m \alpha$ function showing deviations at a layer plane pole density of about 10% (86, 92) while the Gaussian function behaves well out to 1% pole density in as-deposited material (94) and out to about 5% in heat treated material (5). The effects of heat treatment will be discussed in more detail later.

Bragg and Packer (94) also demonstrated that the structure of PG is orientation dependent, with the degree of perfection generally decreasing with increasing inclination to the deposition surface and with the disparity in perfection increasing markedly with heat treatment. This change in degree of perfection requires the use of integrated intensities for all preferred orientation studies in PG.

Small angle scattering by PG has been studied by Bragg, with Hammond and others (95). They showed that PG contains disk-like voids, 22 Å thick and 44 Å in diameter, that lie in the deposition plane and have a spacing comparable to that of the crystallites. Such voids in PG could very easily be associated with the wrinkled sheets found in Stover's electron microscopy studies (75).

F. Other Structural Parameters

In addition to the parameters discussed above, the PG structure can be further characterized by density and pore spectrum determinations. It has been noted that PG is impermeable to inert gases (67) and liquids (96), in

agreement with the lack of visible porosity in the microstructure. This means that the pore spectrum cannot be determined by gas or liquid porosimetry, as is done with other synthetic graphites (27), but must be measured using small angle scattering of x-rays. The displaced-volume density is slightly less than that computed from the x-ray layer spacing, indicating a small sub-microscopic porosity. The x-ray density of PG is a function of the unit cell dimensions and, since the a parameter is essentially constant regardless of the condition of the graphite, the change in x-ray density is related only to the changes in the layer spacing. With an a parameter of 2.461 Å, the x-ray density of nearly ideal hexagonal graphite can be expressed as

$$\rho_x = \frac{15.207}{c} = \frac{7.603}{d_{0002}}$$

where ρ_x is the density in gm/cm³, c the unit cell height in Å, and d_{0002} the average layer spacing in Å. Table 6 lists the graphite x-ray densities for various values of d_{0002} and gives some experimental values of d_{0002} and ρ_x for comparison. The measured density is about 0.02 gm/cm³ or 1% below the theoretical value and this difference must be associated with the porosity indicated by the small angle scattering.

Information regarding the structure of PG can also be obtained by measuring structure-sensitive properties, such as transport and mechanical properties. The thermal (97) and electrical (6, 98) conduction properties have been used to

Table 6
**X-RAY DENSITY AS A FUNCTION OF INTERLAYER SPACING
 AND COMPARISON WITH EXPERIMENT**

Computed		Observed ^(a)	
d_{0002}	ρ_x gm/cm ³	d_{0002}	ρ_x gm/cm ³
3.440 Å	2.210		
3.420	2.223	3.420	2.200
3.400	2.236		
3.380	2.249		
3.370	2.256	3.372	2.225
3.360	2.263	3.366	2.238
3.354	2.267	3.360	2.254

^(a) Observed data from Pappis (Ref. 74.)

demonstrate the anisotropy and preferred orientation of PG and to gain an understanding of its band structure. In addition, mechanical property measurements at high temperature (5, 77) have been used to determine the nature of the bonding between the crystallites in PG. One of the purposes of this investigation is to employ the mass transport properties of PG to increase our understanding of PG structure.

G. Graphitization in PG

Graphitization is the general process by which, on heat-treatment, carbon products approach the ideal graphite structure. The intermediate stages of this process, in the case of PG, are indicated by the following changes (74, 86, 99):

- An elimination of the secondary microstructure

- A decrease in the interlayer spacing
- A sharpened layer plane texture
- An increase in crystallite size
- A shrinkage perpendicular to the deposition plane
- A slight elongation parallel to the deposition plane
- An increase in density

For a given thermal treatment, those crystallites oriented nearly parallel to the deposition surface graphitize more fully than those inclined to the surface (5, 94). Furthermore, the anisotropy ratios of transport properties, i.e., the electrical and thermal properties, are increased by graphitization (74). The terminal stages of the process are noted by a nearly complete elimination of the microstructural detail and a closer approach to the theoretical values of the various x-ray parameters. Perfect single crystals have not been produced by graphitization, but material approaching a mosaic single crystal, as determined by the interlayer spacing, crystallite size, and texture, have been produced (86). One problem with such material is the presence of delaminations parallel to the deposition surface which are introduced when the texture is sharpened.

The rate of graphitization in PG becomes appreciable around 2500°C (5) and reaches terminal stages in reasonable times somewhat above 3000°C (99). Concurrent stress, either in tension parallel to the deposition plane (5, 77) or in compression (100) perpendicular to it, considerably enhances the graphitization process, lowering the graphitization temperature 50 to 100°C and greatly

altering the terminal values of the various structural parameters toward greater perfection.

Kinetics of the above changes have not been studied in detail; instead, the subject has been treated much as the early studies of recrystallization in metals. In these studies, changes in various properties were observed following fixed-time anneals at different temperatures. From a plot of property versus temperature of anneal, a recrystallization or graphitization temperature can be defined as the temperature at which a large change in property occurs. One study of the kinetics of graphitization has been made by Fischbach (101) who used magnetic susceptibility and d_{0004} measurements to characterize the PG structure. The rates of change of these properties with time at temperature were analyzed using sequential first order reaction rate theory, but no justification of this procedure was given. It is by no means clear that these properties bear a homogeneous relationship to the amount of transformation as is required to apply reaction rate theories based on the Law of Mass Action (102).

H. Summary

Studying the effects of PG structure on a property requires a complete characterization of the structure. This characterization involves the simultaneous application of several techniques of metallography and x-ray diffraction, together with accurate density measurements. These techniques have

been applied to the structural aspects of mechanical and electrical properties and will be required to examine the role of structure on metal diffusion in PG. Some details of these techniques and their general results have been given in the discussion above.

Chapter IV

EXPERIMENTAL APPROACH

A. Statement of Problem

It is evident from the discussion in Chapters I and II that a study of the role of structure in metal diffusion in graphites would be both timely and useful. PG is the least complex massive graphite available, and techniques for characterizing its structure have been developed to the point where comparisons of structure and property are possible. A study of diffusion in PG requires developing the necessary experimental techniques and analytical methods to treat the problem and relating the results of the diffusion studies to the structure of the material being examined.

The purposes of this investigation are to determine the fundamental mechanisms of metal diffusion in PG, to increase the understanding of the structure of PG through these studies, and to investigate the possibility of diffusion-alloying PG.

B. Program Summary

Because of the expected low solubility of metals in graphite, high sensitivity radioactive tracer methods are ideally suited for studying metal diffusion in PG. Precision lapping techniques are also well suited to this study because they are sensitive and readily adapted to radioactive tracer methods.

To accomplish the objectives mentioned above, three different types of PG were chosen and specimens from each were given a single heat-treatment so that both the as-deposited and partially graphitized states could be studied. Radioisotopes of Re and Nb were selected as the diffusing species, with the emphasis placed on the Nb. Diffusion reactions of Re with PG were examined, and, with a precision lapping device, the diffusion of Nb in all three types of PG was studied. The diffusion coefficients of Nb in PG were determined for two conditions of each PG (as-deposited and heat-treated) and for the different "crystallographic" directions in PG (parallel and perpendicular to the deposition surface). Autoradiography was employed to observe any non-homogenous distribution of the diffusing atoms. The temperature range from 1400 to 1950°C was covered, corresponding to a range of three decades in diffusivity for each direction. The structure of each PG was characterized by the following:

- Metallographic structure at high and low magnification
- Transmission electron microscopy
- Stacking error probability, p , or degree of graphitization
- Crystallite size, L_a and L_c
- Degree of preferred orientation, as measured by the mean tilt angle
- Orientation dependence of the structural parameters p and L_c
- Submicroscopic void size and distribution, determined from small angle scattering
- High pressure Hg porosimetry
- Density, as determined by hydrostatic weighing

A mathematical analysis of diffusion in layered structures was made, and correlations between the diffusion and structural parameters were noted.

C. Choice of PG

Three different types of PG were chosen to be representative of the various types of PG available. The three types were all produced by Raytheon Company during their development work on PG and may be described in the Pappis notation listed in Chapter II (74) as follows:

R277: A2 structure, singularly nucleated, medium cone size

R165: C3 structure, combination singularly nucleated and regeneratively nucleated, fine cone size

R1: F1 structure, heavily regeneratively nucleated, medium cone size

Most of the work was concentrated on the R165 material because it had the fewest delaminations and most uniform structure. The R277 and R1 materials were marked by a variation in structure from one place in the deposit to another and a tendency toward delamination.

Since this investigation began, there have been many improvements in the production of the PG leading to thicker and more homogeneous deposits with less tendency toward delamination. However, the conclusions reached by this investigation will also apply to the new material and this will be discussed in Chapter IX.

D. Choice of Metal

Initially, it was thought that diffusion of metals in PG would occur with appreciable rate only at very high temperatures due to the high sublimation temperature of graphite. Because of this, metals with low vapor pressure at high temperature were sought so that the boundary conditions associated with the diffusion system would not be complicated by vapor transport. Because the vapor pressure of a metal is generally lower the higher its melting temperature, only high melting point metals were considered for these studies.

A second criterion for choosing metals for the diffusion studies in PG was whether a carbide forms. The description of a diffusion system that includes the formation and growth of compounds is not as simple as the description of a system without compound formation. Because of this, carbide formers should be used with caution in studies of diffusion in graphites.

The final criterion for choosing metals was the availability of a convenient radioisotope because radioactive tracer methods were to be used to determine compositions.

With above considerations in mind, the higher melting metals were divided into three groups:

- (1) Mono-carbide formers; Ti, Zr, Hf
- (2) Multiple-carbide formers; V, Nb, Ta, Cr, Mo, W, Mn, Fe, Co, Th, U
- (3) Non-carbide formers; Re, Ru, Os, Rh, Ir, Pd, Pt

Those with melting temperatures in excess of 2500°C are underlined.

Re was first selected based on a lack of reported carbides (103), a low vapor pressure (54), and a readily available radioisotope (104). Re-186 has a half-life of 3.87 days, decays principally by β^- emission, and is available as HReO₄ in HNO₃ from the Oak Ridge Isotope Development Center (104) with a relative specific activity of about 1%. As discussed in the next chapter, Re-186 was not satisfactory for these diffusion studies, and another metal with a very high specific activity had to be selected.

Nb-95 and Co-58 were the only readily available radioisotopes with carrier-free specific activity. Nb was selected over Co because Nb has a lower vapor pressure at high temperature and is a by-product of some nuclear reactors. The desirability of having a non-carbide former was considered to be secondary in this case because the carrier-free specific activity would permit the use of a very small quantity of metal in the diffusion couples.

Nb-95 has two isomeric states. The upper isomer decays by internal conversion with a 0.23 Mev electron and a 90 hour half-life. The lower isomer, on which these experiments were based, decays to Mo-95 by emitting a 0.16 Mev β^- and a 0.75 Mev γ -ray. The half-life of this isomer is 35 days (104).

E. Summary

Re-186 and Nb-95 were selected to study the diffusion of metals in PG. Because of difficulties related to specific activity, Nb-95 was the only metal for which diffusion coefficients were determined. The diffusion coefficients of Nb-95 were measured as a function of temperature and "crystallographic" direction in

three different kinds of PG in two different conditions. The structure of each PG was characterized using x-ray and metallographic techniques, and correlations between structure and diffusion data were sought to determine the fundamental mechanisms of metal diffusion in PG.

Chapter V

EXPERIMENTS WITH RHENIUM AND PYROLYTIC GRAPHITE

A. Introduction

Initial experiments were concerned with high temperature phase relations in the Re-PG system, using massive Re-PG diffusion couples. Following this work, studies of the diffusion of radioactive Re in PG were started, but these studies had to be abandoned because of difficulties related to the specific activity of the Re isotope. A description of the observed phase reactions is given below as is a summary of the diffusion studies.

B. Phase Reactions of Re with PG

Diffusion couples consisting of 1/8-in. diameter rods of Re and PG or other carbon product were clamped in a graphite fixture and annealed in argon for the various times and temperatures given in Table 7. Following the diffusion anneals, the specimens were mounted parallel to the axis of the rods and polished for examination.

Three different structures resulted from these couples: no adherence, adherence with no evidence of reaction, and adherence with strong evidence of reaction and the formation of an unexpected phase. The couples numbered 3, 4, and 5 did not adhere or react, a failure attributed to insufficient pressure applied by the clamp during the anneal.

Table 7
**LIST OF DIFFUSION COUPLES OF Re VERSUS PG
 AND OTHER GRAPHITES**

<u>Couple Number</u>	<u>Couple Composition</u>	<u>Temp. (°C)</u>	<u>Time (hr)</u>
1	Re vs. PG< a >	1800	3.0
2	Re vs. PG< a >	2100	2.5
3	Re vs. PG< a >	1960	2.0
4	Re vs. PG< a >	2070	3.0
5	Re vs. PG< a >	2150	3.0
6	Re vs. PG< a >	2100	3.0
7	Re vs. PG< a >	2180	3.0
8	PG< a > vs. Re vs. PG< a >	2200	4.0
9	Re vs. ZTA Graphite	2200	4.0
10	PG< c > vs. Re vs. Carbon (non-graphitic) vs. Re vs. PG< a >	2300	6.0

In couples 1 and 2, the Re adhered to the PG, but in couple 1 no evidence of reaction was resolved at 1500X. In couple 2, several regions near the interface exhibited a melted two-phase structure with graphite flakes also present. This structure is shown in Fig. 3 where the black phases are PG and graphite flake, the white phase Re, and the gray, an unexpected new phase. Because this gray phase was formed in the presence of carbon and was attacked by chromic acid, it was thought to be a carbide (105). The line of small, white particles across the bottom of the photographs probably denotes the original interface since the carbon inside this line does not have the original optical anisotropy of PG. This microstructure will be discussed in more detail in subsequent paragraphs.



**Fig. 3a Melted Structure in Rhenium-PG Diffusion Couple.
Polarized Light. 1000X**



**Fig. 3b Reaction Zone in Rhenium-PG Diffusion Couple.
Bright Field. 500X**

Couples 6 and 7 adhered but both couples separated at the interface during handling, leaving some reaction product on the Re. Couple 7 was mounted and polished for microscopic examination. This examination of 7 showed the same kind of structure as in couple 2. The reaction product from 6 was scraped off, and a Debye-Scherrer x-ray diffraction pattern was made from the powder. The powder pattern, obtained with Ni-filtered Cu radiation in a 57.3 mm camera, contained continuous lines of graphite and Re and an additional set of spotty or discontinuous lines. These additional lines indicated the presence of a small number of grains of a different phase. Table 8 includes an indexed list of lines observed in this diffraction pattern together with all the other lines of this phase observed in other diffusion couples.

Couples 8, 9, and 10 also adhered and showed strong evidence of reaction, thus demonstrating that Re will react with other forms of carbon below 2300°C. Debye-Scherrer patterns of scrapings from couples 8 and 9 were weak and inconclusive, but the pattern from 10 was fairly strong, and gave all the lines listed in Table 8.

To improve the diffraction patterns, several attempts were made to produce larger quantities of the new phase by heating pressed pellets of Re and C powder of different compositions. In all of the attempts, no lines or only the first two or three lines of the new phase were observed. Although there were good indications that the new phase was a carbide, the phase may possibly have formed from impurities in the argon. To be certain that the new phase was not an oxide

Table 8
**COMPILED OF DISCONTINUOUS DEBYE-SCHERRER
 LINES OBTAINED FROM MATERIAL TAKEN FROM
 Re-PG DIFFUSION COUPLES**

<i>d</i>	<i>I</i>	$(h^2 + k^2 + l^2)$	$\frac{a}{\lambda}$
2.8	S ^(a)	1	2.80
1.98	S	2	2.80
1.63	S	3	2.83
1.40	M ^(b)	4	2.80
1.26	M	5	2.82
1.15	M	6	2.82
Missing		7	
0.995	VW ^(c)	8	2.82
0.935	VW	9	2.81
0.886	VW	10	2.78
0.852	VW	11	2.82
0.814	VW	12	2.82
0.800	VW	13	2.89
0.780	VW	14	2.92

- (a) Strong
- (b) Medium
- (c) Very weak

or nitride, Re powder was heated in air at several temperatures up to 900°C at which all the Re powder volatilized by oxidation. X-ray diffraction and chemical etching techniques produced no correlations between these reaction products and the phase produced in the Re-PG diffusion couples.

Fourteen lines on the Debye-Scherrer pattern of the new phase were observed, the analysis of which indicated that the new phase has a simple cubic lattice with a lattice parameter of 2.84 Å (106). The fact that the atomic diameter of Re in its own lattice is 2.74 Å (107) suggests that the unit cell might contain Re atoms at the corners with carbon occupying some internal position(s). The cube center would seem the most likely carbon position (CsCl structure). This position is 2.0 Å in diameter along the cube diagonal and, since the carbon atom is generally taken to be 1.52 Å in diameter, there is ample room for the carbon atom. The stoichiometry could not be determined from the relative intensities of the diffraction patterns because of their discontinuous nature and the large difference in atomic scattering factors. Chemical analyses were not attempted because of the small amount present; however, electron microprobe analysis might be appropriate here.

There have been some indications that Re will form a carbide under certain circumstances. A carbide of Re has been reported to form between 470 and 600°C with "activated Re" and CO gas, but it decomposed above 1600°C (109). Other workers have observed an unknown phase(s) in the Re-W-C system, but their reported x-ray diffraction lines do not correspond to any of the strong lines of

the new phase (110). Kempter and Nadler (111) reported that carbides of Ru and Os, isomorphous with hexagonal WC, can be produced under certain pressure and temperature conditions. With the exception of Tc, about which little is known, the findings of Kempter and Nadler leave Re completely surrounded by carbide formers in the periodic table, another indication that Re might form a carbide - not necessarily a stable one - under certain conditions. Another indication that a carbide of Re would be metastable has been given by Searcy and Finnie (112) who postulated that the heat of formation of carbides of the Pt group metals (Ru, Os, Rh, Ir, Pd, Pt) and Re should be positive.

All of the above evidence strongly indicates that the new phase is a carbide of Re. If that is the case, then the melted structure shown in Fig. 3 must be the results of a eutectic reaction. The melted structure cannot be the result of a peritectic reaction because the reaction occurred below the melting point of pure Re. The graphite flakes within the carbide must have been produced by precipitation from the carbide on cooling; precipitation of carbon flakes often occurs upon cooling carbon-saturated phases (113). The rhenium-rhenium carbide eutectic temperature was not accurately determined in this study, but as indicated by couples 1 and 2, it must lie between 1800 and 2100°C, which is below the rhenium-carbon eutectic temperature of 2480°C (103). This low eutectic temperature is further evidence that rhenium carbide is metastable because, as demonstrated by the metastable Fe-Fe₃C phase diagram relative to the stable Fe-C phase diagram (109), phase reactions with metastable compounds occur at lower temperatures than do reactions with stable compounds.

To summarize, metallic rhenium will react with PG and graphite, near 2100°C to produce a previously unreported phase. This new phase is gray in color, is attacked by chromic acid, and produces a Debye-Scherrer pattern consistent with a simple cubic lattice with a unit cell edge of $2.8 \pm \text{A}$. There were many indications that this new phase is a metastable carbide of rhenium but the stoichiometry of the carbide could not be determined.

C. Diffusion Studies with Re

As noted in Chapter IV, Re was initially selected for the diffusion studies because of its low vapor pressure and fairly convenient radioactive isotope. Techniques for preparing, annealing, and sectioning specimens were developed for Re diffusion, and the details of these techniques are described in Chapter VI. Some observations made during the course of the Re diffusion study are presented here.

PG specimens approximately one cm^2 were prepared by grinding and lapping as described in Chapter VI. Following preparation, the edges of the samples were coated with a vinyl emulsion and the radioactive Re electro-deposited from a 0.1 N HNO_3 acid solution containing 10^{-9} molar HReO_4 . Deposition occurred with the PG as either the anode or the cathode. When PG was used as the anode, it was attacked by the nascent oxygen and the surface was covered with a thin layer of PG powder. Deposition with PG as the anode was probably just HReO_4 in solution trapped in the cracks and around the particles left by the oxygen attack. For short deposition times, the damage caused by the nascent oxygen

was slight, and anodic deposition was used in most of the experiments because it appeared to be more efficient. The method of deposition affected the resolution of the interface slightly but did not seem to affect the diffusion of Re into the PG. Following deposition, the vinyl emulsion was stripped from the PG and the specimens were given diffusion anneals at high temperature (1100 to 1800°C).

As described in Chapter VI, sections were ground from the samples. In the initial lapping experiments, the ground surface of each specimen was cleaned with pressure-sensitive mylar tape under fingertip pressure. Later, it was discovered that the uneven pressure left a residue of radioactive material from the previous section on the sample surface. Because the activity of the Re remaining on the surface was very high, this small residue significantly distorted the measured concentration profile. With this distortion, the logarithm of the apparent concentration decreased linearly with distance over three to five decades and extended into the specimen approximately 2×10^{-3} in. When the cleaning pressure was applied uniformly over the surface with a flat platen, the amount of residue was decreased considerably, leading to better resolution of the interface, as shown in Fig. 4.

A fairly flat tail was observed beyond the initial false profile, but the activity was of the order of 10 c/m. Because of this low activity, the slope of the line could not be resolved within reasonable counting times. It was assumed that this flat portion represented true diffusion of Re into PG, possibly distorted by edge effects; but the activity was deemed too low to warrant continuing the experiments.

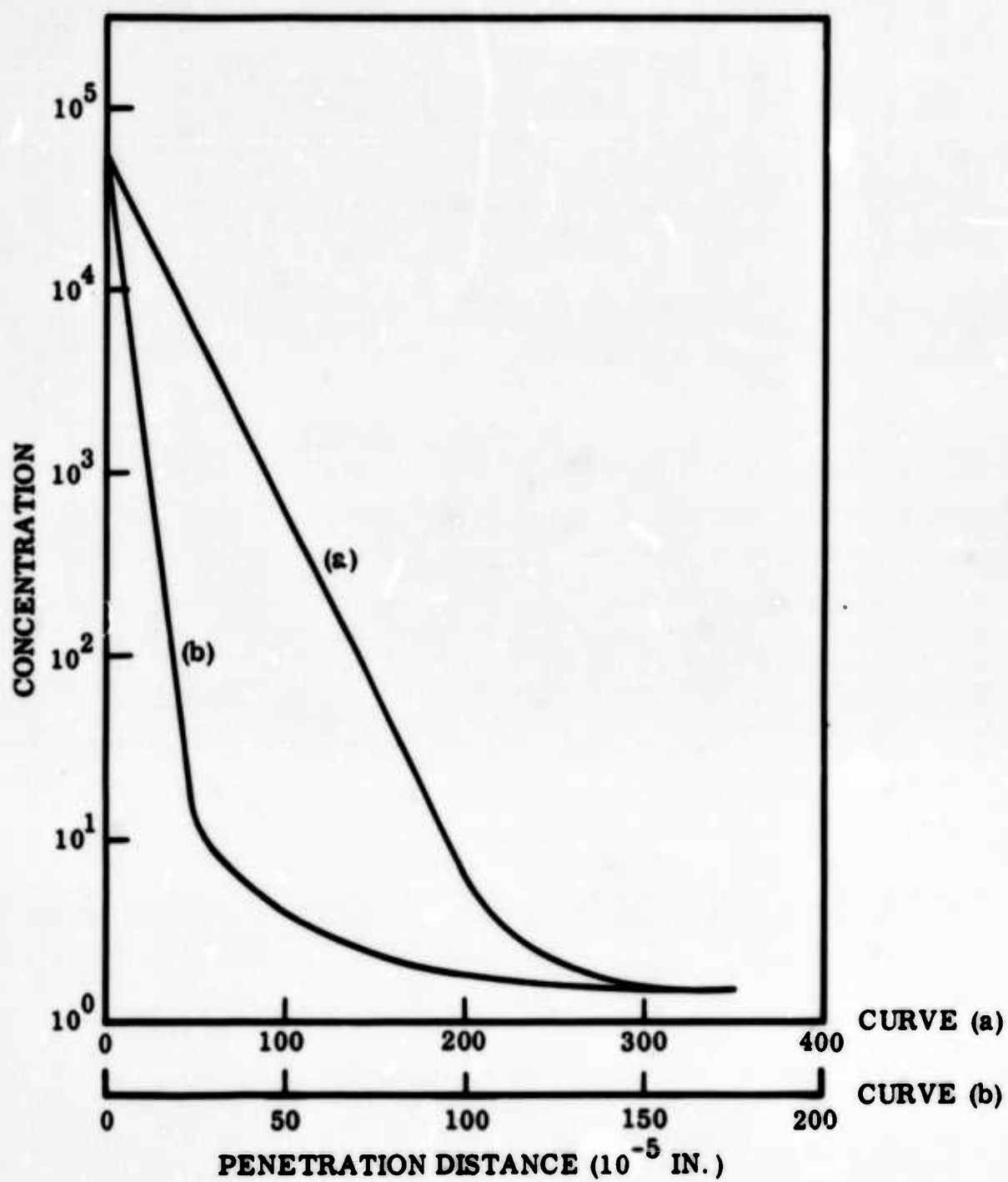


Fig. 4 Schematic Concentration Profiles for Re-186 Diffusion in PG.
**Curve (a) False Profile Caused by Non-uniform Pressure
 Applied During Cleaning Operation.**
Curve (b) Resolution of Interface With Uniform Pressure

To increase the counting rates, either the area of the samples had to be increased by a factor of 100 or the specific activity of the metal had to be increased by a similar amount. It was not practical to work with large specimens, and Re with a high specific activity could only be produced at considerable expense. Therefore, another readily available metal with much higher specific activity was sought. As discussed in Chapter IV, carrier-free Nb-95 satisfied these requirements. Furthermore, the Nb produced counting rates of 1000 to 5000 c/m for the same conditions under which Re produced 10 c/m. As a result, Nb-95 was used to study metal diffusion in PG.

Chapter VI

EXPERIMENTAL PROCEDURES

A. Structural Characterizations

1. Microstructure

Separate specimens from each PG, as-deposited (AD) and heat-treated (HT), were mounted for observation on the plane of the deposit and perpendicular to it. Specimens polished perpendicular to the plane of the deposit first had their deposition plane surface prepared as if they were to be used in a diffusion couple. Thus, any subsurface effects of diffusion sample preparation could be observed. The specimens were mounted in an epoxy-resin under vacuum. They were then ground through 600 grit paper, given a 1μ diamond polish, and then given a final polish with Cer-Cre* and chromic acid. Details of the metallographic technique have been published elsewhere (114). Each specimen was examined for diffusion sample preparation effects, as noted above; photomicrographs were then taken at 10, 100, and 1000X under polarized light, at approximately 15 deg from extinction. The structure produced by polishing the plane parallel to the deposition surface did not clearly show the nodular structure of PG, and this technique was abandoned in favor of cleaving the specimens parallel to the deposition surface with a razor blade.

*Burrell Corporation, 2223 Fifth Avenue, Pittsburgh, Pa.

2. Transmission Electron Microscopy

Specimens for transmission electron microscopy were obtained by touching a collodion-covered grid to the PG powder produced when a sample was ground in the Goldstein apparatus*. In order to have large flakes for observation, only samples which had been ground on the plane parallel to the deposition surface were used. The specimens were examined in transmission using an Hitachi HU-11 electron microscope operating at 100 kV.

3. X-ray Diffraction Studies

In this section, the procedures for determining the stacking error probability, unit cell parameters, crystallite size, degree of preferred orientation, and orientation dependence of structure will be given.

As discussed in Chapter III, the stacking error probability, p , in graphitic carbons can be experimentally related to the observed interlayer spacing (Fig. 2) and, to some extent, related by theory. Because PG is also a graphitic carbon, this observed dependence will be used to determine p . The use of Fig. 2 requires the determination of a precise value of d_{0002} . Accurate d_{0002} values were determined by extrapolating the d-spacing obtained from the 0002, 0004, 0006, and, where possible, 0008 diffraction peaks to $2\theta = 180$ deg using the Taylor-Sinclair function to provide a linear extrapolation (115). The diffraction profiles were obtained with a General Electric XRD-5 diffraction unit with a Ni-filtered Cu radiation, line source. The peaks were scanned automatically with a low time constant (0.5 seconds) and slow scanning speed (0.1 deg/min)

*See Section B-1 of this Chapter.

for the 0002 and 0004 profiles, and fast speeds (1 deg/min) for the 0006 and 0008 profiles. The slit system utilized the 0.4 deg beam slit, high-resolution Soller slit, and 0.1 deg receiving slit. The specimens were 1 mm-thick, flat slabs with faces parallel to the deposition plane, and they were placed in the usual symmetric Bragg reflection geometry. After a precise value of d_{0002} had been obtained, the solid line in Fig. 2 was used to determine p .

The a parameter was determined from the 10 and 11 bands in PG by point counting at 0.1 deg increments in the vicinity of the peak maximum. As noted in Chapter III, the d-spacing correction for the hk bands is negligible for PG with a crystallite size greater than 100 Å.

There are two crystallite dimensions to be measured in graphites: the thickness, L_c , and a characteristic diameter, L_a . The thickness, L_c , was determined from the 0002, 0004, and 0006 profiles. These profiles were smoothed by hand, and the integrated intensity, $I(\alpha)$, integral breadth, B , and center of gravity, $\bar{2\theta}$, were calculated using the trapezoidal rule and appropriate equations

$$I(\alpha) = \sum P(2\theta) \Delta 2\theta$$

$$B = I(\alpha)/I_{\max}$$

$$\bar{2\theta} = \frac{\sum 2\theta P(2\theta) \Delta 2\theta}{I(\alpha)}$$

Here $P(2\theta)$ is the height of the profile at 2θ and I_{\max} the peak height. The integral breadth was corrected by use of the Warren (87) correction

$$\beta^2 = B^2 - b^2$$

which, when applied to the 0002 profile, was found to give results similar to those of the more rigorous Fourier analysis (see Chapter III). Crystallite thicknesses were then computed with the Scherrer equation, using the corrected integral breadth β

$$L_c = \frac{\lambda}{\beta \cos \theta}$$

The value of b was taken from a strain-annealed PG specimen with the same orientation and similar in size to the regular specimens. When standards of the same absorption coefficient and geometry are used to correct integral breadths, separate absorption corrections are not needed. If the absorption effects are so large that the $\alpha_1\alpha_2$ doublet does not noticeably distort the standard profile, then this correction need not be made either. These simplifications were applicable for the PG line breadths in this part of the study. With the use of equations developed by Bragg and Packer (93), the 0002 standard profile was corrected for absorption and found to be only 10% greater than the diffraction profile of a polycrystalline quartz standard. This result was taken as sufficient justification to use the strain-annealed PG as the standard. The absorption corrections were programmed by Scott and Sackman, and calculated on a General Electric Computer System (116).

The 10 and 11 peaks in PG, obtained from flat specimens cut perpendicular to the deposition plane, were used to determine the crystallite diameter, L_a . With the specimens in the symmetric Bragg reflection geometry, the profiles were determined by point counting at 0.2 deg increments. The various

corrections for these profiles were applied in the following order:

1. Backgrounds, determined at the low 2θ side of the hk profile
2. Absorption*, corrected with the relation derived by Bragg and Packer (3) and programmed by Sackman and Scott (116)
3. $\alpha_1 \alpha_2$ doublet, corrected with the Rachinger equation (91)
4. Preferred orientation, corrected with the equation derived by Guentert and Cvickevich (92)
5. Instrumental broadening, corrected with the Warren correction (90),
$$\beta^2 = B^2 - b^2$$
 with the 220 line of NaCl and 331 line of Si as standards.

The $\alpha_1 \alpha_2$ doublet was also corrected in the standards.

The correction for preferred orientation requires that the pole figure data (described later) be represented as $I = I_0 \cos^m \alpha$. The value of m was determined from a log-log plot of I vs $\cos \alpha$.

Small, rectangular specimens, 0.5 mm \times 0.5 mm \times 20 mm, were used for studying preferred orientation. The specimens were prepared by mounting larger pieces on a slotted metal bar with hot wax and abrading them against fine emery paper backed with a flat platen. The specimens were cut so that two of the faces were parallel to the deposition surface. These small rectangular specimens were placed in a two-circle goniometer and, utilizing the rectangular symmetry, were optically aligned in the G.E. XRD-5 X-ray Diffractometer. Further refinement in the alignment was made until the 0002 profiles from

*The mass absorption coefficient used in these corrections was 4.15, as reported by Chipman (117).

opposite sides of the samples peaked at the same 2θ , within 0.01 deg, and the intensities were the same within 20% of each other. With the samples properly aligned, the 0002 line profiles were scanned at increments of 5 deg in α , the angle between the normals of the deposition plane and those crystallites causing diffraction. At each increment in α , the integrated intensity, integral breadth, and center of gravity were computed using the trapezoidal rule as above. With these data, linear plots of $\log I(\alpha)$ vs α^2 were made with the intensities normalized to $I(0) = 100$ and the mean crystallite tilt angles, defined by

$$\langle \alpha^2 \rangle^{1/2} = \left(\frac{\int_0^\infty \alpha^2 I(\alpha) d\alpha}{\int_0^\infty I(\alpha) d\alpha} \right)^{1/2}$$

$$I(\alpha) = I_0 \exp - (\alpha^2 / 2 \langle \alpha^2 \rangle)$$

were calculated from the linear plots. Past experience (5) and data taken here showed that $\langle \alpha^2 \rangle^{1/2}$ is insensitive to the specimen size over the range 0.5 to 1.0 mm, indicating that with the above arrangement there is no effect of specimen geometry on the pole figure below 1 mm specimen thickness.

The orientation dependence of structure as noted by plotting the values of p derived from the d-spacings and the observed integral breadths vs α . The integral breadths were not corrected for the various effects, but any significant changes with α would show in the uncorrected values.

4. Small Angle Scattering

Small angle scattering of x-rays by PG was measured with a special fixture designed by Bragg (118) for the Norelco X-ray Diffraction machine. The slit system limits the incident beam to 1/12 deg divergence and also limits the aperture at the receiving slit to 1/6 deg. The fixture permits very precise and reproducible adjustment of the slit system so data can be taken very close to $2\theta = 0$. Specimens 5 mm \times 30 mm \times 1 mm thick were prepared parallel and perpendicular to the plane of deposit and were the same specimens as those on which the unit cell dimensions, crystallite sizes, and densities were measured. Data were taken by point counting with the Norelco Geiger Counter and were then corrected for counting losses and background. The background was determined by placing two thicknesses of pure, annealed Al foil (0.075 mm total thickness) in the specimen position and point counting in the same range in which the small angle scattering data were taken. The transmittances of the Al and PG samples were determined by measuring the attenuation of the diffracted beam from the 111 planes of quartz, using Ni-filtered Cu radiation. All the transmittances were 0.40 ± 0.02 so relative transmittance corrections did not have to be made. To be certain that the Al foil did not produce any scattering of its own, the background was observed with and without the Al foil and for angles greater than 0.12 deg 2θ ; the transmittance of the Al was the same as that determined with the monochromatic radiation.

5. Other Structural Parameters

The structure of each PG was further characterized using Hg porosimetry and bulk density measurements.

Small specimens (5 mm \times 5 mm \times 1 mm) of each PG in the as-deposited and heat-treated conditions were separately placed in the penetrometer of an Aminco Hg porosimeter and the volume displaced in Hg at pressures between 1.8 and 5000 psi pressure was measured.

The bulk densities of three specimens from each PG, as-deposited and heat-treated, were determined by drilling a hole in the end of each specimen, suspending it from a small wire, and weighing it in and out of isopropyl alcohol. The weighing was done to the nearest 0.01 mg with a total sample weight larger than 0.20 gm.

B. Diffusion Measurements

1. Method of Measuring Diffusion Coefficients

A summary of methods of measuring the diffusion coefficient, D , in solids has recently been given by Cadek (119). Most of the techniques he described involve determining the composition profile by any of several methods, but various techniques have also been developed in which D is computed from the decrease in surface activity or from the total amount of material that has diffused into or out of a phase. All the latter methods assume the nature of the composition profile, and the assumptions are exact only for self-diffusion in a single crystal. To be certain of the interpretation of the results, the composition profiles for metal diffusion in PG had to be determined.

Profile determinations can be divided into two general categories: those in which the sample is divided into several sections perpendicular to the mass flux with subsequent analysis of each section, and those in which the specimen is sectioned only once parallel to the flux with the composition gradient determined by measuring some property related to the composition. Properties commonly used for this determination include hardness, color, autoradiographic intensity, and fluorescent x-ray intensity excited by x-rays or an electron beam. Because the very small concentration of diffusing species in PG determined the second of these categories, a method of sectioning perpendicular to the mass flux was sought, to be combined with tracer analytical techniques. A propagation of error analysis (120, 121) showed that the best techniques were those involving related weight measurements (determining the weight loss of the sample after each sectioning) and related thickness measurements (determining the sample thickness after each sectioning). The related thickness measurement technique was chosen because the density of PG is low and potentially variable, and PG produces fine dust upon grinding which could cause difficulties in the weight measurements by adhering to the sample. If sufficient weight were removed with each section, this dust would not be a problem; however, larger samples and/or greater penetration would be required. In any case, a thickness measurement is faster and more convenient than a precision weight measurement. The method used employed a precision lapping device built by Gomez (122) and similar to one described by Goldstein (123). The amount removed with each section and the penetration distances were measured with a high sensitivity dial gage.

2. Sample Preparation Prior to Diffusion

Nearly flat sheets of PG, 10 cm \times 10 cm \times 1 cm thick were cut into 0.7 cm square specimens. The original sheets had a slight cylindrical curvature, and the first long cuts were made parallel to the axis of the cylindrical curve to minimize its influence. Some specimens from each of the PG's were then given a graphitization heat treatment at 2700°C for 15 minutes. These specimens were labeled HT (Heat-Treated) and the untreated samples, AD (As-Deposited).

The Goldstein apparatus (122, 123) consisted of a rotating shaft perpendicular to a small table upon which a circular glass flat was eccentrically rotated. A cylindrical precision-ground hardened-steel holder was made to just fit onto the shaft, the holder's top and bottom faces being precisely perpendicular to the shaft axis and parallel to the glass flat surface. The holder was 1/2 inch in diameter, the shaft fitted into the holder along 3/4 in. of its length, and the faces of the holder were parallel within 1×10^{-5} in. and perpendicular to the shaft axis within $\pm 2 \times 10^{-5}$ radians.

For diffusion perpendicular to the deposition plane (to be labeled the <c> direction) the specimen faces perpendicular to the intended flux were ground flat and parallel. First, the substrate surface was attached to the holder with hot wax and the final deposition surface ground flat with adhesive 240 grit paper which was smoothly affixed to the circular glass flat. The specimen was then removed, remounted for grinding the substrate surface, and then remounted again for final preparation of the surface nearest the final deposition surface.

In this fashion, the resulting diffusion flux was perpendicular to the substrate surface and, thereby, parallel to the c-axis of most of the crystallites (see preferred orientation results).

For diffusion parallel to the deposition plane (to be noted by $\langle a \rangle$) the specimens were first mounted on one edge, ground, then mounted on the other edge and given the final preparation. Care was taken to ensure that the finished surface was perpendicular to the substrate surface. Because the initial nucleation layer did not have the same structure as the rest of the PG it was removed after the final surface preparation by grinding.

Considerable care was taken to ensure that the flat specimens were attached parallel to the holder face and glass flat. The holder was heated to about 200°C on a hot plate, and a small amount of Apiezon wax melted on its flat surface. With the holder held with one pair of tweezers, a hot specimen was put down onto the melted wax and moved back and forth until intimate, uniform contact with the holder was established. The specimen tweezers were then carefully removed and the holder set on a copper plate to cool. With this technique, specimens could be removed and replaced on the holder with less than 7μ variation over the entire surface.

Final preparation consisted of grinding through 4/0 paper and giving the specimen a metallographic polish with Cer-Cre and chromic acid on slipper satin. The adhesive paper was smoothly attached to the glass flat. The abrasive paper was affixed to the flat and a piece of ordinary paper placed over the abrasive. Then, the adhesive paper was smoothed by pressing it against the straight edge

of a glass sheet and dragging it across that edge. The ordinary paper on top of the abrasive prevented raking off the abrasive. Non-adhesive 3/0 and 4/0 papers were affixed with cellophane tape at two edges. The glass flat for metallographic polishing was prepared by affixing a layered structure of slipper satin, parafilm, and double-back masking tape to it under heat and pressure. The grinding action took place with only the weight of the steel shaft (1 cm diameter by 15 cm long) on the specimen but faster metallographic polishing occurred with an additional weight of about 300 grams.

The tracer was deposited on the metallographically polished surface by evaporating a drop of suitably diluted Nb-oxalate solution procured from the Oak Ridge Radioisotope Facility (104). Controlled amounts were deposited with a 0.050 cm^3 pipette, and about $50 \times 10^3 \text{ c/m}$ were deposited on each specimen.

3. Furnace Description and Annealing Procedure

The furnace used for the heat-treatment and diffusion anneals consisted of a vertical graphite resistance element, with power supplied at water-cooled clamps located at one end of the element. The cylindrical element was uniformly slotted in several places to provide a longer resistance path, and two sighting slits approximately 1/4 in. \times 2 in. were located in the element. The furnace was originally built for tensile testing at 3000°C , and the sighting slits were designed for observing the specimen gage length. The furnace was equipped with a 50 kW power supply, mechanical and diffusion vacuum pumps, He gas

supply, provision for protecting the quartz sight glasses from contamination, and a quenching chamber with an air-lock. Considerable insulation was supplied by several concentric shells of graphite with the volume in between filled with graphite felt.

The furnace power was controlled by a saturable reactor, and an integral-plus-proportional controller, designed by W.E. Eppler of LMSC, which provided $\pm 5^{\circ}\text{C}$ control. A Pyro-Eye two-color pyrometer was used to monitor the temperature. The field of view of the two-color pyrometer was too large to include only the specimen holder surface; as a result, some drift of holder temperature resulted from monitoring the combined heater plus sample temperature. This drift was corrected by hand and was less than 30° total variation in all but one case, when a 50° variation occurred.

For the diffusion anneals, the specimens were placed face to face in a cylindrical graphite holder which was attached, by pinned connections, to a 0.5 cm diameter \times 15 cm long graphite rod. This rod, in turn, was attached to a water-cooled copper plunger that extended out of the furnace through a sliding vacuum seal.

To anneal specimens, the holder was placed in the hot zone, the furnace evacuated, and the temperature then increased manually to near the desired temperature. At 1200°C , the vacuum valve was closed and the system brought to a gage pressure of -10 inches of Hg with pure He gas. The heatup under vacuum served to reduce the Nb-oxalate and to purify the furnace atmosphere while the He gas served to prevent arcing at the higher temperatures, to provide

better heat transfer to the holder, and to reduce the tendency of the Nb-95 to vaporize during the anneal. Virtually all the Nb-95 remained on the samples; no appreciable activity could be detected on the holder or inside the furnace after an anneal. The high sensitivity of the controller required that, initially, the temperature be brought up manually. When the temperature came within 100°C of the desired temperature, however, the controller was put in the automatic mode with a manual override and the desired temperature reached automatically. The temperature was measured with a Micro-optical brightness pyrometer focused on a black-body hole located in the base of the holder, just below the specimens. Heatup time before the controller was introduced was about 15 minutes, with another 10 minutes being spent reaching the final temperature. No temperature overshoot was experienced with this heating method. Heatup time was a small fraction of the annealing times.

During the anneal, the temperature of the holder was monitored with the manual pyrometer and adjusted for the drift mentioned above. At the end of the anneal, the holder was raised out of the hot zone and into a water-cooled copper quench chamber where the holder cooled to below 700°C in about 30 seconds. When the holder had cooled to about 50°C (approximately 20 minutes), the couple was removed from the quench chamber through the air-lock. The time at temperature was measured to the nearest minute, with the initial time estimated as the time at which the temperature reached 20°C below the average temperature of the anneal.

The manual Micro-Optical pyrometer was calibrated with the sight glass against an NBS pyrometer lamp between 700 and 2200°C and then further calibration was accomplished by measuring the melting point of Pd and Mo pellets in contact with graphite in the furnace. Nadler and Kempter's data (124) on melting points of metals in contact with carbon was used as a reference. The temperature measurement errors are estimated as follows:

<u>Error</u>	<u>Temperature</u>
1. Due to lamp calibration	±7°C
2. Due to temperature drift during run	~10 - 30°C
3. Estimated total:	±15 to 30°C between 700 and 2200°C

The figures given above do not refer to the precision of a temperature measurement, which is better than ±5°C, but to the accuracy.

4. Sectioning Techniques

Prior to sectioning, approximately 1-1/2 mm was cut off the edges of the specimens with a jeweler's saw and a small steel miter box [WMB (17) and this study showed that edge effects can be appreciable in diffusion studies in PG]. Following edge removal, each specimen was mounted on the Goldstein device holder as described above, preparatory to lapping.

Prior to each lapping operation, the combined thickness of sample and holder was measured at three to six places on the sample surface with a dial gage accurate to $\pm 1 \times 10^{-5}$ in. (Starrett 25-106). The specimen and holder

were moved about on the dial gage table to eliminate small dirt particles and measurements were taken at the same points on the specimen. With this procedure the amount removed at a particular point could be measured to $\pm 1 \times 10^{-5}$ in. The specimens could be removed and replaced under the dial gage with the same thickness measurement obtained. Thermal expansion effects were estimated to be less than 10^{-5} in., because the room was air-conditioned and the sample was handled very little. These factors, combined with a fairly high thermal mass and low thermal conductivity, made thermal expansion effects negligible. The surface of the specimen was not perfectly flat but had a slight cone shape due to misalignment. This cone shape was less than 10×10^{-5} in. high at the center with a base diameter the size of the specimen (~0.375 in.).

The first lap was done with dry Cer-Cre on slipper satin to remove a maximum of undiffused material, if present, without scratching the surface and embedding the tracer in the scratches. The next lap was made with 4/0 paper and the next two with 3/0 paper. At this point, approximately $10 - 40 \times 10^{-5}$ in. total thickness was removed and this thickness is about equal to the error in replacing the specimen on the holder after the diffusion anneal. Following the preliminary lapping, the abrasive papers were selected according to the amount to be removed. The profiles were determined to depths of $3 - 30 \times 10^{-3}$ in. and were analyzed in 10 to 50 increments. Slight variations in surface flatness produced an average uncertainty in thickness removed of $\pm 2 \times 10^{-5}$ in., corresponding to a relative error of 10% or less.

After each grinding operation, the specimen was removed and the surface cleaned with Scotch-brand No. 56 yellow mylar pressure tape by pressing the sample face against the adhesive several times, using a 5 x 8 file card on a flat surface as the backing. (The use of a flat backing is very important as uneven pressure allows material to remain after each lap and, when most of the tracer has not diffused, this seriously distorts the composition profile.) The same piece of tape was then used to cover the small square of abrasive paper which contained the PG powder. Mylar tape has a peculiar advantage in that it acquires a static charge which attracts the PG powder. This property can be used to control the fine powder produced by grinding.

All the equipment used for radioactive counting was manufactured by Atomic Instrument Co., Baird Associates. The abrasive squares containing PG powder and Nb-95 were placed inside a hollow NaI scintillation counter (A.I.C. Model 810). The counting rate was measured with a β - γ spectrometer composed of A.I.C. Model 312 power supply, 215 amplifier, 510 pulse height analyzer, 134 high-speed scalar, and 630 precision timer. The pulse height analyzer was set to integrate over the 0.75 Mev γ peak of Nb between 0.70 and 0.84 Mev. With this arrangement, the counting efficiency was approximately 25%, based on the initial assay supplied by Oak Ridge. Counting rates for each section were less than 10,000 c/m; generally, at least 1000 total counts were taken on each lap to produce a standard deviation of approximately 5% for a counting rate as low as 300 c/m and background of 70 c/m (125). Sections were taken until the residual activity fell below 200 c/m.

The concentration of Nb-95 was computed by dividing the intensity by the average thickness removed; the distance from the original interface was computed from the mid-points of each lap.

5. Autoradiography

Autoradiographs were taken before and during lapping by placing the radioactive sample against Kodak projector slide plates and exposing for 2 to 800 hours, depending upon the intensity. Generally, the as-ground surfaces were used; on occasion, however, the surface was repolished before an autoradiograph was taken. Repolishing did not alter the appearance of the autoradiograph other than to improve its resolution. Copies of the autoradiographs were made by photographing the negatives at 10X using transmitted light and a bellows camera.

In this fashion, the relative film darkening is preserved, and the darker regions represent areas of higher Nb concentration.

Chapter VII

EXPERIMENTAL RESULTS - STRUCTURE

A. Microstructure

The microstructures of the as-deposited PG's used in this study are shown in Fig. 5 and the heat-treated structures are shown in Fig. 6. The magnification used in these photomicrographs is 10X. As may be seen, these PG's represent a variety of microstructures. The R277 material is characterized by a coarse substrate nucleated structure (structure A2 in Chapter III) with a moderately strong secondary structure. The R165 material is also substrate nucleated but has a fine primary structure and a strong secondary structure (structure C3). The R1 PG is a good example of regeneratively nucleated PG (F1). The as-deposited R277 PG shows a tendency to delaminate, as indicated by the photomicrographs perpendicular to the deposition plane.

As described in Chapter VI, the samples polished perpendicular to the deposition plane first had their deposition plane surface prepared as if to be used in a diffusion couple. The metallographic preparation of these samples was such that the edges could be examined within one micron of the surface prepared for diffusion. No distortion or damage due to the diffusion sample preparation was found.

The heat-treatment did not noticeably alter the structure as observed at 10X magnification (Fig. 6), but it did produce some sort of speckling over the

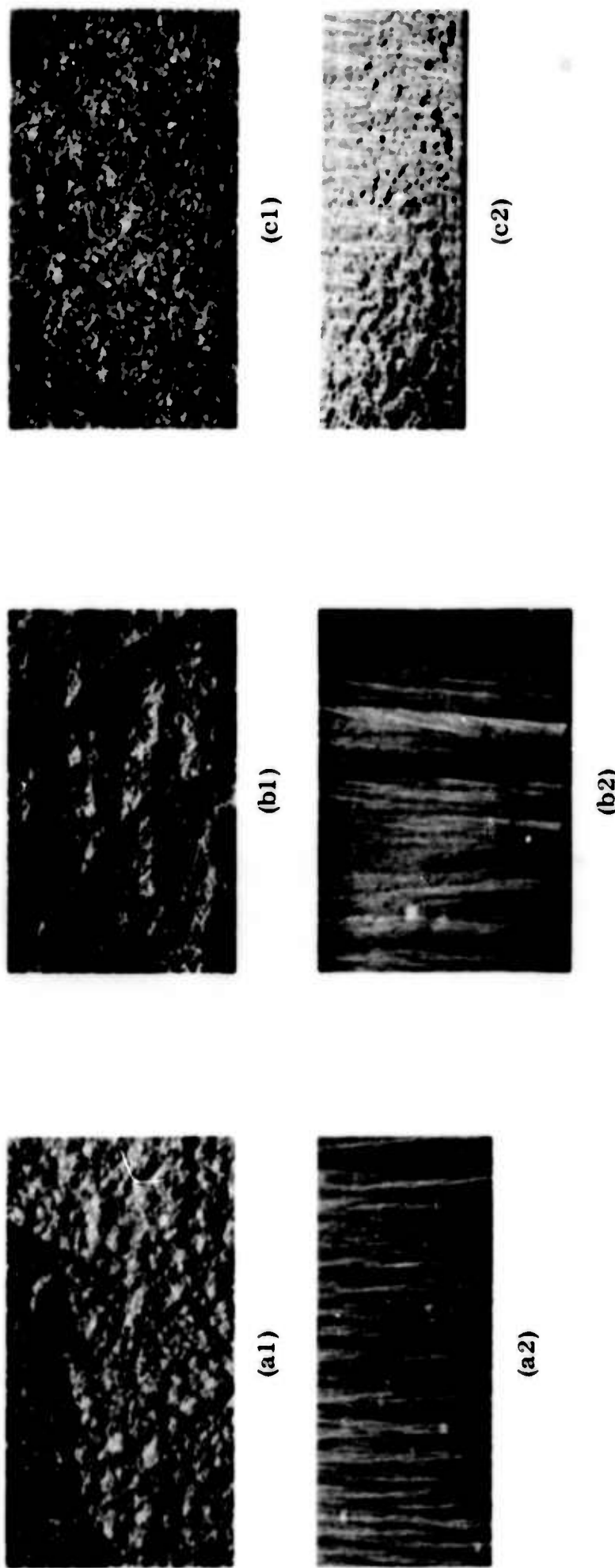
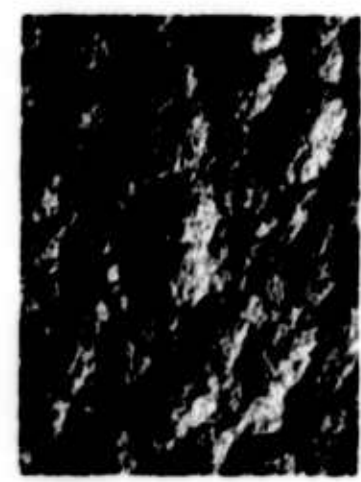


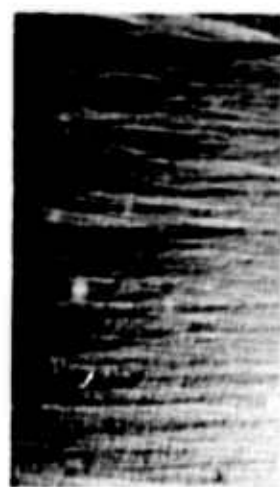
Fig. 5 Photomicrographs at 10X Magnification of As-deposited PG's Used in Study.
(a1), (a2): R165 PG Parallel and Perpendicular to Deposition Plane.
(b1), (b2): R277 PG. (c1), (c2): R1 PG



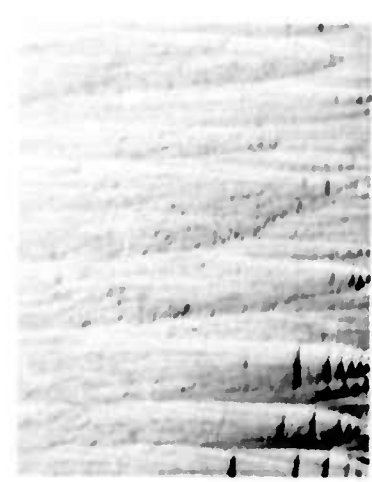
(a1)



(a2)



(b1)



(b2)

(c1)



(c2)

Fig. 6 Photomicrographs at 10X Magnification of Heat-treated PG's Used in Study.
(a1), (a2): R165 PG Parallel and Perpendicular to Depositon Plane.
(b1), (b2): R277 PG.
(c1), (c2): R1 PG

surface perpendicular to the deposition plane. The source of this speckling is not known, but it does not appear in the photomicrographs at higher magnification. The speckling is probably due to a shadow effect produced by slight depressions and the oblique lighting used to take these photographs. The tendency of R277 material to delaminate is further shown in the heat-treated samples, a similar effect being noted in the R1 PG. The R1 material actually consisted of a variety of structures, as shown in Fig. 6 - C2, where both substrate and regeneratively nucleated structures are in evidence.

Figures 7 through 12 are photomicrographs of each PG at 100 and 1000X magnification. The photomicrographs are arranged so that the as-deposited and heat-treated specimens of each PG in each orientation are together, and consecutive figures contain the views parallel and perpendicular to the deposition surface. The views parallel to the deposition plane are of cleavage surfaces, and cleavage defects cause some regions of the photographs to be out of focus. The main features to be noted in this series of photographs are the similarities of the R165 and R277 structures, as contrasted with the R1 PG, the lack of change in primary structure with heat-treatment, and the partial elimination of the finer secondary structure in the heat-treated material. The specimens were prepared and photographs by Mr. A.S. Gleason of LMSC.

B. Transmission Electron Microscopy

Figure 13 contains some transmission electron micrographs of R277 PG taken with an Hitachi HU-11 electron microscope operating at 100 kV. The powder used to obtain these samples came from a section out of a Nb diffusion



(a1)



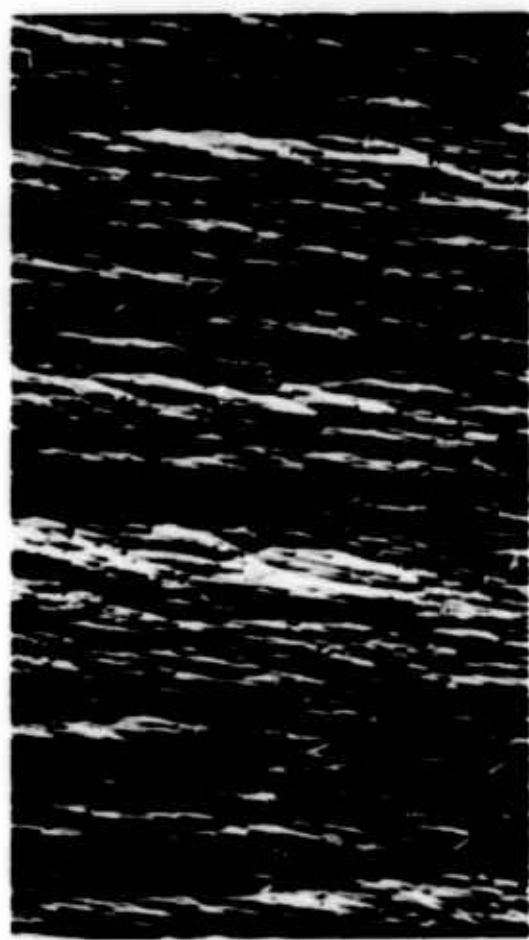
(b1)



(a2)

86

Fig. 7 Photomicrographs Parallel to Deposition Plane of R165 PG. (a1) As-deposited, 100X.
(a2) As-deposited, 1000X. (b1) Heat-treated, 100X. (b2) Heat-treated, 1000X



(a1)



(a2)



(b1)

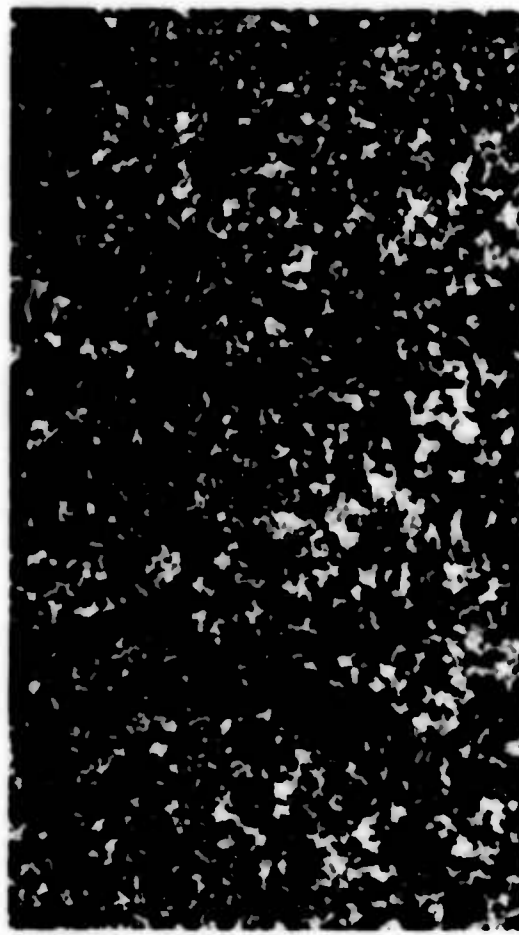


(b2)

Fig. 8 Photomicrographs Perpendicular to Deposition Plane of R165 PG. (a1) As-deposited, 100X.
(a2) As-deposited, 1000X. (b1) Heat-treated, 100X. (b2) Heat-treated, 1000X.



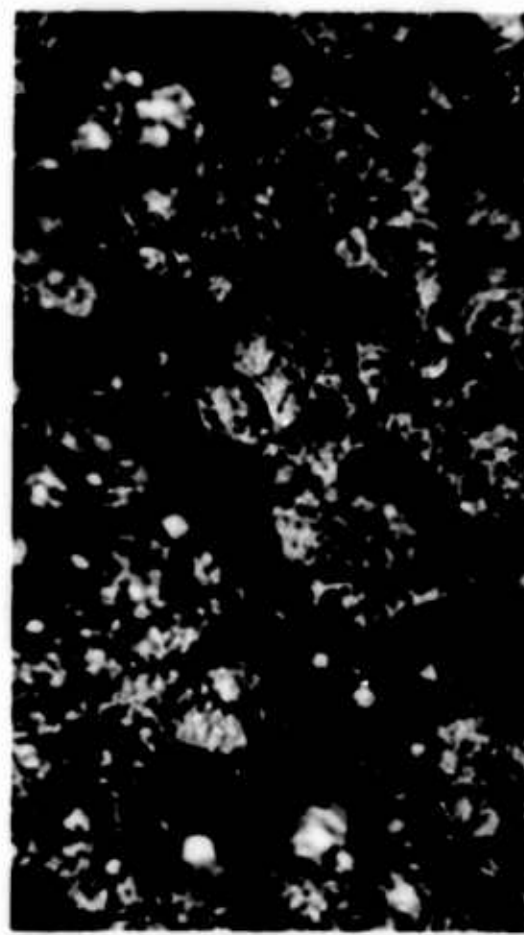
(a1)



(b1)

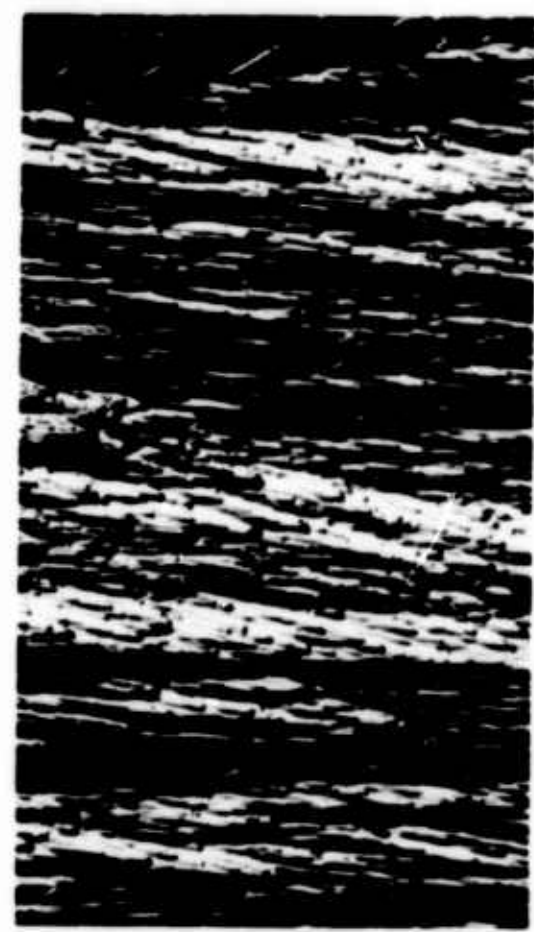


(a2)



(b2)

Fig. 9 Photomicrographs Parallel to Deposition Plane of R277 PG. (a1) As-deposited, 100X.
(a2) As-deposited, 1000X. (b1) Heat-treated, 100X. (b2) Heat-treated, 1000X



(b1)



(b2)



(a1)

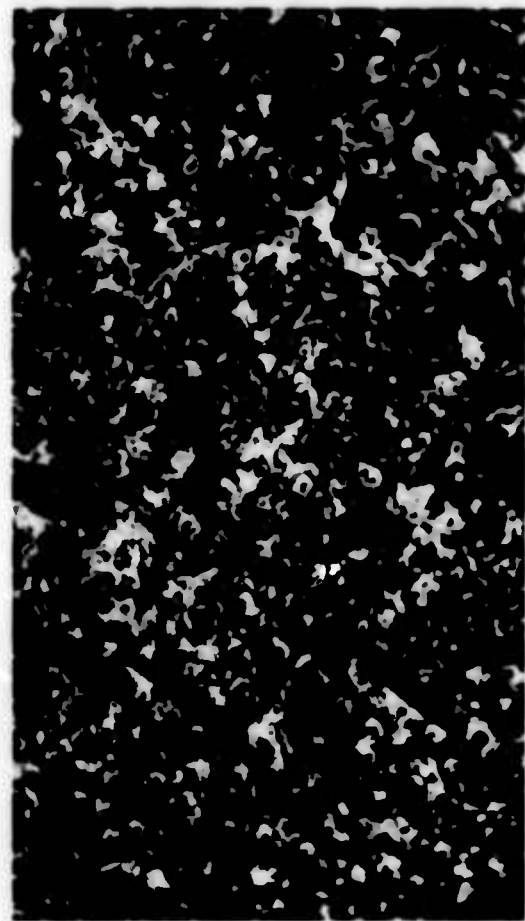


(a2)

Fig. 10 Photomicrographs Perpendicular to Deposition Plane of R277 PG. (a1) As-deposited, 100X.
(a2) As-deposited, 1000X. (b1) Heat-treated, 100X. (b2) Heat-treated, 1000X.



(a1)



(b1)



(a2)



(b2)

Fig. 11 Photomicrographs Parallel to Deposition Plane of R1 PG. (a1) As-deposited, 100X.
(a2) As-deposited, 1000X. (b1) Heat-treated, 100X. (b2) Heat-treated, 1000X.

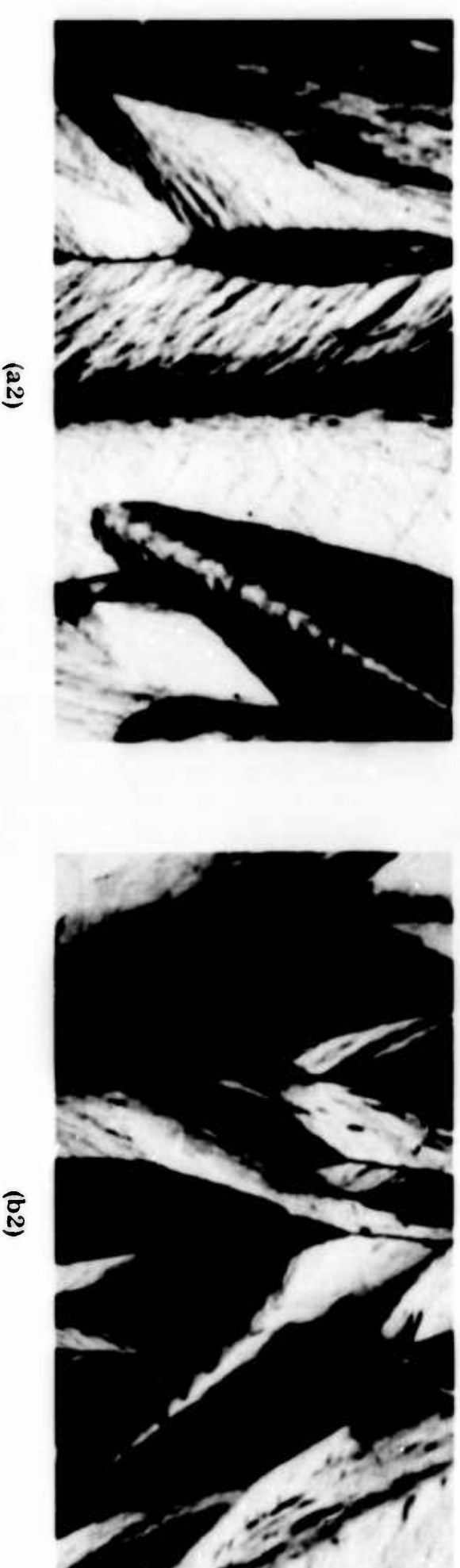


Fig. 12 Photomicrographs Perpendicular to Deposition Plane of R1 PG. (a1) As-deposited, 100X. (a2) Heat-treated, 100X. (b1) Heat-treated, 100X. (b2) Lifted-treated, 100X.

couple which was taken near the beginning of the composition profile. The material was examined to demonstrate the nodular, wrinkled sheet structure of the PG and to show the lack of evidence for clustering of Nb throughout the material. At 70,000X magnification, 150 Å diameter clusters would appear as 1 mm in diameter and could be easily resolved. The fact that clusters of this size or even smaller were not seen in PG flakes obtained near the beginning of the concentration gradients is taken to indicate one of the following possibilities:

1. The Nb is uniformly distributed in the PG
2. The Nb is distributed in clusters in the PG on a scale too fine to be resolved.
3. The Nb is concentrated in so few regions that the chances of observing it are rather small.

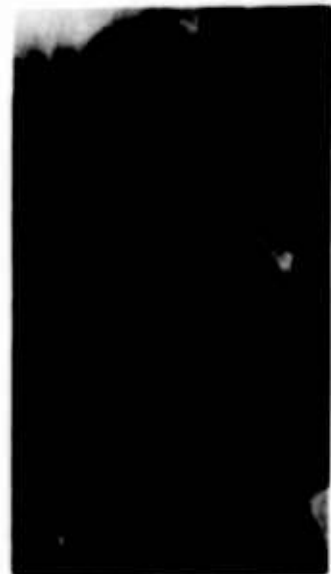
The only indication of high atomic weight clusters is shown in Fig. 13d. The structure is not well resolved and the nature of these dark regions is not known. The transmission electron micrographs were taken by Mr. P. F. Lindquist of LMSC.

C. X-ray Structure

A summary of the x-ray data is given in Tables 9, 10, 11. The as-deposited PG's are all characterized by a 90% stacking error probability (p), a crystallite thickness (L_c) of 170 Å, and a crystallite diameter (L_a) of 190 to 260 Å. The crystallite thicknesses were computed from the 0002 profile, as outlined in Chapter V. Similar calculations on the 0004 and 0006 profiles resulted in much smaller crystallite thicknesses, demonstrating that there is a spread



(a) 14,000X



(b) 53,000X



(c) 70,000X



(d) 70,000X

**Fig. 13 Transmission Electron Micrographs of R277 PG
Taken Near Beginning of Nb Concentration Gradients.
(a) 14,000X, (b) 53,000X, (c) 70,000X, (d) 70,000X**

in the interplanar spacings (60). The crystallite diameters were computed from the 10 and 11 profiles by the method given in Chapter VI. Of the corrections listed there, only the background, the $\alpha_1\alpha_2$ doublet, and the instrumental broadening corrections were important. The absorption correction increased the peak height and shifted it to higher 2θ but did not increase the breadth. The preferred orientation correction was found to be negligible for $(2\theta_{1/2 \text{ max}} - 2\theta_{\text{max}}) < 0.7 \text{ deg}$, which was the case for all the PG's in this study. The preferred orientation correction does not become important until $(2\theta - 2\theta_{\text{max}}) \sim 1 \text{ deg}$ and, because the $\alpha_1\alpha_2$ doublet correction is appreciable, the best procedure is to correct for the doublet first so that the preferred orientation correction is minimized.

The graphitizing heat treatment decreased p to 30% for the R165 and R277 PG's and 40% for the R1 material. The R1 PG varied somewhat in its response to the heat treatment due to the variable structure noted under metallography. This variation is also reflected in the two different values of p given in Table 9 for R1-HT specimens. The crystallite thicknesses increased two to three times upon heat treatment, with the R165 material showing the greatest change and R1 showing the least. The different responses to the heat treatment are also demonstrated by the hk bands plotted in Fig. 14, where the intensities of the R1 profiles are always less than those of the other two PG's even though the geometry in each case is identical. It was noted in Chapter III that there are no well-developed line broadening theories for the modulated hk bands of partially graphitized PG; however, the 11 bands in all three heat-treated PG's

Table 9
STACKING ERROR PROBABILITIES FOR PG USED IN THIS STUDY

PG	Position in Deposit	d_{0002}		p		Avg. for each PG
		Centroid	Peak	Centroid	Peak	
R165-AD	Top	3.423	3.427	0.92	0.94	0.9
R165-AD	Middle	3.427	3.423	0.94	0.92	
R165-AD	Bottom	3.423	3.430	0.92	0.96	
R165-HT	Top	3.366	3.360	0.32	0.18	0.3
R165-HT	Bottom	3.370	3.366	0.40	0.32	
R277-AD	Top	3.418	3.416	0.89	0.81	
R277-AD	Middle	3.416	3.418	0.81	0.89	0.9
R277-AD	Bottom	3.419	3.422	0.89	0.91	
R277-HT	Top	3.372	3.367	0.43	0.34	0.3
R277-HT	Middle	3.367	3.366	0.34	0.32	
R277-HT	Bottom	3.377	3.370	0.52	0.40	
R1-AD		3.435	3.427	0.98	0.94	0.9
R1-HT		3.383	3.381	0.58	0.56	0.6
R1-HT			3.369		0.40	0.4
H253-32	Strain-annealed standard	3.3560	3.3560	0.08	0.08	

Table 10
CRYSTALLITE SIZES FOR THE PG USED IN THIS STUDY

PG	Position in Deposit	Thickness - L _c			Average Thickness			Diameter		
		0002	0004	0006	0002	0004	0006	10	11	Avg.
R165-AD	Top	176A	81A	55A						
R165-AD	Middle	179	92	55	175	85	65	246	250	250
R165-AD	Bottom	176	82	81						
R165-HT	Top	493	175	183						
R165-HT	Bottom	484	175	143	485	175	155		595	595
R277-AD	Top	184	89							
R277-AD	Middle	163	95		165	90	65	268	262	265
R277-AD	Bottom	164	89	64						
R277-HT	Top	291	159							
R277-HT	Middle	339	155	98	325	150	100		595	595
R277-HT	Bottom	338	141							
R1-AR		171	87		170	85		201	182	190
R1-HT		215	121	92	210	120	90		463	460

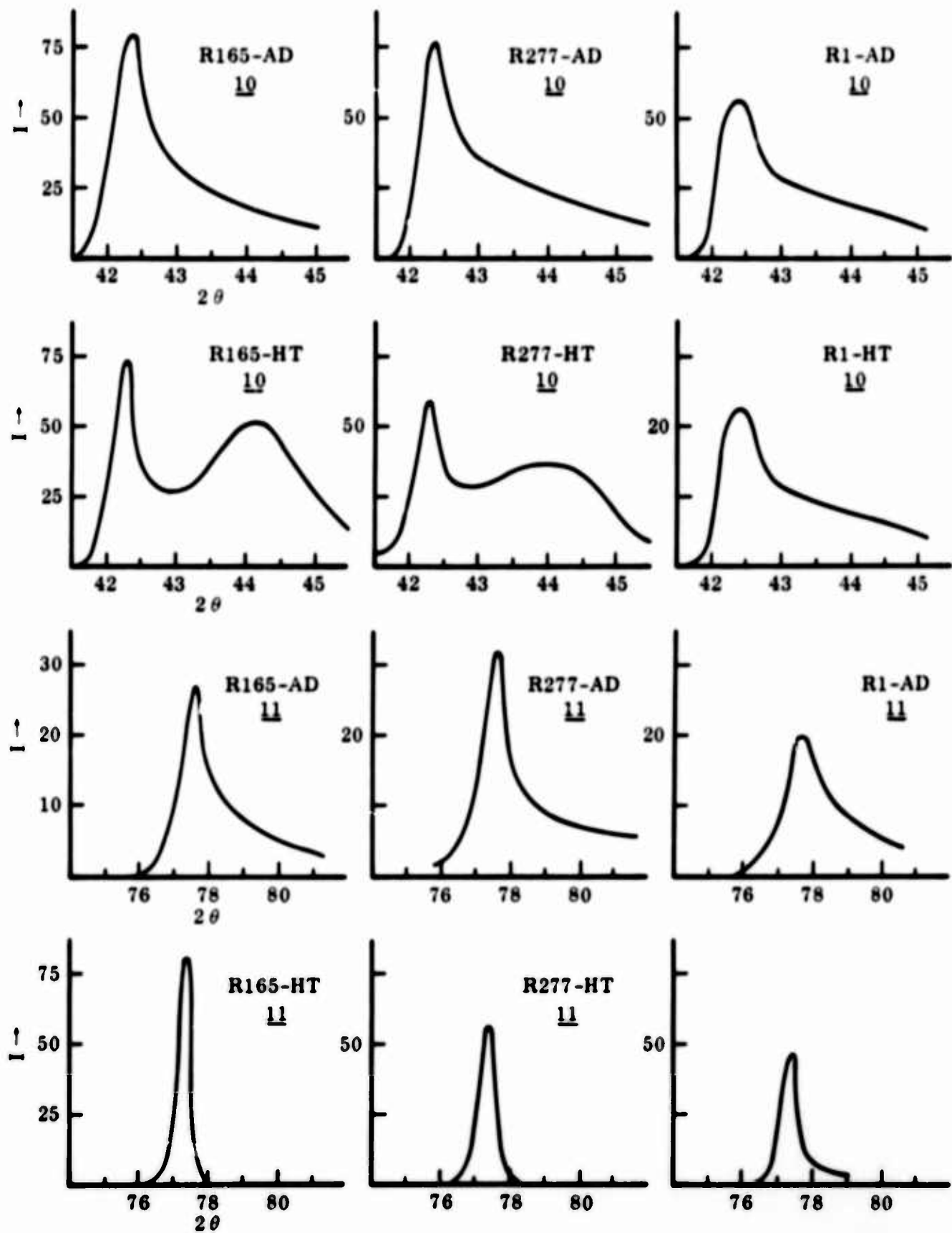


Fig. 14 Uncorrected $\bar{h}k$ Bands in PG

are rather sharp, and the line width at half-height could be used to approximate the crystallite diameter. The separation of the 110 and 111 peaks in graphite is about 6 deg 20' with CuK α radiation, the reason that the modulation effect is not very apparent. The crystallite diameters given in Table 10 for the heat-treated PG's were computed from the 11 bands, after correcting them for the $\alpha_1\alpha_2$ doublet, and instrumental broadening. The preferred orientation correction was not applied, and the numerical factor in the Scherrer equation was taken to be 1.84. As may be seen, the crystallite diameter apparently increased somewhat more than two-fold in all cases.

The results from the preferred orientation studies, with the texture interpreted as Gaussian distributions, are shown in Figs. 15 and 16 and Table 11. The value of m in the $\cos^m \alpha$ representation is also given in Table 11. In all cases, the R1 material has the broadest texture, and, of the as-deposited PG's, R277 has the sharpest texture. Upon graphitization, there is little difference between R165 and R277, but R1 still has the broadest texture.

The orientation dependence of the stacking error probability is given in Fig. 17. The as-deposited material exhibits very little orientation dependence while that for the heat-treated PG's is somewhat greater. The change in p is somewhat less than previously observed (5, 94) but not extraordinarily so. In the as-deposited material, the line breadths indicated a decrease in crystallite thickness of about 15% at $\alpha = 45$ deg and a 25% decrease for the heat-treated material. Although the changes in crystallite size and stacking error probability are definitely present, they are not large enough to warrant consideration at this time.

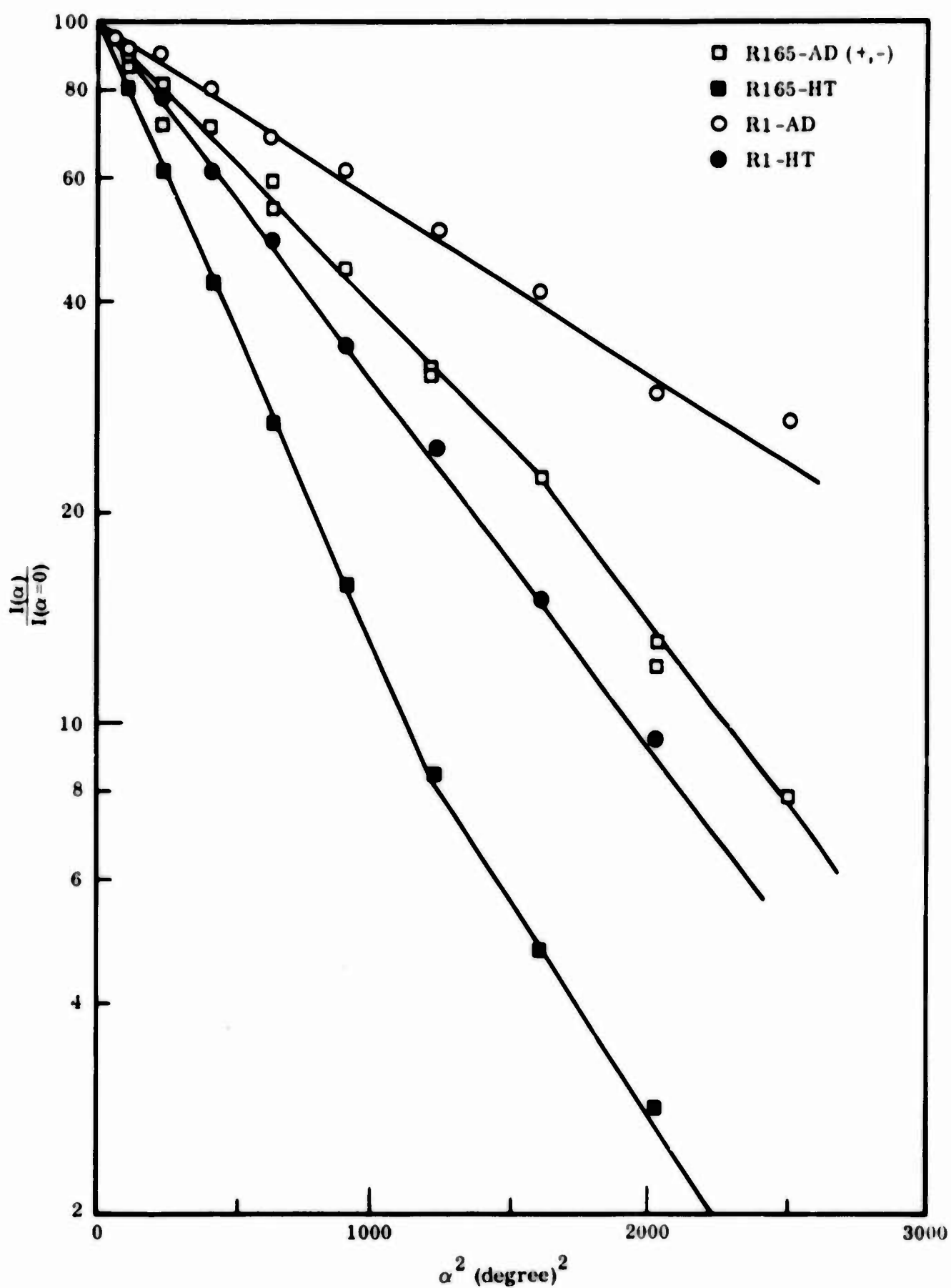


Fig. 15 0002 Pole Figures for R165 and R1 PG (α is angle away from deposition plane normal)

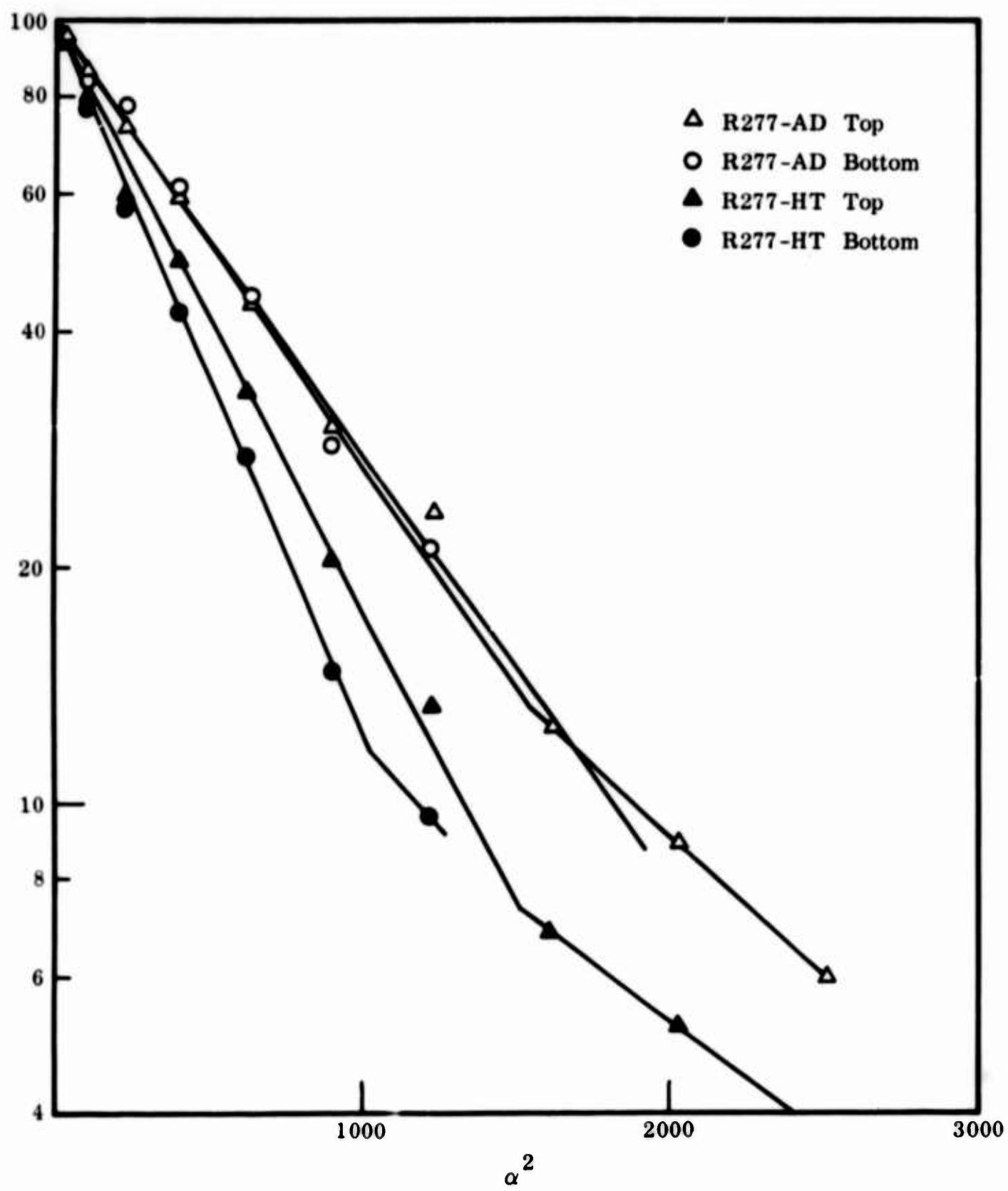


Fig. 16 0002 Pole Figures for R277 PG (α is the angle away from the deposition plane normal)

Table 11
**SUMMARY OF
 PREFERRED ORIENTATION DATA**

PG	Position in Deposit	Mean Tilt Angle $\langle \alpha^2 \rangle^{1/2}$	m
R165-AD	—	23.2°	5.4
R165-HT	—	15.5°	11.6
R277-AD	Top	19.4°	7.8
R277-AD	Bottom	19.5°	
R277-HT	Top	16.7°	9.2
R277-HT	Bottom	15.5°	
R1-AD	—	27.5°	3.6
R1-HT	—	20.6°	7.2

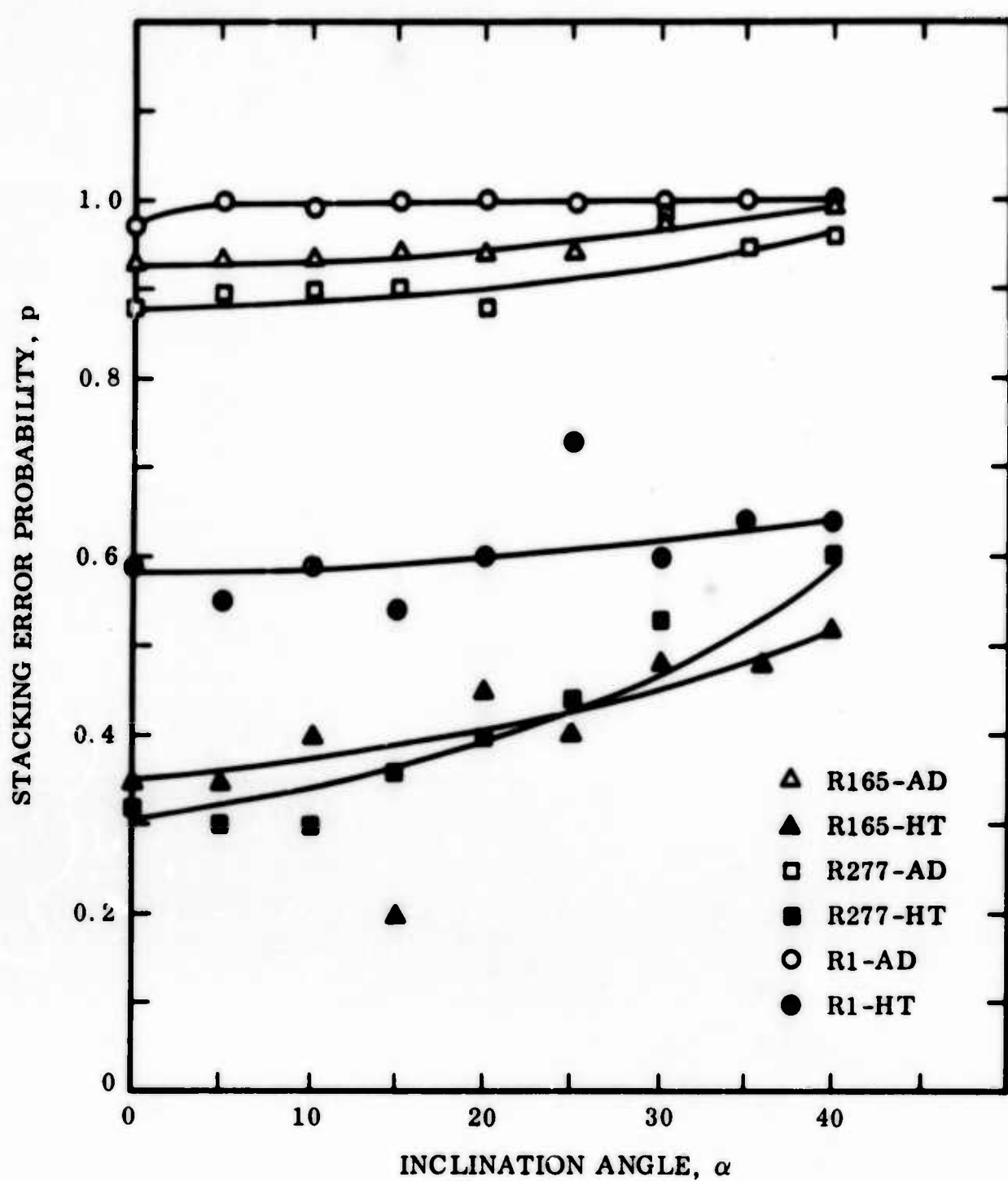


Fig. 17 Orientation Dependence of Stacking Error Probability

D. Small Angle Scattering

Small angle scattering of x-rays by solids or liquids is caused by heterogeneities in the electron density with dimensions from several tens to several hundred times the x-ray wave length (126, 127). These heterogeneities may be regions of high or low electron density; for example, in solids, the heterogeneities could be voids. X-rays are scattered out of the direct beam by less than 3 deg 2θ and careful collimation is required to allow data to be taken as close as 0.1 deg 2θ away from the beam. Small angle scattering data are generally described in terms of the diffraction vector $h = (4\pi \sin\theta)/\lambda$.

This h should not be confused with the \underline{h} used in the Miller indices notation.

Guinier (126) has shown that for small values of h , small angle scattering from a collection of fixed identical particles having the same orientation, behaves as

$$I = kNn^2 \exp(-h^2 \underline{D}^2)$$

where I is the intensity of the scatter x-rays, k a constant, N the total number of particles, n the number of electrons per particle, and \underline{D} the inertial distance of the particles relative to the plane of the incident beam.

This relationship is termed the Guinier approximation and is valid for $h\underline{D} < 1$.

For ellipsoids of revolution (126)

$$\underline{D}^2 = b^2/5$$

where b is the particle dimension perpendicular to the plane of the beam.

For x-ray beams possessing neither height nor width, the small angle scattering approaches an h^{-4} dependency at large h and a beam of infinite height distorts this asymptotic behavior to an h^{-3} dependency (126, 127). Bragg (128) has shown that, for freely moving mono-disperse particles, the onset of the asymptotic h^{-4} or h^{-3} dependency occurs at

$$hq \cong 4.0$$

where q is the smallest dimension of the particles. This approximation, which will be referred to as the Bragg approximation, can be extended to fixed particles having the same orientation (129) as

$$\frac{hb}{2} \sim 4.0$$

The data at intermediate h generally do not lend themselves to analysis; the equations given above, however, do provide two independent estimates of the particle size, one at small h and the other at large h .

Small angle scattering of x-rays can be complicated by the presence of doubly diffracted x-rays. This distortion is termed double Bragg scattering (127, 130). If the diffracting planes are aligned to give strong double Bragg diffraction, the initial portion of the small angle scattering data can be obscured.

Using the procedure described in Chapter VI, the small angle scattering of x-rays from as-deposited and heat-treated PG was measured with the plane of the beam both parallel and perpendicular to the deposition plane. The experimental configuration is shown schematically in Fig. 18, together with the data

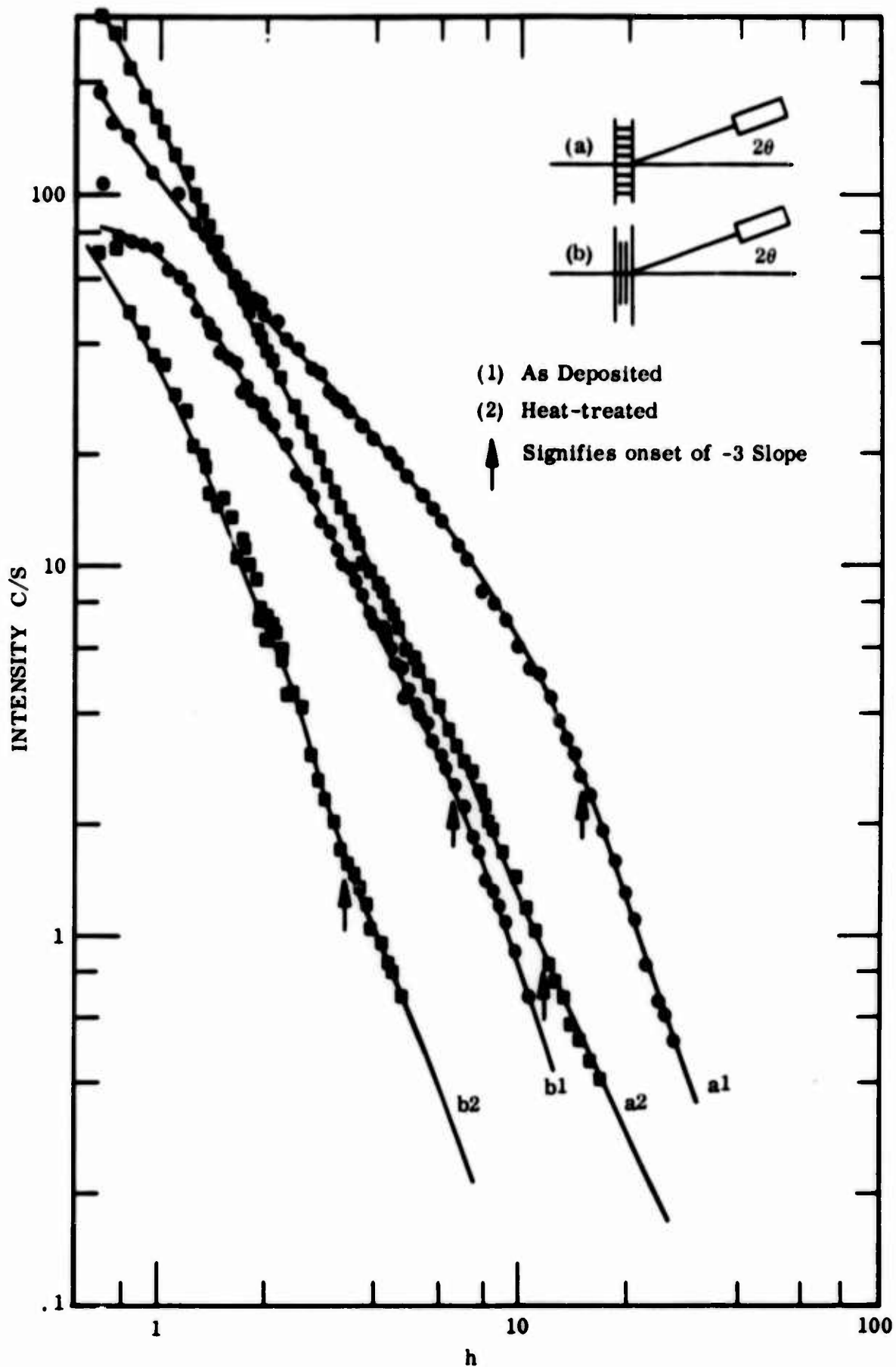


Fig. 18 Small Angle Scattering by R165 PG. Curves (a1) and (b1): As-Deposited PG; Curves (a2) and (b2): Heat-treated PG

plotted as $\log I$ vs $\log h$. Because the density of PG is nearly equal to the theoretical x-ray density, it is assumed that the scattering is caused by the presence of small voids having essentially zero electron density (95). The asymptotic h^{-3} dependency is observed for all the data, but the data for which the x-ray beam was parallel to the deposition plane do not obey the Guinier approximation. In this plot, the slope of the data should decrease at small h , and curves for specimens of the same condition but different orientation should approach the same value of I as h becomes very small. This deviation from theory for specimens with the beam oriented parallel to the deposition plane is the result of double Bragg scattering from the 0002 planes of the PG. As discussed by Bragg et al. (95), the layer planes in PG are aligned to give strong double Bragg diffraction in this specimen configuration. This distortion is so great here that it does not permit the application of the Guinier approximation, but the void thickness perpendicular to the deposition plane can be estimated from the onset of the h^{-3} dependency.

In Fig. 19, the small angle scattering data are plotted as $\log I$ vs h^2 to demonstrate the Guinier approximation. In this plot, the data for specimens of the same condition but different orientation should extrapolate to the same value of I at $h = 0$ because the scattering is caused by the same void volume in both cases. The distortion produced by the double Bragg diffraction prevents the curves noted by (a) from being properly extrapolated.

Two dimensions are required to characterize the voids observed by the small angle scattering: a void thickness perpendicular to the deposition surface,

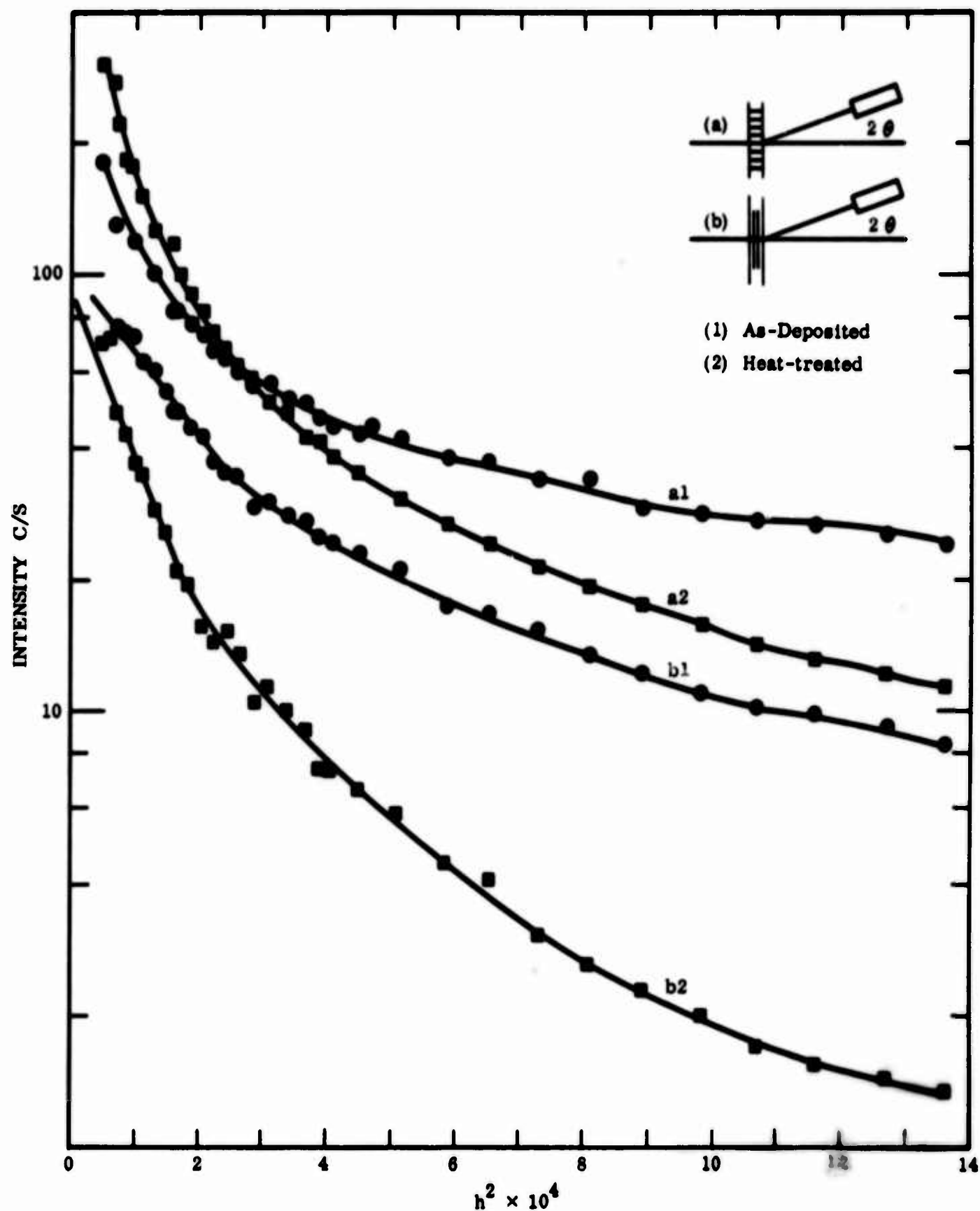


Fig. 19 Guinier Analysis of Small Angle Scattering Curves. Curves (a1) and (b1): As-Deposited PG; Curves (a2) and (b2): Heat-treated PG

b_c , and a void diameter parallel to the deposition surface, b_a . Estimates of these parameters as determined by applying the Guinier and modified Bragg approximations to the data given in Figs. 18 and 19, are listed below:

<u>Method of Estimating</u>	<u>As-Deposited</u>		<u>Heat-Treated</u>	
	b_a	b_c	b_a	b_c
Guinier	158A	—	390A	—
Modified Bragg	120	50	240	60

The agreement between the two estimates is fairly consistent, showing that during the graphitizing heat-treatment the void diameter increased by about a factor of 2 and the thickness remained essentially unchanged. This is also consistent with the increase in crystallite diameter with heat-treatment as given in Table 10. The void diameter is somewhat smaller than the crystallite size obtained from the line broadening experiments; however, it should be noted that the theories on which both these estimates are based are not accurate within a factor of 2, but they do show proper relative sizes. Similar comments apply to comparisons between the Guinier and modified Bragg approximations in the small angle scattering data.

A more detailed interpretation of small angle scattering in PG is being developed by Bragg and co-workers (129). As yet, this work has not been completed. Nevertheless, the results reported here will probably agree within a factor of 2 with the results of the more detailed analysis.

Mr. J.C. Robinson of LMSC assisted in obtaining these data.

E. Other Structural Parameters

The mercury porosimetry data showed that the volume of accessible pores in PG (in either the as-deposited or heat-treated condition) which can be penetrated with mercury at pressures up to 5000 psi is less than $0.001 \text{ cm}^3/\text{cm}^3$ of PG. This data represents the limit of sensitivity for the porosimeter for the samples used. The results were not unexpected, when one considers the high density of PG compared with its x-ray density and the lack of porosity in the microstructure. The porosimetry data were obtained by Mr. K.A. Till of LMSC.

The bulk densities of the various PG's, as determined by hydrostatic or differential weighing in isopropyl alcohol, are given in Table 12, together with the calculated x-ray densities. The density values are about 0.003 gm/cm^3 too high because the air buoyancy correction was not applied; however, the accuracy of the determination is estimated to be $\pm 0.005 \text{ gm/cm}^3$ with the major error occurring in the surface tension effects on the supporting wire. As expected, there is a small void volume in the as-deposited PG's (typically 0.4%), but the graphitizing heat-treatment virtually eliminated the porosity except in the case of the R1 material, where a slight porosity persists.

The bulk density data were obtained by Mr. R. Nygren of LMSC.

F. Summary

The PG's used in this investigation are representative of large (R277) and small (R165) cone-sized PG of the substrate nucleated type and of the small cone-sized, regeneratively nucleated type (R1). The response of each PG to heat-treatment is also typical, the major features being an increase in

Table 12
COMPARISON OF OBSERVED DENSITIES AND
DENSITIES COMPUTED FROM OBSERVED INTERLAYER SPACINGS

PG	Position in Deposit	Observed Density (gm/cm ³)	Average Observed Density (gm/cm ³)	d ₀₀₀₂ A	X-ray Density(a) (ρ _x)	Estimated Void Volume (%)
R165-AR	Top	2.212				
R165-AR	Bulk	2.208	2.214	3.425	2.220	0.3
R165-AR	Bulk	2.223				
R165-HT	Bottom	2.263				
R165-HT	Bulk	2.265	2.264	3.366	2.259	0.0
R165-HT	Bulk	2.263				
R277-AR	Top	2.219				
R277-AR	Bulk	2.219	2.212	3.417	2.225	0.6
R277-AR	Bulk	2.206				
R277-HT	Middle	2.260				
R277-HT	Bulk	2.254	2.263	3.366	2.259	0.0
R277-HT	Bulk	2.265				
R1-AR	Bulk	2.205				
R1-AR	Bulk	2.217	2.205	3.431	2.216	0.5
R1-AR	Bulk	2.193				
R1-HT	Bulk	2.251	2.250	3.375	2.253	0.1
R1-HT	Bulk	2.249				

$$(a) \rho_x = 7.603/d_{0002} \quad \text{gm/cm}^3$$

crystallite diameter and thickness of about 2.5 times and a decrease in stacking error probability from 90% to approximately 35%. This was accompanied by a decrease in mean tilt angle from somewhat more than 20 deg to about 15 deg and virtually complete elimination of void volume. Very little delamination occurred during the graphitizing heat-treatment.

Chapter VIII

EXPERIMENTAL RESULTS - DIFFUSION

A. General Behavior of Data

The structure and many of the properties of PG are anisotropic and, as expected, the diffusion of metals in PG is also anisotropic. For the same thermal treatment, the diffusion rate of Nb parallel to the deposition plane is approximately 30 times that of Nb perpendicular to the deposition plane. This factor is not the same at every temperature because the activation energies for diffusion in the two directions are not equal. The anisotropy of metal diffusion in PG gave rise to two different experimental situations.

The composition profiles fell into two general categories: those in which considerable activity remained on the surface and in the first three laps, and those in which there was very little residual surface activity. Specimens in which diffusion took place perpendicular to the deposition plane had high residual surface activities while those for diffusion parallel to the deposition plane usually did not have a high residual surface activity. Approximately the same amount of Nb was placed on each sample, so these results are consistent with the much higher D values observed parallel to the deposition plane. Two typical profiles for the two different directions are shown in Fig. 20. The difference in behavior of the two kinds of samples led to the conclusion that two

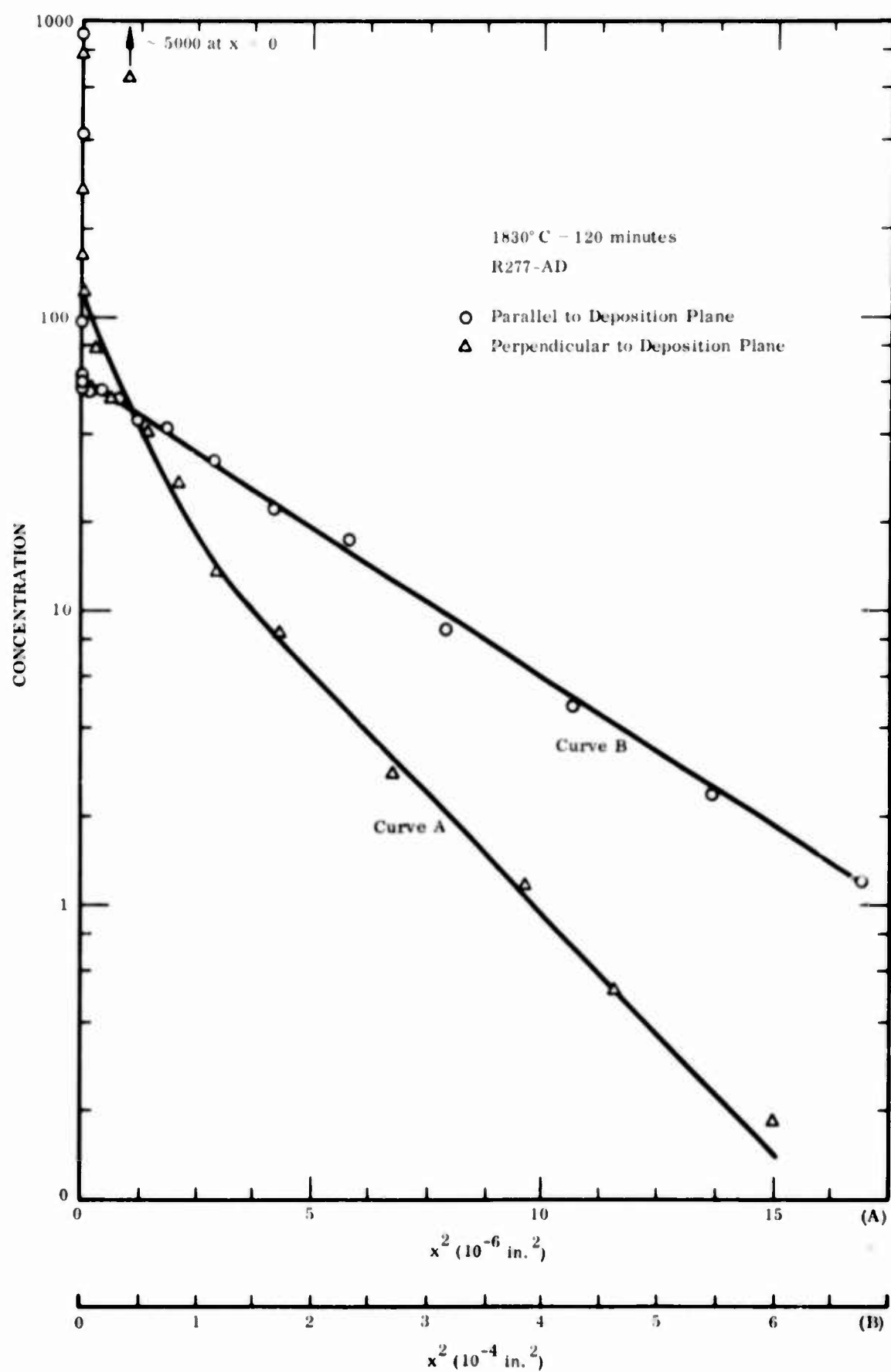


Fig. 20 Typical Composition Profiles Perpendicular and Parallel to Deposition Plane

different solutions to the diffusion equation would be required to treat the data adequately.

The concentrations observed in these experiments were very low. For the experiments approximating constant surface composition conditions, the activity concentration at the surface was about 0.1 mc/cm^3 . With a counting efficiency of approximately 25%, this observed activity corresponds to a true specific activity of $0.4 \text{ mc/cm}^3 \text{ PG}$. For Nb-95, the carrier-free specific activity without absorption, is about $4 \times 10^6 \text{ mc/gm Nb}$. From these data, the maximum concentration of Nb in PG was about $10^{-7} \text{ gm Nb/cm}^3 \text{ PG}$. As will be shown in Chapter IX, this concentration does not represent the true solubility of Nb in PG, but rather, represents a crystallite edge decoration.

B. Computation of Diffusion Coefficients

As demonstrated in Fig. 20, the data were sufficiently precise to distinguish the two separate categories. It was felt that these categories were the result of having two situations prevail during the diffusion anneals: the constant surface composition situation (CSC) and the instantaneous source situation (IS) for semi-infinite media (131, 132). In no case did the data suggest the linear log C vs x dependence predicted by various grain boundary diffusion theories. This latter observation will be discussed in more detail in the next chapter.

For the experimental conditions of a salt of a metal deposited on the specimen surface, it is not possible to predict the exact nature of the boundary conditions that apply during the diffusion anneal.

If the solubility and diffusivity are extremely low, then even the small amount of tracer deposited on the surface will not all diffuse, and a constant surface composition situation would be approximated. On the other hand, higher diffusivity can result in all the tracer diffusing into the PG and, if this occurs near the beginning of the diffusion anneal, the instantaneous source will be approximated. An intermediate situation can arise if the surface composition is neither constant nor vanishing near time zero, but is a variable function of time. If an independent estimate of the surface composition is available, then it is possible to account for this last complication (133); however, this situation did not prevail in these PG diffusion experiments. As a result, only the two extreme situations were examined.

If the CSC solution applies, then the composition relative to the surface composition (C/C_s) should behave as

$$\frac{C}{C_s} = 1 - \frac{2}{\sqrt{\pi}} \int_0^\alpha \exp(-\alpha^2 d\alpha) = \operatorname{erfc} \alpha = \operatorname{erfc} \frac{x}{2\sqrt{Dt}}$$

and if the IS solution applies, then

$$C = k \exp(-\alpha^2) = k \exp\left(\frac{x^2}{4Dt}\right)$$

will represent the C-x behavior (131, 132). These two functions are plotted in Fig. 21. For the IS equation, k was taken arbitrarily to be 2; for the CSC equation, $\log(C/2C_s)$ is plotted against α^2 using $1/2 \operatorname{erfc} \alpha$ for the dependency.

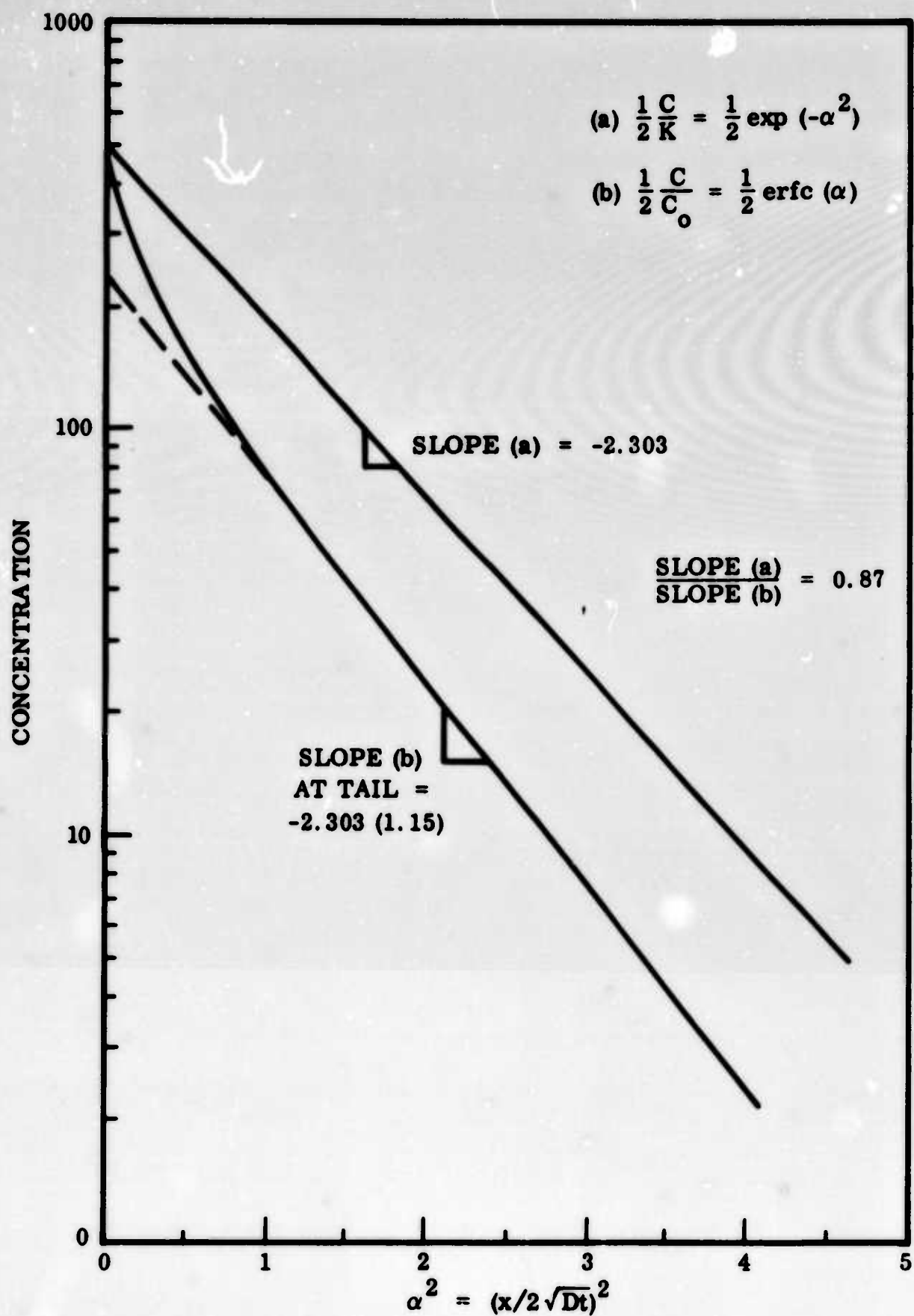


Fig. 21 Behavior of Instantaneous Source (a) and Constant Surface Composition (b) Solutions to Fick's Diffusion Laws for Semi-infinite Solid

As expected, the IS solution is linear over the entire range, but the CSC solution is approximately linear only beyond $C/2C_s \cong 0.08$ and the slope of the line increases with smaller α . Clearly, if one assumed that an IS solution applied in an experiment in which the CSC solution were more appropriate, and, if the diffusivity were computed from the slope of the curve, some serious error could result for $\alpha < 1.0$. Malkovich (134) has treated this problem analytically. He derives the following expression, relating the D measured by assuming an IS solution (D_{meas}), with the true D appropriate to the CSC solution (D_{actual}):

$$D_{\text{meas}} = [\sqrt{\pi} \alpha \exp(\alpha^2) \operatorname{erfc} \alpha] D_{\text{actual}}$$

$$D_{\text{meas}} = \lambda D_{\text{actual}}$$

$$\alpha = \frac{x}{2\sqrt{Dt}}$$

He also computed the λ factor:

α	λ
0.10	0.16
0.25	0.34
0.50	0.55
1.00	0.76
2.00	0.91

Actually, the curve of $\log C/2C_s$ vs. α^2 or x^2 for the CSC solution is everywhere concave upward; empirically, one can choose a slope starting at $\alpha = 1.0$ that gives D_{meas} to be 0.87 D_{actual} , as depicted in Fig. 21.

Figure 21 definitely shows that experimental conditions approximating the CSC solution can be distinguished from the IS solution by plotting the data as $\log C$ vs x^2 , and the data should be treated accordingly. In this study, all the data were first plotted as $\log C$ vs x^2 . Those curves which were linear for $C/C_s < 0.9$ were treated as approximating the IS conditions while those which curved upward for $C/C_s > 0.1$ were treated as approximating the CSC conditions. For the CSC samples, the first three or four laps showed very high activity relative to the estimated value of C_s ; this additional activity was attributed to radioactive material remaining on the surface and the lack of perfect interface resolution.

For the samples to be treated as approximating the IS conditions, the diffusivities were computed from the average of the maximum and minimum values obtained from lines drawn with maximum and minimum slopes through the data plotted as $\log C$ vs x^2 . A standard deviation for each diffusivity was estimated by dividing the difference between the maximum and minimum values by $\sqrt{2}$. These estimated standard deviations were between 10 and 20% of the value measured and occasionally were as high as 30%.

To obtain a first estimate of C_s , the data approximating the CSC conditions were extrapolated back to $x^2 = 0$ on the $\log C$ vs x^2 plots. Each composition point was then divided by $2C_s$ and the result plotted vs x^1 on the lower half of linear probability paper (Keuffel and Esser Co., #359-23) the scale of which is designed to make $1/2 \operatorname{erfc} \alpha$ linear from 0.50 to 0.0001. If the data did not extrapolate back to $C/2C_s = 0.50$, then new values of C_s were selected and

each point again adjusted until a straight line through the data would intersect the probability scale at 0.50 relative composition. It should be noted here that as long as the C_s value is incorrect, the data will not lie on a straight line but will be slightly curved in the direction of the error. After a suitable value of C_s was determined, lines of maximum and minimum slope were drawn to compute maximum and minimum values of D. The diffusivities were computed from the equation

$$\frac{C}{2C_s} = \frac{1}{2} \operatorname{erfc} \frac{x}{2\sqrt{Dt}}$$

using a single value of $C/2C_s$, usually 0.00150. Average diffusivities and standard deviations were estimated as above.

C. Measured Diffusion Coefficients

Table 13 lists the diffusivities, as determined above, together with the PG type, time and temperature of anneal, and groups the data according to diffusion anneal. Where the word fail is written, the data were not used to calculate a D because, upon lapping and cleaning the specimen with mylar tape, the surfaces became extremely uneven and produced very erratic profiles. This damage to the samples was prevented later by cleaning the heat-treated specimens with cellophane tape which is less adherent and will not tear the heat-treated PG. The symbol (d) in the table signifies that the data are probably influenced by diffusion parallel to the deposition plane. The symbol \gg denotes far greater penetration than expected, indicating that

Table 13
DIFFUSION COEFFICIENTS (D) FOR Nb-95 IN VARIOUS TYPES OF PG
(D in cm^2/sec)

Sample Designation ^(a)	TEMPERATURE ($^{\circ}\text{C}$)/TIME								1935 (0 hr)
	1450 (163 hr)	1465 (9 hr)	1530 (40 hr)	1560 (3 hr)	1650 (16 hr)	1650 (3.5 hr)	1750 (4 hr)	1850 (2 hr)	
R165-AD< a >	1.68×10^{-10}	2.80×10^{-10}	3.42×10^{-10}	1.10×10^{-9}	3.55×10^{-9}	1.81×10^{-8}	1.29×10^{-8}	3.74×10^{-8}	6.45×10^{-10} 6.45×10^{-10}
R165-AD< c >			1.16×10^{-11}		3.93×10^{-11}	2.07×10^{-8}	1.61×10^{-10}	3.87×10^{-10}	
R165-HT< a >	7.10×10^{-10}	2.38×10^{-9}	2.65×10^{-9}	fall(b)	2.07×10^{-11}	1.22×10^{-7}		2.07×10^{-7}	1.74×10^{-9} $< a > (e)$
R165-HT< c >								2.02×10^{-10}	
R277-AD< a >	1.87×10^{-10}	5.35×10^{-10}	5.74×10^{-10}	1.35×10^{-9}	1.03×10^{-10} $9.03 \times 10^{-11} (c)$	2.36×10^{-8}	1.62×10^{-8}	3.87×10^{-8}	1.61×10^{-20} 1.61×10^{-10}
R277-AD< c >			2.58×10^{-11}		7.10×10^{-11}	1.03×10^{-8}	1.62×10^{-10}	4.52×10^{-10}	
R277-HT< a >	1.16×10^{-9}	2.45×10^{-9}	2.52×10^{-9}	fall	2.90×10^{-11}	9.04×10^{-8}		1.81×10^{-10}	$< a >$
R277-HT< c >									
R1-AD< a >	1.29×10^{-10}	1.81×10^{-10}	3.68×10^{-10}	9.03×10^{-9}	2.26×10^{-9}	2.07×10^{-8}		3.29×10^{-8}	1.23×10^{-9} 4.77×10^{-10}
R1-AD< c >			1.87×10^{-11}		5.80×10^{-11}			5.35×10^{-10}	
R1-HT< a >	6.38×10^{-10}	1.10×10^{-9}	1.16×10^{-9}	fall	4.32×10^{-8}				2258 4.429
R1-HT< c >					2.71×10^{-11}				
Temp. ($^{\circ}\text{K}$)	1763	1753	1803	1833	1923	2023	2123	2208	
$10^4/T \cdot \text{K}$	5.872	5.668	5.546	5.456	5.200	4.943	4.710	4.529	

(a) PG type-condition-direction: AD = as-deposited, HT = heat treated
 < a > = parallel to deposition surface, < c > = perpendicular to deposition surface

(b) Fall = sample ruined

(c) Old Nb solution used

(d) Data possibly influenced by < a > diffusion

(e) < a > diffusion dominated

diffusion parallel to the deposition plane definitely dominated the diffusion process.

Finally, the letter (c) denotes a D value obtained with a Nb solution 112 days (3.1 half-lives) older than the solution used on the other samples of that annela. Nb-95 decays to Mo-95 and this comparison was intended to observe any effect the Mo might have. As may be seen, the Mo did not have any discernable effect.

Most of the data were reduced by the author's wife, Betty.

D. Temperature Dependence of Diffusion Coefficients

Figures 22 and 23 are Arrhenius plots of the diffusion coefficients grouped according to the two directions studied. The data for each PG, in each condition and direction, were fitted to the equation

$$D = D_0 \exp(-Q/RT)$$

using a least squares technique developed by Deming (135) which permits one to include the estimated errors of each data point independently. The data were fitted with the logarithm form of the Arrhenius equation (the standard deviations for D_0 computed in this form are factors rather than additive terms). The result of these computations is given in Table 14. Because the activation energies for a given direction were all within their overall standard deviations, they were averaged to produce one activation energy for diffusion parallel to the deposition planes, Q_a , and another perpendicular to the deposition planes, Q_c . The D_0 's were then recomputed using the average activation energies in each direction. The results of these calculations are also given in Table 14.

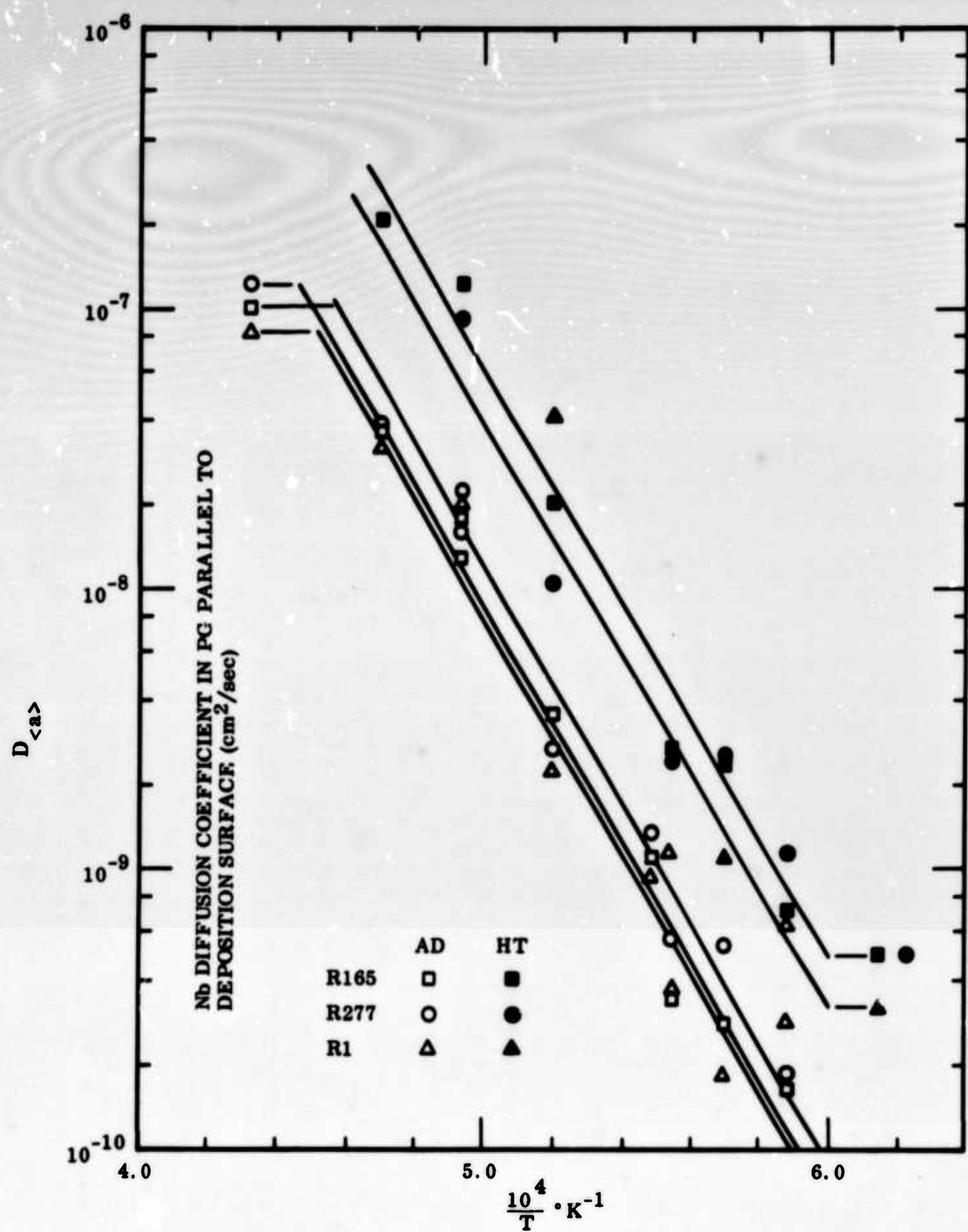


Fig. 22 Arrhenius Plots of Nb Diffusion Coefficient in PG. Diffusion Parallel to Deposition Plane

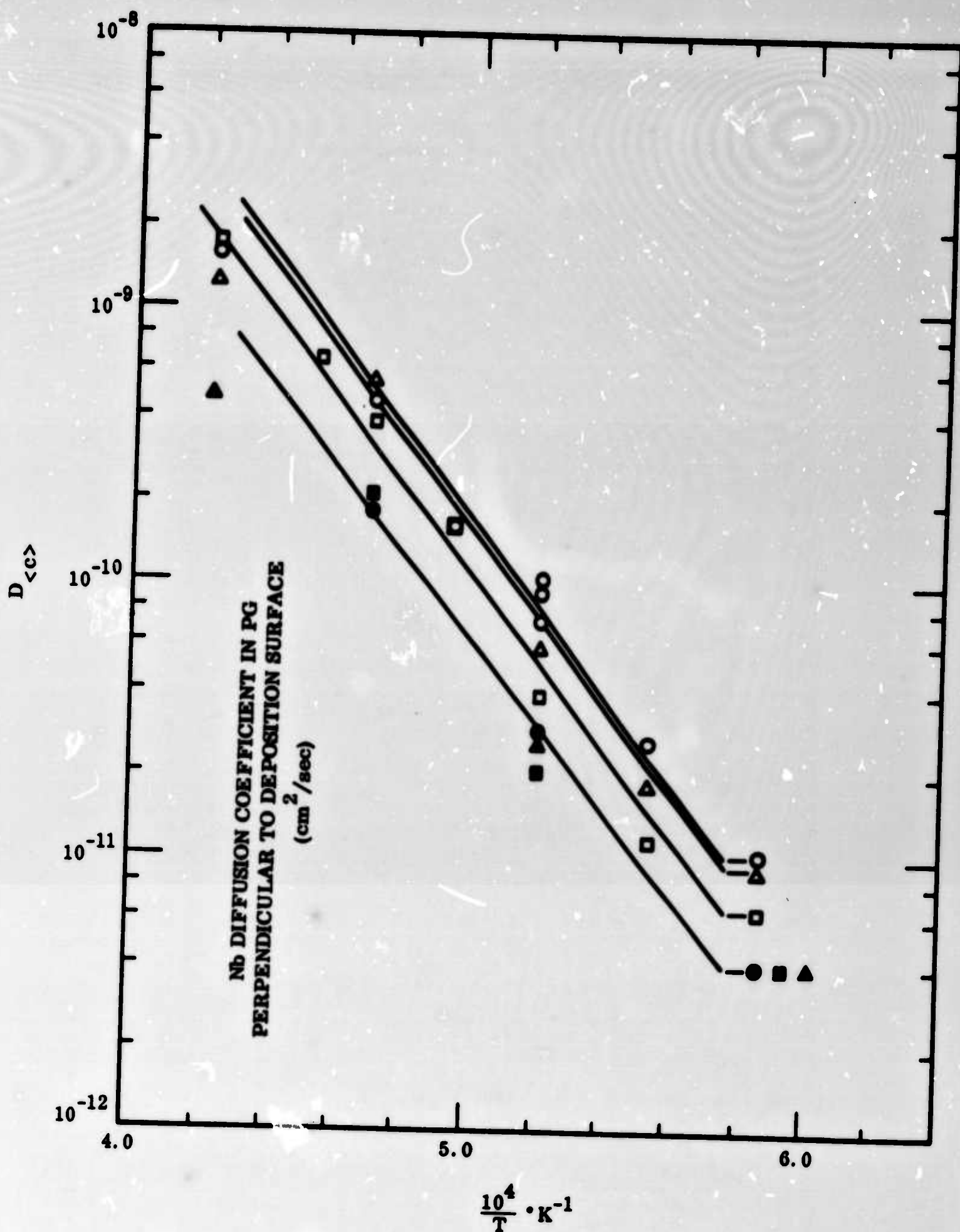


Fig. 23 Arrhenius Plots of Nb Diffusion Coefficient in PG. Diffusion Perpendicular to Deposition Plane

Table 14
 TEMPERATURE DEPENDENCE OF DIFFUSION COEFFICIENTS
 Data Expressed as $D = D_0 \exp(-Q/RT)$

PG Type and Condition	Direction of Diffusion	First Estimate (cm ² /sec)	$f_o^{(a)}$ Std. Dev. Factor	Q Activation Energy (k cal/mole)	σ_Q Std. Dev. of Q (k cal/mole)	\bar{Q} Avg. Activation Energy (k cal/mole)	σ_Q Std. Dev. of \bar{Q}	Second Estimate of D_o (cm ² /sec)	$\frac{D_o(\text{HT})}{D_o(\text{AD})}$
R165-AD	< a >	6.54×10^2	3.9	98.3	5.3			3.23×10^2	5.6
R277-AD	< a >	2.77×10^2	3.1	94.3	6.2			3.81×10^2	4.8
R1-AD	< a >	2.45×10^2	2.1	95.6	3.1			2.71×10^2	5.0
R165-HT	< a >	2.07×10^3	1.8	96.1	2.2	$\bar{Q}_{<a>} = 96.2$	4.0	1.81×10^3	
R277-HT	< a >	1.94×10^3	2.8	96.5	4.0			1.81×10^3	
R1-HT	< a >	(2.8×10^5)	(500)	(113)	(26.0)			1.35×10^3	
R165-AD	< c >	8.38×10^{-2}	1.5	78.7	1.8			1.16×10^{-2}	.56
R277-AD	< c >	6.32×10^{-1}	3.1	69.3	4.5			1.94×10^{-2}	.33
R1-AD	< c >	4.71×10^{-2}	5.3	67.8	4.9			1.74×10^{-2}	.38
R165-HT	< c >					$\bar{Q}_{<c>} = 73.1$	4.0		
R277-HT	< c >								
R1-HT	< c >							6.45×10^{-3}	

(a) Standard deviation of D_o , $\sigma_{D_o} = f_o D_o$

Using the propagation of error analysis (120) it can be shown (121) that

$$\frac{\sigma_Q^2}{Q^2} = \left(\frac{RT}{Q}\right)^2 \frac{\sigma_D^2}{D^2} + \frac{\sigma_T^2}{T^2}$$

$$\frac{\sigma_{D_0}^2}{D_0^2} = \frac{\sigma_D^2}{D^2} + \left(\frac{Q}{RT}\right)^2 \frac{\sigma_T^2}{T^2}$$

where σ_A is the standard deviation of any quantity A, T the temperature in ^0K , Q the activation energy, R the gas constant, and D_0 the pre-exponential factor in the Arrhenius equation. As determined by this study and that of WMB (17), the diffusion coefficients of metals in PG exhibit very high activation energies and Q/R is typically $50 \times 10^3 ^0\text{K}$. With the temperature range in the vicinity of 2000^0K , the factor Q/RT is about 25. Reference to the above equations shows that this high value of Q/RT makes the determination of Q rather insensitive to errors in D while the pre-exponential factor D_0 is extremely sensitive to errors in T. For example, if $\sigma_D/D = 20\%$ and $\sigma_T/\% = 1.5\%$, then

$$\frac{\sigma_{D_0}^2}{D_0^2} = (.20)^2 + (25)^2 (.015)^2$$

and

$$\frac{\sigma_{D_0}}{D_0} = 0.42$$

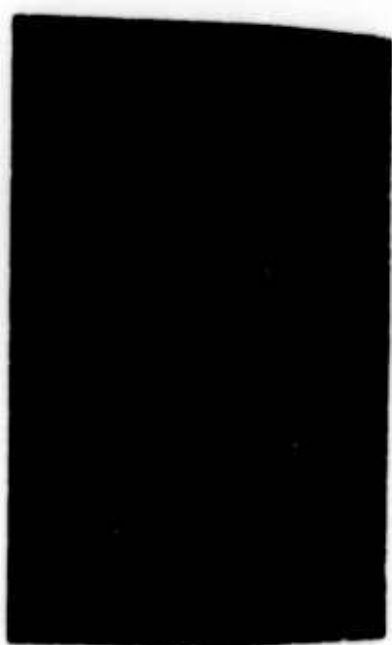
The values of σ_D/D and σ_T/T given above are typical of the conditions used in these experiments; however, the resulting values of σ_{D_0}/D_0 from the least squares computation are much larger than the value estimated above. Table 14 indicates that the D_0 's for a particular direction and condition do not differ appreciably for all the different types of PG. The small variation of D_0 with microstructure is taken to indicate that the additional scatter in D_0 is not due to structural variations within a particular PG type. Instead, the additional scatter is probably due to errors in the temperature determination. Besides the sources of temperature error listed in Chapter VIII, which totaled less than 1.5%, additional errors could arise due to unknown temperature gradients over the stack of specimens and within the holder. Another source of error is the possibility of temperature differences between the black body hole in the graphite holder and the specimens. The size of these potential errors is not known, but they would not have to be very large to appreciably increase the overall scatter in the data.

E. Autoradiography

Some representative autoradiographs are shown in Figs. 24, 25, and 26, together with photomicrographs of the same specimens. These autoradiographs were taken at various depths in the concentration profile and their position in the profile was not a factor in their appearance. Figures 24 and 25 contain autoradiographs taken parallel to the deposition plane and show how the Nb is concentrated around the circles which represent the major cone boundaries in

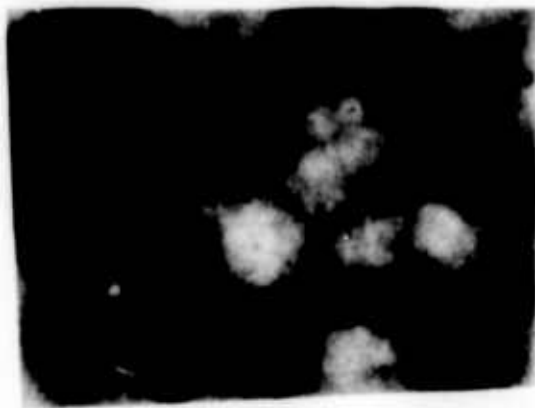


R165



R1

Fig. 24 Direct Comparison of Structure and Autoradiographs Parallel to Deposition Surface for R165 and R1 As-deposited PG



As-deposited

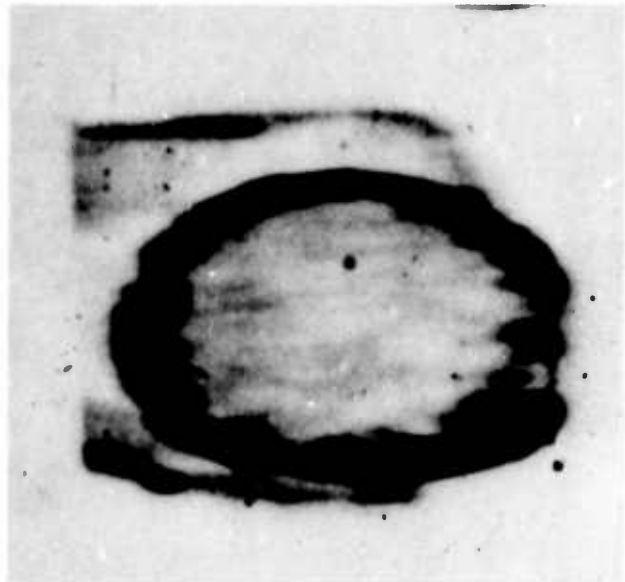


Heat-treated

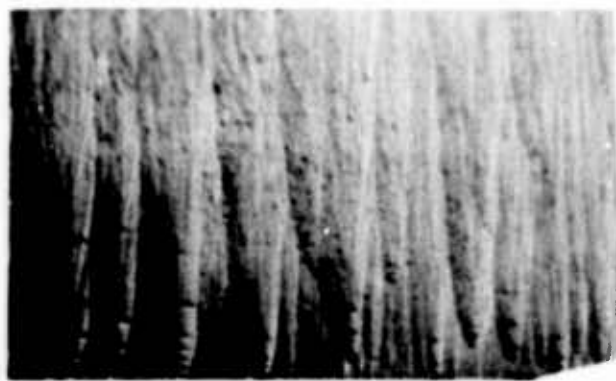
Fig. 25 Direct Comparison of Structure and Autoradiographs Parallel to Deposition Surface for R277 PG, As-deposited and Heat-treated

the PG. The R1 autoradiograph (Fig. 24) was heavily exposed to determine if the centers of the larger circles contained any appreciable radioactivity. As is evident, the larger circles are virtually devoid of any radioactivity and the areas containing many smaller cones show nearly complete film darkening. Similar effects are present in the other views of the deposition planes of the R165 and R277 PG. WMB (17) obtained essentially the same autoradiographs. They further observed that autoradiographs taken from samples in which diffusion occurred near the substrate surface of the deposit showed smaller circles than did samples for diffusion near the final deposition surface. The major diameter of the circles increases from the bottom to the top, as was clearly delineated in the WMB autoradiographs. All of these autoradiographs are proof that metal diffusion in PG perpendicular to the deposition plane occurs down primary cone boundaries, with entry into the cones taking place principally from these primary cone boundaries.

In Fig. 25, it is evident that the heat-treatment had very little effect on the manner in which the Nb-95 is distributed. This is to be expected because the heat-treatment did not appreciably alter the primary structure. The increased detail in the R277-HT autoradiograph is the result of repolishing the sample after lapping to be certain that the observed distribution of Nb-95 was not an artifact. Autoradiographs and microstructures of R277 as-deposited and heat-treated specimens viewed on the plane perpendicular to the deposition plane are shown in Fig. 26. The major features to be noted here are the lack



As-deposited



Heat-treated

Fig. 26 Comparison of Structure and Autoradiography Perpendicular to Deposition Surface for R277 PG, As-deposited and Heat-treated

cone delineation and the presence of streaks parallel to the deposition plane. These streaks are due to occasional delaminations or are reflections of the PG's tendency to delaminate. They demonstrate the diffusing Nb will decorate places of delamination or incipient delamination. Both of these features will be discussed in more detail in Chapter IX.

Chapter IX

DISCUSSION

A. Summary of Results

The diffusion coefficients of Nb in several different types of PG have been determined both parallel and perpendicular to the deposition plane, and the structure of each PG has been characterized by the application of several techniques of metallography, x-ray diffraction, and density determinations. The structure and diffusion data, reported in detail in Chapters VII and VIII, are summarized in Table 15. These data will be reviewed briefly and then a model for the diffusion of metals in PG will be developed. Following these discussions, the model will be applied to other forms of graphite and diffusion alloying PG will be discussed briefly.

The as-deposited PG's represented a wide variety of microstructures. Their structures determined by x-ray techniques, however, were quite similar. The following structure parameters were derived from the x-ray diffraction studies:

- Stacking error probability and x-ray density
- Crystallite thickness and diameter
- Degree of preferred orientation and mean tilt angle
- Void thickness and diameter.

The major differences in the x-ray structure occurred in the degree of preferred orientation. Some of the specimens were given a graphitizing heat-treatment which increased their density and crystallite size, sharpened their texture, decreased their stacking error probability, and altered their void structure. The specific values relative to these changes are summarized in Table 15.

As noted in Chapter VIII, all the diffusion coefficients in a particular direction, regardless of PG type, could be represented by a single activation energy and a variable pre-exponential factor. The scatter of the data were about a factor of 2.5 and somewhat less for the R165 material. The graphitizing heat-treatment increased D_{o-a} , decreased D_{o-c} , did not particularly alter the spread in the data, and did not seem to affect the activation energy for diffusion in either direction.

Autoradiographs taken perpendicular to the mass flux for diffusion perpendicular to the deposition plane (D_{o-a}) demonstrated that diffusion perpendicular to the deposition plane occurs in the primary or major cone boundaries. Autoradiographs taken perpendicular to the deposition plane for diffusion parallel to the deposition plane showed a uniform distribution of radioactivity. In this configuration, the cone structure was not delineated by the diffusing Nb but some streaks occurred parallel to the deposition plane in the autoradiographs.

B. Correlation with Structure

The rather small variation of diffusion coefficients for a wide range of microstructures indicates that the structure of the PG, as determined by optical

Table 15
SUMMARY OF STRUCTURE AND DIFFUSION DATA

PG Number and Condition	Micro-structure	Density (gm/cm ³)	Stacking Error Probability (p)	Crystal Diameter L _a (Å)	Crystal Thickness L _c (Å)	Mean Tilt Angle 2 _{1/2} <α>	Void Diameter b _a (Å)	Void Thickness b _c (Å)	D _{o<c>} // c (cm ² /sec)(k cal/mole)(k cal/mole)	D _{o<a>} ⊥ c (cm ² /sec)(k cal/mole)(k cal/mole)	Q< _a > ⊥ c (k cal/mole)
R165-AD	C3	2.214	.90	250	170	23.2°	150	50	1.16×10 ⁻²	3.23×10 ⁻²	73.1
R165-HT	C3	2.264	.30	600	480	15.5°	300	60	6.45×10 ⁻³	1.81×10 ⁻³	73.1
R277-AD	A2	2.212	.90	250	170	19.4°	—	—	1.94×10 ⁻²	3.81×10 ⁻²	73.1
R277-HT	A2	2.263	.30	600	330	16.0°	—	—	6.45×10 ⁻³	1.81×10 ⁻³	73.1
R1-AD	F1	2.205	.90	190	170	27.5°	—	—	1.74×10 ⁻²	2.71×10 ⁻²	73.1
R1-HT	F1	2.250	.50	460	210	20.6°	—	—	6.45×10 ⁻³	1.35×10 ⁻³	73.1

microscopy, has little effect on the diffusivity of metal atoms in PG. However, the autoradiographs demonstrated that the PG microstructure determines the distribution of the diffusing species and the number of equivalent diffusion paths per unit area. Thus, the total mass flow of metals diffusing in PG will be controlled by the microstructure, but the diffusivity, defined from Fick's First Law as the total mass flow per unit concentration gradient and unit sample area, will not be affected by the microstructure.

This diffusivity does not depend upon the microstructure because both the total mass flow and the concentration per unit sample volume are proportional to the number of equivalent paths per unit sample area. The statement can be made because, as will be shown in this chapter, true volume of metals in PG is inconsequential, and the diffusing atoms are restricted to the crystallite surfaces. Thus, the situation is approximately equivalent to studying metal diffusion in a metal mesh; the measured diffusion coefficient does not depend upon the mesh size.

The somewhat lower scatter in the diffusion data for the R165 material is explained by its more uniform microstructure because the uniformity of the substructure is probably related to the uniformity of the microstructure. As described in Chapter VIII, some of the scatter in the diffusion data is definitely the result of the very high activation energies; even a 1% error in temperature can appreciably affect the errors in the pre-exponential factor in the Arrhenius equation. Other contributions to the scatter could arise from the presence of

delaminations, slight misorientations of the samples relative to the deposition plane, and structural variations among the samples of a particular PG.

Graphitization did not appear to change the general modes of diffusion because neither the autoradiographs nor the activation energies for a particular direction were altered appreciably. Since the activation energies were not affected by graphitization, changes in the pre-exponential factor, D_0 , must be responsible for the changes in the diffusion coefficients with graphitization. The graphitizing heat-treatment increased the crystallite diameter by about a factor of 2.4 and increased D_{0-a} about 5.2 times. Because D_0 is proportional to the distance squared (136), and because the square of the increase in the crystallite diameter is 5.8, the jump distance parallel to the deposition plane must be related to the crystallite diameter. This unusual correlation will be discussed later in more detail. In contrast to this behavior, D_{0-c} decreased with graphitization even though the crystallite thickness increased about two-fold.

The observed 5 to 10 deg decrease in mean tilt angle with heat-treatment would not appreciably alter the nature or length of the diffusion paths by itself. This change, however, accompanies the many other changes in structure brought about by graphitization, and the diffusion path is thus indirectly related to the texture. For example, a sharpening of the texture would decrease the width of the crystallite boundaries by decreasing the angular misorientation across them.

C. Possible Mechanisms for Metal Diffusion in PG

Possible diffusion mechanisms for metals in PG can be separated into two categories — mechanisms within the crystallites and mechanisms external to the crystallites.

Within the crystallites the following mechanisms are possible:

- 1) Direct substitution at a carbon site and subsequent diffusion by any of the carbon self-diffusion mechanisms:
 - a) Layer plane vacancy-atom exchange
 - b) Direct interchange of the atom with a carbon atom
 - c) Interlayer migration
 - d) Vacancy-atom exchange between layers
- 2) If the atoms are too big or are otherwise not chemically suited to substitute for a carbon atom, then diffusion could occur by the following:
 - a) Vacancy cluster — foreign atom exchange within a layer
 - b) Vacancy cluster — foreign atom exchange between layers
 - c) Interlayer migration
 - d) Migration along gross stacking errors, such as a missing portion of a layer plane

Mechanisms external to the crystallites include:

- 1) Migration between crystallites along the top layer plane, with trapping at vacancy clusters and at the edge of the top layer plane.

- 2) Migration perpendicular to the layers along the crystallite sides, proceeding layer by layer.
- 3) Migration perpendicular to the layers along the crystallite sides, with a jump distance comparable to the crystallite thickness.
- 4) Migration in regions of gross mismatch where crystallites of differing orientations meet.
- 5) Migration around the crystallites, proceeding from trap to trap along the circumference of the crystallites.

The mechanisms listed above are essentially the only ones possible for metal diffusion in PG. Gross pore diffusion is not a possibility because the high density of PG rules out the presence of the large, interconnected pores that occur in normal synthetic graphites. As will be discussed shortly, the small pores indicated by the small angle scattering studies in PG are included in item 1 of the mechanisms external to the crystallites.

In the following paragraphs, each of the above mechanisms will be examined to see which of them are probable mechanisms for metal diffusion in PG.

Considering the mechanisms within the crystallites, the first set requires that the metal atom substitute for carbon in the graphite lattice. To substitute for carbon, the metal atom must have the proper valence to participate in the graphite structure and must be small enough not to seriously distort the lattice. The only elements small enough not to disturb the graphite lattice are B, H, O, and N. All of these combine readily with carbon to form compounds but none

have the valence necessary to participate in the graphite bonding structure.

Of these elements, B and N react with each other to form BN which has structures very similar to the graphite and diamond structures (9).

The group IVA elements have the proper valence to substitute for carbon, but even the Si atom is 50% larger than the carbon atom, which is a serious size difference in covalently-bonded structures. The chemical similarity of Si and C is well documented, and α -SiC exists in a variety of hexagonal layer structures (54). There is, however, no evidence for direct substitution of Si in the graphite lattice and the large size difference would probably prevent direct substitution from occurring. From the above discussion, it can be seen that the mechanisms of metal diffusion requiring direct substitution for the carbon atom are not very likely and the other mechanisms must be considered.

Of the second set of mechanisms for diffusion within the crystallites, those mechanisms based on the motion of vacancy clusters are not very likely, considering the high energy that would be required to form and move such defects in the covalently-bonded planes (see Chapter II). The interlayer mechanisms are also unlikely except for the very smallest atoms and in situations in which lamellar compounds form. If lamellar compounds are formed, their presence would be noted by the swelling at high temperature and the increase in the interlayer spacing that accompanies their formation. As noted in Chapter II, the formation energy of an interlayer Xe atom (4.4 Å diameter) is estimated to be 350 kcal/mole and, although the transition metals are somewhat smaller than the Xe atom, electronic interactions and the fact that the "free space" between

layers decreases with increasing temperature (137) would prevent appreciable interlayer diffusion. Gross stacking errors large enough to permit diffusion of metal atoms in PG would greatly disturb the layer plane periodicity and this disturbance would be reflected in the crystallite size. Thus, mechanisms 2d under diffusion within the crystallites is equivalent to mechanisms 1 under diffusion external to the crystallites. From this discussion, it can be seen that diffusion in PG must occur external to the crystallites for all but the smallest atoms.

Metal diffusion in PG is anisotropic. This discussion will now be separated into mechanisms for diffusion parallel to the deposition plane and mechanisms perpendicular to the deposition plane.

Of the mechanisms postulated for diffusion external to the crystallites, only 1, 4, and 5 apply to diffusion parallel to the deposition plane. Mechanism 1, migration between crystallites along their top and bottom planes, requires a consideration of metal atom sizes just as in the case of the interlayer mechanism discussed directly above. Metal atoms are typically 3 Å in diameter, the "free space" between carbon atoms within a crystallite being about 1.5 Å at 2000°C (137). Therefore, migration between crystallites along their top and bottom planes requires that the crystallites be separated sufficiently to provide room for the diffusing atoms. The voids indicated by the small angle scattering studies will provide just this separation. The void diameters are slightly less than the crystallite diameters, and the thicknesses are approximately 50 Å.

The thickness values are biased to the larger values (95), but smaller void thicknesses are adequate to allow for metal migration between the crystallites.

In mechanisms 1 (external to the crystallites), trapping of the diffusing atoms will occur at the unsatisfied bonds along the edges of the top and bottom layers of the crystallites and at vacancy clusters in the top and bottom planes.

Because there was no evidence of preferential boundary penetration for diffusion parallel to the deposition plane, mechanism 4 (external to the crystallites) does not apply. Mechanism 5, migration around the circumference of the crystallites, although applicable to diffusion parallel to the deposition plane, is unimportant. The jump distance for mechanism 5 is a few Å while that for mechanism 1 is a few hundred Å. Therefore, the diffusion rate based on mechanism 5 would be inconsequential compared to that for mechanism 1.

The mechanisms external to the crystallite labelled 2, 3, and 4 apply to metal diffusion perpendicular to the deposition plane. Migration rates perpendicular to the layers will depend upon how well the crystallites meet along their common boundaries and upon the nature and extent of contamination by other foreign atoms at the layer plane edges. Furthermore, the unsatisfied bonds at each layer plane edge will provide many trapping sites, and the average jump distance will be of the order of the layer plane separation distance. This situation eliminates mechanism 3, in which the jump distance is comparable to the crystallite thickness.

In PG there are regions of differing misorientation; within a minor cone the misorientation between crystallites is rather small, while at minor cone

boundaries it is somewhat greater, and at major cone boundaries it is the greatest of all. Because the major cone boundaries contain the greatest degree of mismatch, they will offer the least resistance of all the boundaries to the diffusion of metals. The unsatisfied bonds at each layer and the regions of differing misorientation are evidence for a diffusion mechanisms perpendicular to the deposition plane that includes mechanisms 2 and 4.

To summarize:

- Metal diffusion in PG can only occur external to the crystallites
- Traps exist along the layer plane edges and at vacancy clusters in the top and bottom layer planes of the crystallites
- Atoms diffusing on the top layer planes of the crystallites are relatively free to move, provided there is sufficient room between between the crystallites
- Primary cone boundaries contain regions of greater misorientation than do secondary cone boundaries
- Diffusion perpendicular to the layer planes occurs principally in the primary cone boundaries, the regions of greatest layer plane misorientation
- Atoms diffusing perpendicular to the layer planes encounter frequent trapping sites, probably at each layer plane edge

D. Model for the Diffusion of Metals in PG

Two separate processes for metal diffusion in PG are recognized; one parallel to the layer planes and another perpendicular. The high degree of preferred orientation of the layer planes in PG makes it possible to assume a close proportionality between the diffusion coefficient measured parallel to the deposition plane ($D_{\langle a \rangle}$) and the diffusion coefficient parallel to the layer planes. The nearly straight cone boundaries and an analysis given in the Appendix make it possible to relate the diffusion coefficient measured perpendicular to the deposition plane ($D_{\langle c \rangle}$) with the diffusion coefficient perpendicular to the layer planes.

The expression relating the diffusion coefficient for non-substitutional diffusion to the jump distance (d) and jump frequency (ν) will be given here because it will be needed later in the development of the model for metal diffusion in PG (136). This expression is

$$D = k d^2 \nu$$

where k is a numerical factor concerning the number of different jumps possible (136). The jump frequency is simply given by the vibration frequency, ν_0 , and the Boltzman factor, therefore

$$D = k d^2 \nu_0 \exp(-\Delta G^*/RT)$$

where ΔG^* is the standard Gibbs free energy of activation per mole required to surmount the energy barrier for the jump process.

Metal diffusion in PG parallel to the layer planes takes place between the crystallites and along delaminations in the material, as is evidenced by autoradiography and by deductions concerning the lack of diffusion within the crystallites. Because the top and bottom surfaces of the crystallites are relatively free of traps and the edges of the crystallites have the highest trap density, the important jump distance parallel to the layer planes is the crystallite diameter. One can determine that the jump distance is equal to the crystallite diameter by considering that the ratios of the D_{o-a} 's for the as-deposited and partially graphitized PG's are approximately equal to the ratio of the squares of the crystallite diameters in the two conditions. The basis of this correlation is given in the above equations relating the diffusivity to the square of the jump distance. Vacancy-cluster trapping can also occur, but it will not be important. The energy to form even a divacancy is estimated to be 150 kcal/mole (see Chapter II), and, unless an active source of vacancies exists the few available clusters will soon saturate. After saturation, vacancies or vacancy-clusters will not appreciably affect the overall migration rate. As noted above, metal diffusion across the surfaces of the crystallites requires a slight void region between the crystallites to allow passage of the diffusing atoms; the small angle scattering from PG is the evidence for these voids.

The microstructure of the PG is not delineated by diffusion parallel to the layer planes because there are about as many trapping sites per unit area near the major cone boundaries as there are away from them. Diffusion parallel to the deposition plane in the major cone boundaries should occur at about the same

rate as cone boundary diffusion perpendicular to the deposition plane. The data showed that the diffusion rate measured parallel to the deposition surface is greater than that measured perpendicular to it at any temperature; therefore, diffusion parallel to the deposition surface is dominated by diffusion across the crystallite surfaces and not by cone boundary diffusion.

Diffusion parallel to the deposition plane occurs on approximately flat planes containing the crystallite surfaces; the relatively slower diffusion rate perpendicular to the deposition plane prevents interaction between the parallel planes of diffusion. If this interaction were appreciable, it would complicate the measurement of $D_{\langle a \rangle}$. Diffusion parallel to the deposition plane is slightly complicated by diffusion around the circumference of the crystallites but, as described earlier, mass transport by this circumferential path is negligible compared to diffusion across the crystallite surfaces. The delaminations mentioned above can slightly disturb the concentration profile, but there is little difference between surface diffusion along a delamination and surface diffusion across a crystallite if traps exist along the delamination with about the same spacing as the crystallite diameter. The extent to which the traps in the delaminations do not approximate the traps within the material will determine the effect of the delaminations on measuring the diffusion coefficient parallel to the layer planes.

In apparent contradiction of the results and model presented above, Wolfe, McKenzie and Borg observed that extreme graphitization in PG (annealed at 3000°C for 15 min) decreased the diffusion coefficient of Ni-63 parallel to the

layer planes by about three orders of magnitude. PG this well graphitized would be characterized by a very large crystallite size, an extremely sharp layer plane texture (5), and, probably, a complete lack of small angle scattering. The lack of misorientation between the crystallites would permit considerable inter-crystallite bonding over adjacent layer plane faces, and this bonding would tend to eliminate the voids between the crystallites. In turn, elimination of the voids would reduce the jump distance and/or increase the activation energy, and both of these changes would decrease the observed diffusion coefficient. The heat-treated PG's used in this study were not nearly as well graphitized as heat-treated PG studied by WMB.

The activation energy for diffusion across the crystallite surfaces consists of two terms: that for "untrapping" and that for motion across the crystallite surface. The untrapping energy should be called the energy to form a crystallite surface atom ($\Delta G^*_{f<a>}$), and it should be related to the bond energy of the metal for carbon and the size of the metal atom. Conversely, the energy for motion across the crystallite ($\Delta G^*_{m<a>}$) will primarily depend upon the crystallite separation and the metal atom size. From all the above discussion, the diffusion coefficient parallel to the deposition plane can be expressed as

$$D_{<a>} = k_a L_a^2 \nu_0 \exp(-\Delta G^*_{f<a>} - \Delta G^*_{m<a>}/RT)$$

As noted above, k_a is a numerical factor related to the number of different jumps possible, L_a is the crystallite diameter and jump distance for the diffusion, and ν_0 is the vibration frequency.

The mechanism for diffusion perpendicular to the layer planes will now be discussed. Diffusion in this direction must occur down the crystallite edges for the reasons given above. Between the crystallites within the minor cones and along the minor cone boundaries, the relative misorientation is slight, which probably results in a low degree of disorder. Large lattice strains would be required for metal diffusion along these boundaries, making the activation energy for diffusion much larger here than at the major cone boundaries where the misorientation is greatest. Because the pre-exponential factor for all these paths will be about the same, the diffusion rate at a given temperature will be greatest for the path of least activation energy, which is the primary cone boundary. Primary cone boundary diffusion is demonstrated in the autoradiographs of diffusion perpendicular to the layer planes and in the observation that partial graphitization decreases the diffusion coefficient measured in that direction. Further evidence for this portion of the model is given by the effect of graphitization on $D_{\langle c \rangle}$. Partial graphitization results in a decrease in the misorientation angle between crystallites and a decrease in $D_{\langle c \rangle}$. These observations are consistent with the arguments just given concerning diffusion rates in regions of differing misorientations.

Diffusion perpendicular to the layer planes is complicated by a high lateral diffusion rate parallel to them; however, it can be shown (see Appendix) that

$$D_{\langle c \rangle} \propto k D_b$$

where l is the major cone boundary thickness, D_b the boundary diffusion coefficient, and $D_{\langle c \rangle}$ the value obtained by treating the observed profile as being the result of diffusion into a semi-infinite solid under constant surface composition conditions. This proportionality between D_b and $D_{\langle c \rangle}$ is important: it shows that the activation energy computed from the $D_{\langle c \rangle}$ data is the same as that for D_b . It also states that, although the scatter in the diffusivity data is dominated by errors in temperature, some contribution to this scatter can come from having experimental conditions that do not meet the assumptions used in the derivation given in the Appendix. These assumptions are that the observed profile can be represented by

$$\frac{C}{C_s} = \operatorname{erfc} \frac{x}{2\sqrt{Dt}}$$

and that constant surface composition conditions existed throughout the diffusion anneal. If the tracer reservoir on the surface is depleted during the experiment, one of the boundary conditions used in the derivation will be violated.

It is reasonable to assume that the jump distance for diffusion perpendicular to the layer planes is equal to the layer plane separation. The edges of each layer plane have a large number of unsatisfied bonds; traps can thus be expected to exist at each layer plane. Such trapping yields a jump distance of 3.4 Å, which is virtually independent of the crystallite thickness. If the jump distance is independent of crystallite thickness, the activation energy for diffusion perpendicular to the layer planes would apparently have to increase in the graphitized material to account for the observed decrease in $D_{\langle c \rangle}$ with graphitization.

There was no significant increase in activation energy; therefore, the cause of the decrease in $D_{\langle c \rangle}$ will have to be found elsewhere. In the Appendix, it is shown that

$$D_{\langle c \rangle} \propto l D_b$$

It is reasonable to expect that the width of the boundary containing the less organized carbon would decrease slightly upon graphitization due to the decrease in misorientation. A one-half decrease in l would account for the slight decrease in D_{0-c} for the partially graphitized PG. A gradual increase in the activation energy for diffusion perpendicular to the layer planes with increasing graphitization is to be expected, however, because the major cone boundaries will become regions of less disorder as the misorientation decreases and these boundaries will approach the state of the minor boundaries. This state was not reached in the graphitizing heat-treatment used in this study.

From the above discussion, the observed diffusion coefficient perpendicular to the layer planes can be written

$$D_{\langle c \rangle} = k_c d_{0002}^2 \nu_0 \exp(\Delta G^*_{m\langle c \rangle}/RT) \propto l D_b$$

where l is the boundary thickness, k_c a numerical factor related to the number of different jump directions, d_{0002} the interlayer spacing, $\Delta G^*_{m\langle c \rangle}$ the standard Gibbs free energy for motion perpendicular to the layer planes, and ν_0 the vibration frequency.

The ratio of the pre-exponential factors for diffusion parallel and perpendicular to the layer planes should be equal to the ratio of the numerical factors times the square of the inferred jump distances:

$$\frac{D_{o-a}}{D_{o-c}} = \frac{k_a L_a^2}{k_c d_{0002}^2}$$

Assuming $k_a \approx k_c$, and taking data for as-deposited PG from Table 15,

$$\frac{D_{o-a}}{D_{o-c}} = \frac{3.2 \times 10^2}{1.2 \times 10^{-2}} = 2.7 \times 10^4$$

$$\frac{L_a^2}{d_{0002}^2} = \left(\frac{250}{3.4}\right)^2 = 0.54 \times 10^4$$

Similarly, for heat-treated PG

$$\frac{D_{o-a}}{D_{o-c}} = \frac{1.8 \times 10^3}{6.5 \times 10^{-3}} = 2.5 \times 10^5$$

$$\frac{L_a^2}{d_{0002}^2} = \left(\frac{600}{3.4}\right)^2 = 0.31 \times 10^5$$

For the as-deposited PG's, the ratios differ by a factor of 5 and for the heat-treated PG's the ratios differ by a factor of 8. If the values of D_{o-c} for the as-deposited and heat-treated PG's were normalized to the same primary cone boundary thickness, the agreement would be improved. In the model discussed above, it was postulated that the primary cone boundary thickness was decreased

by one-half during the graphitizing heat-treatment; therefore, normalization of the D_{O-C} terms would require multiplying D_{O-C} (HT) by 2. With this factor of 2, the ratios of the D_O 's and the ratios of the squares of the jump distances would differ from each other by a factor of 5. The agreement could be improved further if k_a were about $5 k_c$. These numerical factors are proportional to the reciprocal of the number of different jump directions from a particular site (136), and estimates of these factors are given below.

For diffusion perpendicular to the deposition plane, an atom diffusing in the primary cone boundary can jump in four different directions: to the next layer plane above its position, to the plane below its position, to the left of its position, or to the right of its position. All of these jumps are of equivalent size. Conversely, for diffusion parallel to the layer planes, the number of different, equivalent jumps is restricted to two: forward or backward one crystallite diameter. Jumps to either side are possible, but their distance is much smaller than the crystallite diameter jump distance, and therefore, they are not of consequence in the diffusion process. These arguments yield $k_a = 2 k_c$. Another factor of two might be obtained from arguments concerning the vibration frequencies; however, the D_O 's are not known with sufficient accuracy to warrant such refinements. The standard deviation of Q_c is about 6%, a slight increase in Q_c for Nb would also reduce the pre-exponential factor ratio and tend to improve the agreement.

E. Discussion of Grain Boundary Diffusion Theories

Grain boundary diffusion in metals has been studied rather extensively (136,138 through 141) and LeClaire (142) has recently reviewed the subject. All the grain boundary theories presented to date have been developed for concurrent boundary and volume diffusion in an otherwise isotropic solid and all predict that the logarithm of the concentration should decrease approximately as the first power of the distance. When grain boundary diffusion is important this dependency is observed for metals diffusing in polycrystalline metals (143). In contrast with these results, the data of this investigation and those of Wolfe, McKenzie and Borg definitely show that this dependency is not observed for metals diffusing in PG.

The reason for this difference between grain boundary diffusion in metals and in PG lies in the lack of volume diffusion and the peculiar, anisotropic defect structure of PG. Diffusion in PG parallel to the layer planes is equivalent to diffusion on many parallel planes, each with a line source. With modifications of the concentration terms, this situation is equivalent to linear diffusion from a plane into a solid (144). The same could be said for diffusion within the primary cone boundaries perpendicular to the layer planes except for the lateral diffusion parallel to the layer planes. These sinks extending away from the cone boundaries are supplied at the rate of diffusion down the boundary and, because only lateral and cone boundary diffusion can occur, the concentration profile measured by sectioning techniques is simply proportional to the boundary concentration profile (see Fig. 27). Therefore, the measured diffusion coefficient

is approximately proportional to the boundary diffusion coefficient. The mathematics of this discussion are given in the Appendix.

F. Discussion of the Model and Comparison with the Data of Wolfe, McKenzie and Borg

The data of Wolfe, McKenzie and Borg are in general agreement with the data of this investigation. While WMB studied the diffusion of several different metals in PG, the present study concentrated on the diffusion of one metal in several different PG's. A comparison of all the data shows that the diffusion of metals in PG is dependent upon the kind of metal, the direction of diffusion, and the crystallite diameter, but not upon the microstructure. The model proposed by WMB was based primarily upon entropy arguments concerning the large values of D_{0-a} . These arguments led them to propose that the jump distance was approximately equal to the crystallite dimension in the direction of diffusion. Their model is similar to that proposed here, except for the jump distance perpendicular to the layer planes. The WMB model assumes this jump distance to be the crystallite thickness, whereas in the model proposed in the present investigation, the jump distance perpendicular to the layer planes is the inter-layer spacing.

Some of the results for WMB's work and this investigation are summarized in Table 16, together with other information. First, it may be seen that $D_{0-a} > D_{0-c}$ in all cases, with the ratio being about 10^4 for Nb diffusing

Table 16
COMPARISON OF DATA FROM THIS INVESTIGATION WITH THOSE OF WOLFE, MCKENZIE AND BORG

Diffusing Metal	Q_a (k cal/mole)	Q_c (k cal/mole)	Compounds Formed	$-\Delta H_{298}$ (k cal/mole)	Metal Radius (Å)	$Q_a +$ ΔH_{298} (k cal/mole)	$Q_c +$ ΔH_{298} (k cal/mole)	PG Condition	$D_{o(a)}$ (cm ² /sec)	$D_{o(c)}$ (cm ² /sec)	$\frac{D_{o(a)}}{D_{o(c)}}$
Nb	96.2	73.1	NbC	.9	1.46 ^(b)	60	50	AD	3.2×10^2	1.2×10^2	2.7×10^4
Nb	96.2	73.1			1.80 ^(b)	100	69	HT	1.6×10^3	6.5×10^{-3}	2.5×10^5
Ta	145.0	114.7	TaC	45	1.52 ^(b)	65	69	AD	1.3×10^5	2.5	5.4×10^4
U	115.0	129.5	UC	40	1.52 ^(b)	65	69	AD	6.8×10^3	3.9×10^2	1.75×10^1
			U_2C_3	72							
			UC_2	40							
Si	47.2	53.3	-	-	1.24 ^(c)	-	-	AD	1.0×10^2	2.2	4.6×10^1
Ag	64.3	-	-	-	1.17 ^(c)	-	-	AD	9.3×10^3	-	-
Ra	99.4	-	-	-	1.43 ^(c)	-	-	AD	1.2×10^4	-	-

(a) Reference 54
 (b) Reference 108
 (c) Reference 106

in as-deposited PG and somewhat less for WMB's data on Th, U, and Ni. The model proposed in this study requires that, to a first approximation, this ratio must be constant for a particular PG, regardless of the diffusing metal. This ratio is not constant for WMB's data; however, it should be noted that D_o is very sensitive to the choice of Q , and it is possible for the ratio of D_{o-a}/D_{o-c} to vary by a factor of 10 through the choice of Q_a and Q_c . This ratio is as low as 20 for the case of U diffusing in PG, as determined by WMB. Such a low value cannot be explained by a smaller crystallite diameter because WMB estimated that the crystallite diameter of the PG used in their investigation was about 150 Å. This diameter is somewhat smaller than the values obtained for the PG's used in this study, but the difference would only account for a factor of 2 in the ratio of the pre-exponential factors.

The relative values of the activation energies parallel and perpendicular to the layer planes also differ for the different metals studied in this investigation and that of WMB. As shown in Table 16, $Q_a > Q_c$ for Nb and Th, and for U and Ni, $Q_a < Q_c$. In the model proposed here,

$$Q_a = \Delta H_{f<a>} + \Delta H_{m<a>}$$

and

$$Q_c = \Delta H_{m<c>}$$

To a first approximation, one might expect $H_{f<a>} = H_{m<c>}$ because both represent untrapping. This approximation would make $Q_a > Q_c$ for all metals,

which is not the case for U and Ni. In light of this, the approximation concerning the activation energies does not appear to be valid.

It is also possible that $\Delta H_{f<a>}$ and $\Delta H_{m<c>}$ are related to the metal-carbon bond strength. Table 16 lists the heats of formation for the carbides of Nb, Th, and U at 298°K. As may be seen, the activation energies for diffusion are two to three times the heat of formation of the carbides, indicating that either the metal atoms are more tightly bound in the PG structure than in the carbide or that the contribution of strain energy to the activation energies for diffusion is large. Both effects probably contribute to the difference. The high value of Q_c for Th in PG is very likely related to its large size. In the model developed by this investigation, diffusion parallel to the deposition plane occurs by atoms moving between the crystallites. Thus, the much larger Th atom should have a higher motion energy for that process than do the smaller atoms.

As listed in Table 16, the activation energies for diffusion of Ni and Ag in PG are much lower than those of U, Th, and Nb. Ni and Ag do not form carbides and their activation energies for diffusion are about equal to those for the carbide formers after the absolute value of the heat of formation of the carbide has been subtracted. This observation is in agreement with the model, in that the activation energy for diffusion of a carbide former in PG should be larger than that of a non-carbide former by the heat of formation of the carbide because the "untrapping" energy for a carbide former should include the heat of formation of the carbide. An apparent exception to this argument is the value of 99 kcal/mole for diffusion of Ra parallel to the deposition plane in PG. This value is

larger than that observed for Nb but the atom sizes differ appreciably. The atom size of Ra is not well known; however, the atom radius of Ra may be estimated from the atom sizes of Kr and Xe, using the values given in Cullity (106) as 2.5 Å. An atom size this large would result in a high activation energy for diffusion parallel to the deposition plane for the same reasons given above for the Th diffusion.

G. Relevance of Model to Diffusion in Other Graphites and Pyrolytic Graphites

The model for diffusion in PG developed in this investigation should have application to metal diffusion in other forms of graphite and in the recently improved forms of PG. Some of the model's implications for diffusion in the other graphites will be given here.

As discussed in Chapter III, conventional synthetic graphites consist of well graphitized regions surrounded by somewhat less graphitized regions that are derived from the carbonization and graphitization of the petroleum-coke binder. Conventional graphites contain a spectrum of crystallite sizes from over 1000 Å to less than 50 Å, with the well graphitized regions having the larger crystallites and the binder regions the smaller. The average diameter of crystallites is about 500 Å (27). Conventional graphites also possess a spectrum of pore sizes, some of which are accessible to high pressure Hg porosimetry. Because the easily sheared layer planes tend to lie parallel to the flow lines, some preferred orientation exists if the graphite body has been subjected to hot working.

Because the activation energies parallel and perpendicular to the layer planes are comparable and the pre-exponential factor for diffusion parallel to the layer planes is large, the diffusion rate parallel to the layer planes will dominate in conventional graphite. This effect would be accentuated in conventional graphite because of large average crystallite size. Another complication would arise due to the wide spectrum of crystallite sizes which would result in an even greater spread in the pre-exponential factor. Furthermore, there would definitely be an anisotropy of diffusion related to the layer plane texture of the graphite. However, the ratio of the diffusivities perpendicular and parallel to the texture would be considerably less than in PG because conventional graphites do not have the high degree of layer plane texture possessed by PG.

If diffusion parallel to the layer planes is the dominate mechanism for metal diffusion in conventional graphites, then one might expect to observe the same activation energy as that for diffusion in PG parallel to the deposition plane. There are, however, additional complications. It is not likely that conventional graphites would possess the uniform layer plane voids found in PG because of the differences in manufacture. When the volatile elements are driven off during the manufacture of conventional graphite, the carbon-foreign element bonds are broken and new carbon-carbon bonds are formed. Many of these form what are called cross-links (57) which are bonds that do not form part of the layer plane network but extend away from it in different directions. These bonds interfere with the graphitization process and also would interfere with the motion

of foreign atoms diffusing over the surfaces of the crystallites. In addition, the purity of conventional graphites is generally less than that of PG, with the foreign atoms tending to congregate at the edges of the crystallites for the reasons discussed earlier. Because these foreign atoms occupy the same places that the diffusing atoms should occupy, some interference is inevitable. For these reasons, the activation energy for metal diffusion in conventional graphites should be somewhat greater than that for diffusion parallel to the deposition surface in PG.

Examination of WMB's data (Table 3) indicates that the diffusion of U-232 in both National Carbon ZTA graphite (high density) and Speers S700 graphite (low density) follows the above description. The pre-exponential factors are two orders of magnitude greater than the pre-exponential factor parallel to the PG deposition plane and the activation energies are slightly higher than the activation energy parallel to the deposition plane in PG. The anisotropy of Th diffusion in ZTA also fits the above discussion.

None of the other data for metal diffusion in graphites listed in Chapter II shows activation energies as high as those found in this investigation or by WMB for the same metals studied. It should be noted, however, that these data generally represent very questionable results derived from two or three points on the concentration profiles with data at three or so temperatures used to determine activation energies. As discussed earlier, the studies of the migration of fission fragments are additionally complicated by radiation damage and the presence of other elements; however, the generally lower activation energies are

probably indicative of mass transport within or along the pores rather than between the individual crystallites, as in PG. All of the elements listed in Table 2 have rather low melting temperatures and high vapor pressures, which would tend to enhance the pore migration mechanism.

Recent developments in PG technology have led to the production of thicker deposits with a greater uniformity of structure and less tendency toward delamination than were previously available. The differences between these newer PG's and the ones used in this study are differences only in quality and uniformity. Because it was shown that metal diffusion in PG does not depend upon microstructure but rather upon crystallite size, metal diffusion coefficients in the new PG's would not differ appreciably from those found in this study or that of WMB. Any variation should be predictable on the basis of crystallite variations, as described above.

H. Comments Concerning Diffusion-Alloying in PG

One of the purposes of this investigation was to consider the possibility of diffusion-alloying PG with metals. From the diffusion data obtained in this study and that of WMB, it is evident that the diffusion coefficients of many metals in PG are high enough to allow appreciable penetration within reasonable times. However, the concentrations involved are very small ($\sim 10^{-7}$ gm/cm³) and the effect of the alloy element might be small. It was shown that the diffusing metal atoms are restricted to the crystallite surface and, since the mechanical (5) and

oxidation (15) behavior of PG is largely controlled by the interaction of the crystallites and their surfaces, these few atoms concentrated on the crystal-lite surfaces could appreciably alter some of the properties of PG. The size of the effect would have to be determined by experiment.

Chapter X

SUMMARY

The purposes of this investigation were to determine the fundamental mechanisms of metal diffusion in PG, to increase the understanding of the structure of PG through these studies, and to examine the possibility of diffusion-alloying PG. A literature survey revealed that, with the exception of recent data of Wolfe, McKenzie, and Borg (17) and possibly that of Hennig (18), there were virtually no reliable data for the diffusion of metals in graphites. This lack of data was one of the underlying reasons for the investigation.

In the initial studies, diffusion reactions of Re with PG were studied and a metastable carbide of Re was discovered. This carbide could not be produced in quantity, but information regarding its phase reactions with Re metal and its crystal structure was obtained. The crystal structure of the carbide was found to be simple cubic with a unit cell edge of $2.8\pm A$. However, because the atom positions within the unit cell could not be determined, the stoichiometry of the carbide is not known. The largest quantities of the carbide were produced in diffusion couples by a eutectic reaction with Re. The eutectic temperature between Re and Re carbide was estimated to be $\sim 2000^{\circ}C$ ($\pm 200^{\circ}C$), compared with $2480^{\circ}C$ for the eutectic temperature between Re and C (103).

The techniques for studying metal diffusion in PG were developed with a radioisotope of Re, but higher specific activity was required than was readily

available with Re and a carrier-free isotope of Nb was chosen to continue the study of metal diffusion in PG.

The diffusion coefficients of Nb in PG were measured between 1450 and 1950°C in three different kinds of PG. The PG's were chosen to be representative of substrate nucleated, combination substrate and regeneratively nucleated, and regeneratively nucleated microstructures. The diffusion coefficients were determined for two conditions of each PG (as-deposited and partially graphitized) and in the two different "crystallographic" directions of PG (parallel and perpendicular to the deposition surface). Autoradiography was employed to observe the distribution of the diffusing atoms.

The structure of each PG was characterized by the application of many techniques of metallography, x-ray diffraction, and density determinations. With these techniques, the structure was described in terms of:

- Metallographic structure at high and low magnification
- Structure observed by transmission electron microscopy
- Stacking error probability or degree of graphitization, p
- Crystallite thickness and diameter, L_c and L_a
- Degree of preferred orientation
- Orientation dependence of structural parameters, p and L_a
- Submicroscopic void size, determined from small angle scattering of x-rays
- Displaced volume density and x-ray density

A mathematical analysis of diffusion in layered structures was made, and correlations between the diffusion and structural parameters were noted.

The diffusion coefficients for Nb in PG in a particular direction could be represented by a single activation energy and variable pre-exponential factors. The activation energy was independent of the PG microstructures and states of graphitization used in this study. The activation energy for Nb diffusion in PG parallel to the deposition surface was 96.2 kcal/mole while that for Nb diffusion perpendicular to the deposition surface was 73.1 kcal/mole

The pre-exponential factors (D_0) for a given direction in the as-deposited PG did not differ appreciably, regardless of microstructure. There was, however, a significant change in the D_0 's brought about by the graphitizing heat-treatment. Parallel to the deposition plane the pre-exponential factors (D_{0-a}) were all approximately $3.2 \times 10^2 \text{ cm}^2/\text{sec}$ for the as-deposited PG's and $1.8 \times 10^3 \text{ cm}^2/\text{sec}$ for the heat-treated materials. For diffusion perpendicular to the deposition plane, these factors (D_{0-c}) were approximately $1.2 \times 10^{-2} \text{ cm}^2/\text{sec}$ for the as-deposited PG's and $6.5 \times 10^{-3} \text{ cm}^2/\text{sec}$ for the heat-treated PG's. There were slight differences in the pre-exponential factors in each direction among the various PG's but the differences were of the order of the uncertainty in the D_0 's

Autoradiographs taken perpendicular to the mass flux for diffusion perpendicular to the deposition plane demonstrated that diffusion perpendicular to the deposition plane occurs principally along the primary cone boundaries which are the regions of greatest layer plane misorientation. Autoradiographs taken

perpendicular to the deposition plane for diffusion parallel to the deposition plane showed a uniform distribution of radioactivity, except for occasional streaks caused by delamination.

A consideration of the possible mechanisms for diffusion within the crystallites showed that such mechanisms are very unlikely except for the smallest atoms: B, H, O, and N. From valence considerations, none of these will substitute for carbon in the layer planes, but an interlayer migration mechanism is possible. All other atoms are too large to diffuse within the crystallites except in situations in which lamellar compounds form. Evidence was given that lamellar compounds did not form during this investigation.

Considerations of the possible mechanisms external to the crystallites led to the following conclusions:

- Traps exist along the layer plane edges and at vacancy clusters in the top and bottom layer planes of the crystallites
- Primary cone boundaries contain regions of greater misorientation than do secondary cone boundaries
- Atoms diffusing on the top layer plane of a crystallite are relatively free to move, provided there is sufficient room between the crystallites
- Diffusion perpendicular to the layer planes occurs principally in the primary cone boundaries, along the paths of greatest layer plane misorientation

- Atoms diffusing perpendicular to the layer planes encounter frequent trapping sites, probably at each layer plane edge.

The above conclusions and an analysis of the ratios of the pre-exponential factors for the different directions and conditions revealed that *the fundamental jump distance parallel to the deposition plane is the crystallite diameter while the jump distance perpendicular to the layer planes is the layer plane separation distance.* The following equations resulted when these conclusions were combined with elementary interstitial diffusion theory:

$$D_{\langle a \rangle} = k_a L_a^2 \exp(-\Delta G^*_{\langle a \rangle})$$

$$D_{\langle c \rangle} = k_c d_{0002}^2 \exp(-\Delta G^*_{\langle c \rangle})$$

where L_a is the crystallite diameter, d_{0002} the interlayer spacing, $G^*_{\langle a \rangle}$ and $G^*_{\langle c \rangle}$ the standard free energies of activation for the processes parallel and perpendicular to the deposition plane, respectively, and k_a and k_c numerical factors related to the number of different jump directions for a given position. A consideration of the different possible jumps led to the relation $k_a = 2 k_c$.

An analysis of metal diffusion down the primary cone boundaries of PG with lateral diffusion occurring only parallel to the deposition surface yielded

$$D_{\langle c \rangle} \propto t D_b$$

where f is the primary cone boundary thickness, D_b the boundary diffusion coefficient, and $D_{\langle c \rangle}$ the measured diffusion coefficient. The analysis required that $D_{\langle c \rangle}$ be obtained by treating the composition profiles as if they were the result of diffusion into a semi-infinite solid under constant surface composition conditions. This relationship explained how $D_{\langle c \rangle}$ was decreased with partial graphitization without any change in $\Delta G^*_{\langle c \rangle}$. This relationship, together with the $k_a = 2 k_c$ relationship, also provided quantitative confirmation of the equations given above relating the diffusivities in the different directions to their respective jump distances.

Some apparent anomalies for Th and Ra diffusion in PG, reported by Wolfe, McKenzie and Borg (17), were explained by the model developed in this investigation, as were some of the difficulties involved in studying metal diffusion in conventional graphites. The diffusion coefficients of several metals in PG were shown to be sufficiently large to permit appreciable diffusion-alloying of PG within reasonable times; however, the efficacy of this method of alloying remains to be determined by experiment.

Appendix

MATHEMATICS OF DIFFUSION IN LAYERED STRUCTURES

Using various arguments, it was shown in Chapter IX that metal diffusion in PG occurs only over the surfaces and down the edges of the PG crystallites. Because most of the crystallites in PG lie parallel to the deposition surface, the diffusion coefficient measured parallel to the deposition surface, $D_{\langle a \rangle}$, corresponds to that parallel to the layer planes. Conversely, the diffusion coefficient measured perpendicular to the deposition surface, $D_{\langle c \rangle}$, corresponds in some fashion to a boundary diffusion coefficient, D_b . It is the purpose of this appendix to examine the relationship of $D_{\langle c \rangle}$ and D_b .

Figure 27 shows a somewhat idealized model of metal diffusion in PG perpendicular to the deposition surface. From the arguments presented in Chapter IX, the volume diffusion coefficient is essentially zero so the only paths into the PG from the surface are the major cone boundaries. Approximately perpendicular to the major cone boundaries there exist high diffusivity paths which are the surfaces of the crystallites, and they have a spacing equal to the crystallite thickness, L_c . Since L_c is very small relative to the concentration profile, the problem can be treated as if the PG were an anisotropic solid with a slab of different diffusivity extending into it.

Figure 28 shows the mathematically idealized structure which will be used to treat cone boundary diffusion in PG. The model consists of a single boundary perpendicular to the deposition surface, $2l$ units wide, and extending in the

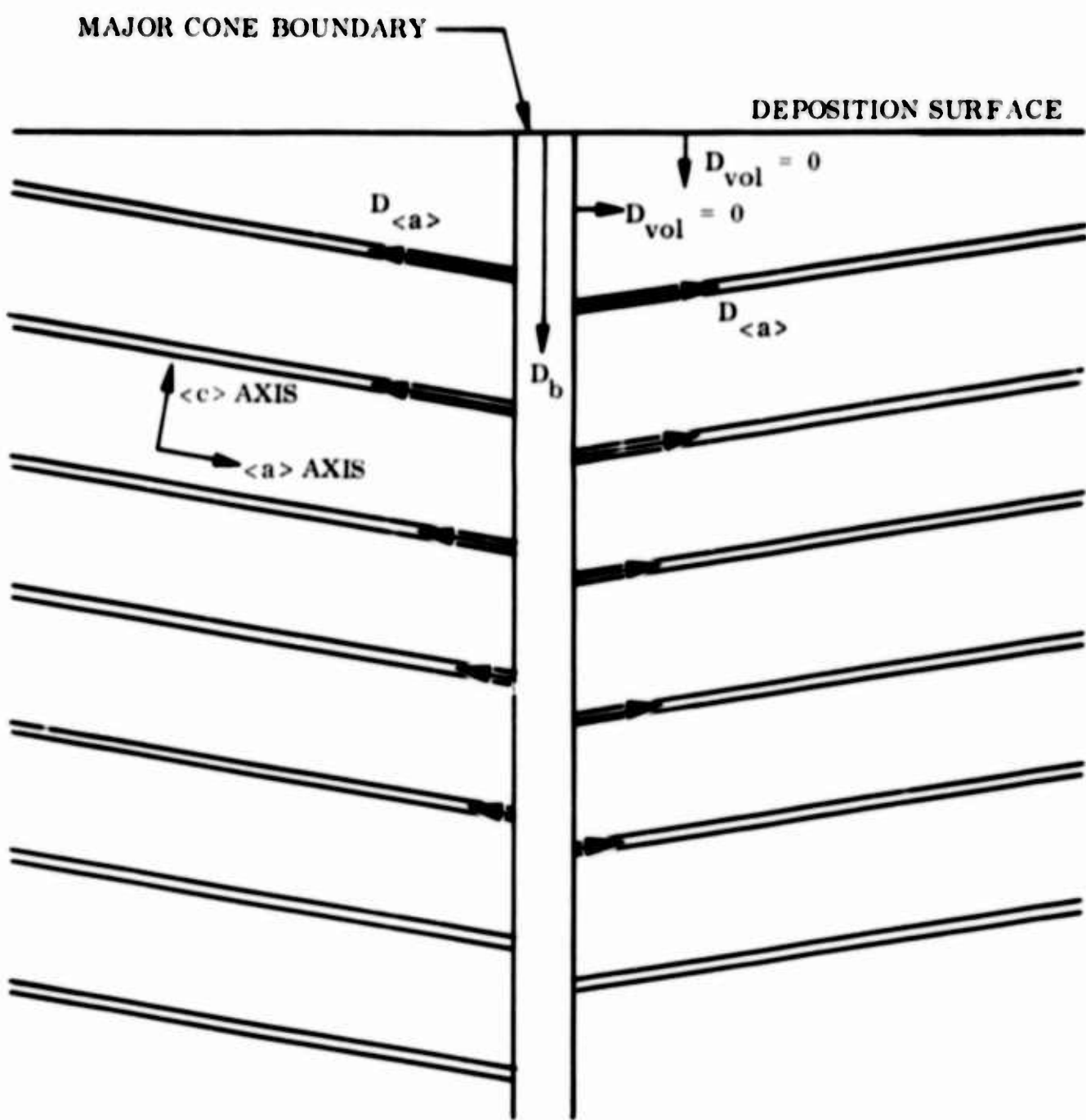


Fig. 27 Idealized Model for Diffusion Perpendicular to Layer Planes in Pyrolytic Graphite

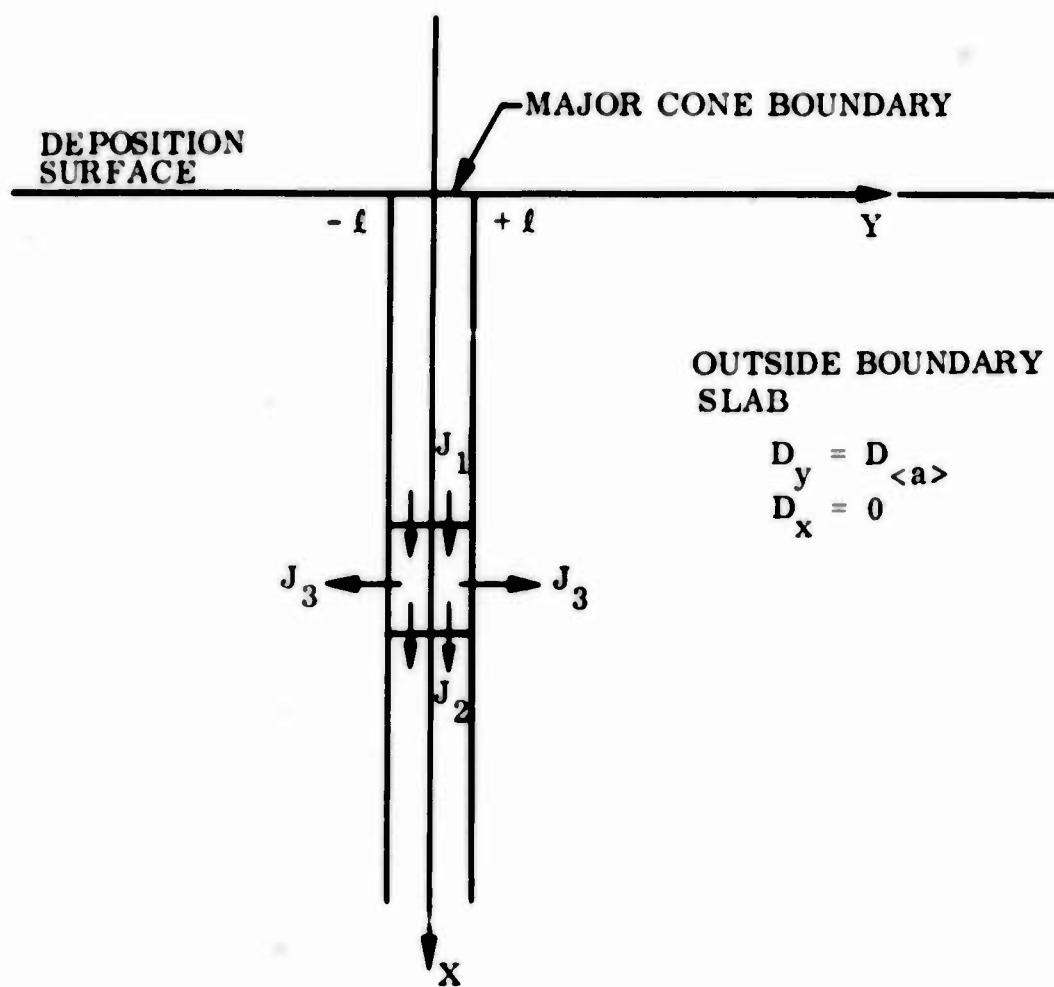


Fig. 28 Mathematical Model for Diffusion Perpendicular to Layer Planes in Pyrolytic Graphite

x-direction into a semi-infinite solid. The distance to the next cone boundary is assumed to be so large that the lateral diffusion can be treated as if the solid were semi-infinite in the y and z directions also.

If the subscript _v refers to processes outside the boundary and the subscript _b refers to processes within the boundary, then, in the quadrant containing positive x and positive y, we have two differential equations to describe the diffusion processes outlined above.

$$\begin{aligned} \text{DE 1} \quad \frac{\partial C_v}{\partial t} &= D_v \frac{\partial^2 C_v}{\partial y^2} \\ \text{DE 2} \quad \ell \frac{\partial C_b}{\partial t} &= \ell D_b \frac{\partial^2 C_b}{\partial x^2} + D_v \frac{\partial C_v}{\partial y} \Big|_{y=\ell} \end{aligned} \quad (1)$$

where $D_v \equiv D_{\langle a \rangle}$, the diffusion coefficient measured parallel to the deposition plane. Note that a term involving $\partial^2 C_v / \partial x^2$ is absent because the volume diffusivity in that direction is assumed to be zero. Assuming that there are no concentration gradients in the y-direction within the boundary,

$$\begin{aligned} C_v &= C_v(x, y, t) \\ C_b &= C_b(x, t) \end{aligned} \quad (2)$$

The initial conditions are

$$\text{IC 1} \quad C_v(x, y, 0) = 0$$

$$\text{IC 2} \quad C_b(x, 0) = 0$$

and the boundary conditions for constant surface composition conditions and semi-infinite media are

$$\text{BC 1} \quad C_b(0, t) = C_s$$

$$\text{BC 2} \quad C_v(x, \infty, t) = \left. \frac{\partial C_v}{\partial y} \right|_{y=\infty} = 0$$

$$\text{BC 3} \quad C_b(\infty, t) = 0$$

The coupling condition is

$$\text{CC} \quad C_v(x, l, t) = C_b(x, t)$$

Sectioning experiments involve the use of an average composition taken over a slice parallel to the yz plane, so we can define an average composition by

$$C(x, t) = l C_b(x, t) + \int_l^\infty C_v(x, y, t) dy \quad (3a)$$

and this can be differentiated with respect to t yielding

$$\frac{\partial C}{\partial t} = \frac{\partial}{\partial t} (l C_b) + \frac{\partial}{\partial t} \int_l^\infty C_v(x, y, t) dy \quad (3b)$$

From DE 1 and 2, and BC 2

$$\frac{\partial}{\partial t} \int_l^\infty C_v(x, y, t) dy = -D_v \frac{\partial C_v}{\partial y} \Big|_{y=l}$$

$$\frac{\partial}{\partial t} (l C_b) = l D_b \frac{\partial^2 C_b}{\partial x^2} + D_v \frac{\partial C_v}{\partial y} \Big|_{y=l}$$

Substituting into Eq. (3b) we obtain

$$\frac{\partial C}{\partial t} = l D_b \frac{\partial^2 C_b}{\partial x^2}$$

Integration with respect to x once and applying BC 2 and 3 yields

$$-l D_b \frac{\partial C_b}{\partial x} = \int_x^\infty \frac{\partial C(\eta, t)}{\partial t} d\eta$$

Integrating again,

$$l D_b C_b(x, t) = \int_x^\infty \int_t^\infty \frac{\partial C(\eta, t)}{\partial t} d\eta dt$$

Interchanging the order of integration and integrating once, we obtain

$$l D_b C_b(x, t) = \int_x^\infty \int_x^\eta \frac{\partial C(\eta, t)}{\partial t} dt d\eta$$

$$t D_b C_b(x, t) = \int_x^{\infty} (\eta - x) \frac{\partial C(\eta, t)}{\partial t} d\eta \quad (4)$$

Applying BC 1 to Eq. (4) yields

$$t D_b C_s = \int_0^{\infty} \eta \frac{\partial C(\eta, t)}{\partial t} d\eta \quad (5)$$

At this point, an approximation will be made. It was observed that the concentration profiles for Nb diffusing into PG perpendicular to the deposition surface could be represented very well by the error function complement. Because of this, we shall assume a solution to the above equation; namely

$$C(x, t) \approx C^*(x, t) = C_s^* \frac{2}{\sqrt{\pi}} \int_{\frac{x}{2\sqrt{D_c t}}}^{\infty} \exp(-s^2) ds = C_s^* \operatorname{erfc} \frac{x}{2\sqrt{D_c t}} \quad (6)$$

where C^* is the observed concentration, C_s^* is the surface composition obtained by extrapolating the data to $x = 0$, and D_c is the diffusion coefficient measured perpendicular to the deposition plane. The brackets $\langle \rangle$ around c have been omitted here for convenience. Differentiating Eq. (6) with respect to t yields

$$\frac{\partial C^*}{\partial t} = \frac{2 C_s^*}{\sqrt{\pi}} \frac{x}{4 \sqrt{D_c t}} \exp\left(-\frac{x^2}{4 D_c t}\right)$$

and from Eq. (5)

$$\ell D_b C_s \approx \int_0^\infty \eta \frac{\partial C^*(\eta, t)}{\partial t} = \frac{2C_s^* 4 D_c t}{\sqrt{\pi} 2t} \int_0^\infty \frac{\eta^2}{4D_c t} \exp\left(-\frac{\eta^2}{4D_c t}\right) \frac{d\eta}{2\sqrt{D_c t}} \quad (7)$$

$$\ell D_b C_s \approx C_s^* D_c$$

$$\ell D_b \approx \frac{C_s^*}{C_s} D_c \quad (8)$$

which demonstrates that, approximately, the boundary diffusion coefficient, D_b , is proportional to the measured diffusion coefficient.

Equation (8) is only approximate because C_s^* , the measured surface composition is a function of time. Evaluating Eq. (3a) at $x = 0$, we obtain

$$C^*(0, t) = \ell C_s + \int_{-\ell}^0 C_v(0, y, t) dy$$

$$C^*(0, t) = \ell C_s + f(t)$$

But, the approximation given by Eq. (6) assumes

$$C^*(0, t) = C_s^*$$

which is not a function of time. Thus, the approximation given by Eq. (6) is not valid near $x = 0$.

$C^*(0,t)$ can be evaluated at $x = 0$ because

$$C_b(0,t) = C_s = C_v(0,l,t)$$

$$C_v(0,y,t) = C_s \operatorname{erfc} \frac{y}{2\sqrt{D_v t}}$$

therefore

$$C^*(0,t) = lC_s + 2\sqrt{D_v t} \int_{l/2\sqrt{D_v t}}^{\infty} C_s \operatorname{erfc} \frac{y}{2\sqrt{D_v t}} \frac{dy}{2\sqrt{D_v t}}$$

$$C^*(0,t) = lC_s + C_s \frac{2\sqrt{D_v t}}{\sqrt{\pi}} \left(\exp(-l^2/4D_v t) - l \operatorname{erfc} \frac{l}{2\sqrt{D_v t}} \right)$$

The size of l is very small, being of the order of a few Å, while $2\sqrt{D_v t}$ is of the order of 10^6 Å. Therefore

$$C_s^* = C(0,t) \cong lC_s + 2C_s \sqrt{\frac{D_v t}{\pi}} \quad (9)$$

Applying Eq. (9) to Eq. (8)

$$lD_b \cong \frac{lC_s + 2C_s \sqrt{\frac{D_v t}{\pi}}}{C_s} D_c$$

$$lD_b \cong l + 2\sqrt{\frac{D_v t}{\pi}} D_c$$

$$D_c \approx \frac{l}{l + 2\sqrt{\frac{D_v t}{\pi}}} D_b$$

But, $l \ll \sqrt{D_v t}$, therefore

$$D_c \approx \frac{l}{2\sqrt{\frac{D_v t}{\pi}}} D_b \quad (10)$$

This result is still only approximate because it is based upon the assumption that C_s^* is not a function of t , and Eq. (9) shows that C_s^* is a function of time. In any case, all of the above derivations demonstrate that

$$D_c \propto l D_b$$

The physical significance of this analysis is that the average composition near $x = 0$ continues to increase as material diffuses out the first lateral paths, but beyond $x = 0$ somewhere, the approximation given by Eq. (6) adequately represents the data. An exact solution to the differential equations describing the situation was not found and the above approximation was made because Eq. (6) represented the data very well over virtually all of the concentration profile. As noted in the body of the text, the initial concentration points were greater than the extrapolated value of C_s and this was attributed to a lack of perfect resolution of the interface with the lapping technique. It is clear from this analysis that part of the extra concentration at the very beginning of the profile is due to the results shown in Eq. (9).

The differential equations and boundary conditions given above can also be approached by the method of the Laplace transform. The following discussion, due to Professor J. C. Shyne, uses Laplace transforms, but, unfortunately the inverse of the last transform is not available. This approach is presented here because the result is capable of being numerically evaluated; however, this numerical evaluation has not been carried out.

The equations and conditions are as before.

Transforming first with respect to t :

$$\mathcal{L} t = s$$

<u>Boundary Condition</u>		<u>Transformed Boundary Condition</u>
[1] $C_v(x, y, t)$	→	$\bar{C}_v(x, y, s)$
[2] $C_b(x, t)$	→	$\bar{C}_b(x, s)$
[3] $C_b(\infty, t) = 0$	→	$\bar{C}_b(\infty, s) = 0$
[4] $C_b(x, t) = C_v(x, l, t)$	→	$\bar{C}_b(x, s) = C_v(x, l, s)$
[5] $C_v(x, \infty, t) = 0$	→	$\bar{C}_v(x, \infty, s) = 0$
[6] $C_b(x, 0) = 0$	→	$\bar{C}_b(x, 0) = 0$
[7] $C_v(x, y, 0) = 0$	→	$\bar{C}_v(x, y, 0) = 0$
[8] $C_b(0, t) = C_s$	→	$\bar{C}_b(0, s) = C_s/s$

Transforming the differential equations, DE 1 and DE 2, with respect
to t

$$s \bar{C}_v(x, y, s) - C_v(x, y, 0) = D_v \frac{\partial^2 \bar{C}_v(x, y, s)}{\partial y^2}$$

$$s \bar{C}_b(x, s) - C_b(x, 0) = D_b \frac{\partial^2 \bar{C}_b(x, s)}{\partial x^2} + \frac{D_v}{l} \frac{\partial \bar{C}_v(x, l, s)}{\partial y} \quad \Big|_{y=l}$$

Applying conditions [6] and [7] above

$$s \bar{C}_v(x, y, s) = D_v \frac{\partial^2 \bar{C}_v}{\partial y^2} \quad (11)$$

$$s \bar{C}_b(x, s) = D_b \frac{\partial^2 \bar{C}_b}{\partial x^2} + \frac{D_v}{l} \frac{\partial \bar{C}_v}{\partial y} \quad \Big|_{y=l} \quad (12)$$

Now, transforming with respect to x :

$$\text{let } x = r$$

<u>Boundary Conditions</u>		<u>Transformed Boundary Condition</u>
[1] $\bar{C}_b(x, s)$	\rightarrow	$\bar{C}_b(r, s)$
[2] $\bar{C}_v(x, y, s)$	\rightarrow	$\bar{C}_v(r, y, s)$
[3] $\bar{C}_v(x, \infty, s) = 0$	\rightarrow	$\bar{C}_v(r, \infty, s) = 0$
[4] $\bar{C}_v(x, s) = \bar{C}_v(x, l, s)$	\rightarrow	$\bar{C}_b(r, s) = \bar{C}_v(r, l, s)$

Transforming Eqs. (11) and (12) with respect to x

$$s \bar{\bar{C}}_v(r, y, s) = D_v \frac{\partial^2 \bar{\bar{C}}_v(r, y, s)}{\partial y^2} \quad (13)$$

$$s \bar{\bar{C}}_b(r, s) = D_b \left[r^2 \bar{\bar{C}}_b(r, s) - \bar{C}_b(o, s) - \frac{\partial \bar{C}_b(o, s)}{\partial x} \right] + \frac{D_v}{l} \frac{\partial \bar{\bar{C}}_v(r, l, s)}{\partial y} \quad (14)$$

Now

$$\bar{C}_b(o, s) = \frac{C_s}{s}$$

and

$$\frac{\partial C_b(o, s)}{\partial x} = \varphi(s)$$

where $\varphi(s)$ must be determined later.

Substituting for $C_b(o, s)$ and $\partial C_b(o, s)/\partial x$ into Eqs. (13) and (14):

$$s \bar{\bar{C}}_b = r^2 D_b \bar{\bar{C}}_b - D_b \frac{r C_s}{s} - D_b \varphi(s) + \frac{D_v}{l} \frac{\partial \bar{\bar{C}}_v(r, l, s)}{\partial y}$$

$$s C_v = D_v \frac{d^2 \bar{\bar{C}}_v}{dy^2}$$

Rearranging:

$$\frac{\partial \bar{\bar{C}}_v(r, \ell, s)}{\partial y} = \frac{\ell}{D_v} \left[(s - r^2 D_b) \bar{\bar{C}}_b + D_b \frac{r C_s}{s} + D_b \varphi(s) \right] \quad (15)$$

$$\frac{d^2 \bar{\bar{C}}_v}{dy^2} - \frac{s}{D_v} \bar{\bar{C}}_v = 0 \quad (16)$$

A solution for Eq. (16) is

$$\bar{\bar{C}}_v = A \exp\left(+\sqrt{\frac{s}{D_v}} y\right) + B \exp\left(-\sqrt{\frac{s}{D_v}} y\right)$$

Since $\bar{\bar{C}}_v(r, \infty, s) = 0$, $A = 0$.

and since $\bar{\bar{C}}_v(r, \ell, s) = \bar{\bar{C}}_b = B \exp\left(-\sqrt{\frac{s}{D_v}} \ell\right)$

$$B = \bar{\bar{C}}_b \exp \sqrt{\frac{s}{D_v}} \ell$$

and

$$\bar{\bar{C}}_v = \bar{\bar{C}}_b \exp \left(-\sqrt{\frac{s}{D_v}} (y - \ell) \right) \quad (17)$$

Now, differentiating Eq. (17):

$$\frac{\partial \bar{C}_v(r, l, s)}{\partial y} = \bar{C}_b \left(-\sqrt{\frac{s}{D_v}} \right) \exp \left(-\sqrt{\frac{s}{D_v}} (y - l) \right) \Big|_{y=l}$$

$$\frac{\partial \bar{C}_v(r, l, s)}{\partial y} = -\sqrt{\frac{s}{D_v}} \bar{C}_b$$

Substituting into Eq. (15)

$$-\sqrt{\frac{s}{D_v}} \bar{C}_b = \frac{l}{D_v} \left[(s - r^2 D_b) \bar{C}_b + D_b \frac{r C_s}{s} + D_b \varphi(s) \right]$$

$$\bar{C}_b = \frac{\frac{r C_s}{s} + \varphi(s)}{r^2 - \left(\frac{s}{D_b} - \frac{\sqrt{s D_v}}{l D_b} \right)} = \frac{\frac{r C_s}{s} + \varphi(s)}{r^2 - \gamma^2}$$

\bar{C}_b has the form

$$\frac{\frac{C_s}{s} r}{r^2 - \gamma^2} + \frac{\beta}{r^2 - \gamma^2}$$

and the inverse transform of \bar{C}_b with respect to r is:

$$\bar{C}_b(x, s) = \frac{C_s}{s} \cosh \gamma x + \frac{\varphi(s)}{\gamma} \sinh \gamma x \quad (18)$$

The function $\varphi(s)$ can now be evaluated.

$$\frac{\partial \bar{C}_b}{\partial x} = \frac{C_s}{s} \gamma \sinh \gamma x + \varphi(s) \cosh \gamma x$$

$$\frac{\partial \bar{C}_b}{\partial x} = 0 \quad \text{at} \quad x = 0$$

$$0 = \frac{C_s}{s} \gamma^2 \tanh \gamma \infty + \varphi(s) \gamma$$

Therefore

$$\varphi(s) = \frac{C_s}{s} \gamma$$

Substituting this relationship into Eq. (18) yields

$$\bar{C}_b(x, s) = \frac{C_s}{s} \exp(-\gamma x) \quad (19)$$

Transforming Eq. (17) yields

$$\bar{C}_v(x, y, s) = \frac{C_s}{s} \exp \left(-\gamma x - \sqrt{\frac{s}{D_v}} (y - l) \right) \quad (20)$$

The problem could be solved if the inverse transforms of Eqs. (19) and (20) were available. The resulting functions $C_v(x, y, t)$ and $C_b(x, t)$ would then be substituted into Eq. (3a) in order to functionally determine the observed composition-distance data. Unfortunately, the inverse transforms of Eqs. (19) and (20) are not available. An alternative approach is to express Eqs. (19) and (20) in the complex plane and evaluate them numerically; however, it was decided that this effort would not be worthwhile at present, considering that the approximation given in Eq. (6) fit the data rather well.

REFERENCES

1. A.R.G. Brown and W. Watt, Industrial Carbon and Graphite, p86, Soc. Chem. Ind., 1958.
2. A.R.G. Brown, D. Clark and J. Eastabrook, J. Less. Com. Metals, 1, 94, 1959.
3. J. Pappis and S.L. Blum, J. Amer. Ceram. Soc., 44, 592, 1961.
4. R.J. Diefendorf and E.R. Stover, Metals Progr., 81, n5, 103, 1962.
5. R.H. Bragg, D.D. Crooks, R.W. Fenn, Jr., and M.L. Hammond, Carbon, 1, 171, 1964.
6. C.A. Klein, Rev. Mod. Phys., 34, 56, 1962.
7. M.P. Lepie, Trans. Brit. Ceram. Soc., 63, 431, 1964.
8. C.A. Klein and M.P. Lepie, Solid State Electronics, 7, 241, 1964.
9. A.R. Ubbelohde and R.A. Lewis, Graphite and Its Crystal Compounds, Oxford Press, 1960.
10. F.P. Bundy, Science, 137, 1057, 1962.
11. J. Bassett, Brennstoff Chem., 22, 127, 1942.
12. Pyrolytic Graphite Engineering Handbook, Specialty Alloys Section of Metallurgical Products Department, General Electric Co., Detroit 32, Mich.
13. Products Bulletin J-FGB-2 (113.15) BPH, Minnesota Mining and Manufacturing Co., St. Paul, Minn.
14. W.V. Goeddel, Chapter 8 of Materials and Fuels for High Temperature Nuclear Engineering Applications, M.T. Simnad and L.R. Zumwalt, eds., Mass. Inst. Tech. Press, Mass., 1964.
15. I.W. Dawson and E.A.C. Follet, Proc. Roy. Soc., London, A274, 386, 1963.
16. R.O. Carlson, J. Phys. Chem. Solid, 13, 65, 1960.
- 17a. J.R. Wolfe, D.R. McKenzie, and R.J. Borg, UCRL Report 7324, Chemistry, UC-4, TID-4500 (30th Ed.), April 1964.

- 17b. J.R. Wolfe and R.J. Borg, Paper No. 163, presented at the 6th Conf. on Carbon, Univ. of Pittsburgh, Pa., June 1963.
- c. R.J. Borg, D.R. McKenzie, and J.R. Wolfe, Paper No. 159, presented at the 6th Conf. on Carbon, Univ. of Pittsburgh, Pa., June 1963.
- d. Private communications with R.J. Borg, Lawrence Radiation Laboratory, Livermore, Calif.
18. G.R. Hennig, J. Chem. Phys., 42, 1167, 1965.
19. G.J. Dienes, J. Appl. Phys., 23, 1194, 1952.
20. L. Pauling, The Nature of the Chemical Bond, Cornell Univ. Press, Ithica, N.Y., 1944.
21. M.A. Kanter, Diffusion of Carbon Atoms in Natural Graphite Crystals, Ph.D. Thesis, Illinois Institute of Technology, 1955.
22. M.A. Kanter, Phys. Rev., 107, 655, 1957; Phys. Rev., 98, 1563, 1955; and p61 of Kinetics of High Temperature Processes, W.D. Kingery, ed., John Wiley & Sons, New York, 1959.
23. C.A. Coulson, Valence, p181, Clarendon Press, Oxford, 1953.
24. G.J. Dienes and G.H. Vineyard, Radiation Effects in Solids, Interscience, Inc., New York, 1957.
25. T. Iwata, F.E. Fujita and H. Suzuki, J. Phys. Soc. Japan, 16, 197, 1961.
26. G.R. Hennig, Paper 8-2 of Progress in Nuclear Engineering, Series V, p587, McGraw-Hill Book Co., 1956.
27. R.E. Nightingale, ed., Nuclear Graphite, Academic Press, New York, 1962.
28. D.G. Schweitzer, Phys. Rev., 128, 556, 1962.
29. C. Baker and A. Kelly, Nature, 193, 235, 1962.
30. R.L. Wooley, Nature, 197, 66, 1963.
31. G.R. Hennig, Appl. Phys. Letts., 1, 55, 1962.
32. C.A. Coulson and M.D. Poole, Carbon, 2, 275, 1964.

33. C.A. Coulson, Proc. of the 4th Conf. on Carbon, p215, Pergamon Press, New York, 1960.
34. T. Moeller, Inorganic Chemistry, John Wiley & Sons, New York, 1956.
35. M.H. Feldman and G.J. Dienes, W.V. Goeddel and W. Gossen, J. Appl. Phys., 23, 1200, 1952.
36. J.C. Fisher, J. Appl. Phys., 22, 74, 1951.
37. W. Rudorff, Chapter in Advances in Inorganic Chemistry and Radiochemistry, Vol. 1, Academic Press, New York, 1959.
38. R.C. Croft, Proc. of the 3rd Conf. on Carbon, p315, Pergamon Press, New York, 1958.
39. C.T. Young and C.A. Smith, Atomic Energy Res. Report NAA-SR-232, June 1953.
40. C.T. Young, Atomic Energy Res. Report NAA-SR-247, 1953.
41. C.J. Orth, Nucl. Sci. Eng., 9, 417, 1961.
42. C.A. Smith and C.T. Young, Atomic Energy Res. Report NAA-SR-72, May 1951.
43. G.A. Cowan and C.J. Orth, Atomic Energy Res. Report A/Conf., 15/10/613, USA, June 1958.
44. D.Cubiciotti, Atomic Energy Res. Report NAA-SR-194, Oct. 1952.
45. S. Yajima, K. Shiba and M. Honda, Bull. Chem. Soc., Japan, 36, 258, 1963.
46. J. Bromley and N.R. Large, Proc. of the 5th Conf. on Carbon, p365, Pergamon Press, New York, 1962.
47. T. Nakai, S. Yajima, K. Shiba, and J. Osugi, Bull. Chem. Soc., Japan, 33, 497, 1960.
48. R.L. Loftness, Atomic Energy Res. Report NAA-SR-64, Aug. 1950.
49. J.D. Loch, J.R. Gambino and W.H. Duckworth, Amer. Inst. Chem. Eng., 2, 195, 1956

50. P.S. Kislyi and G.V. Samsanov, Sov. Phys.-Solid State (Trans.), 2, 1563, 1961.
51. J. Truitt, G.D. Alton, and C.M. Blood, Appl. Phys. Letts., 3, 150, 1963.
52. A.R. Ubbelohde, Proc. of the 3rd Conf. on Carbon, p63, Pergamon Press, New York, 1958.
53. R. Kieffer and F. Benesovsky, Hartstoffe, Springer-Verlag, 1963.
54. I.E. Campbell, ed., High Temperature Technology, John Wiley & Sons, Inc., New York, 1956.
55. J. O'M Bokris, J.L. White, and J.D. McKenzie, Physicochemical Measurements at High Temperatures, Butterworths Sci. Pub., London, 1959.
56. F.C. Whitmore, Organic Chemistry, 2 ed., Van Nostrand Co., Inc., New York, 1951.
57. R.E. Franklin, Proc. Roy. Soc., London, A209, 196, 1951.
58. J.D. Bernal, Proc. Roy. Soc., London, A106, 749, 1924.
59. P.L. Walker, Jr., Amer. Scient., 50, 259, 1962.
60. G.E. Bacon, United Kingdom Atomic Energy Authority Report AERE M/R 2702, October 1958.
61. H.P. Boehm and R. Coughlin, Carbon, 2, 1, 1964.
62. G.E. Bacon, Nature, 166, 794, 1950.
63. J. Biscoe and B.E. Warren, J. Appl. Phys., 13, 364, 1942.
64. M.W. Riley, Mat'l's in Des. Eng., 56, 113, 1962.
65. M.W. Hawkes, Metals Progr., 80, n6, 138, 1961.
66. Directory of Graphite Availability, ASD-TDR-63-853, Sept. 1963.
67. R.J. Diefendorf, Chapter in High Temperature Technology, p313, Butterworths Pub. Co. for International Union of Pure and Applied Chemistry, 1964.
68. R.J. Diefendorf, General Electric Report 60-RL-2432M, May 1960.

69. R.J. Diefendorf, J. Chim. Phys., 57, 815, 1960.
70. W.E. Sawyer, U.S. Patent No. 229,335 (1880)
71. C.J. Christensen, U.S. Patent No. 2,328,422 (1943).
72. O.J. Guentert, J. Chem. Phys., 37, 884, 1962.
73. T. Noda, M. Inagaki, and H. Kato, Bull. Chem. Soc., Japan, 35, 1471, 1962.
74. J. Pappis, Pyrographite Research and Development, final report from Raytheon Co., Waltham, Mass. to Lockheed Missiles & Space Co., 1961.
- 75 E.R. Stover, General Electric Report 61-RL-2745M, June 1961.
76. J. Coy, J. Amer. Ceram. Soc., 45, 223, 1962.
77. W.V. Kotlensky and H.E. Martens, Tech. Rept. 32-360, Jet Propulsion Lab., California Institute of Technology, Nov 1962.
78. S. Amelinck and P. Delavignette, J. Appl. Phys., 31, 2126, 1960.
79. I.M. Dawson and E.A.C. Follet, Proc. Roy. Soc., London, A253, 390, 1959.
80. B.E. Warren, J. Chem. Phys., 2, 551, 1934.
81. B.E. Warren, Phys. Rev., 59, 693, 1941.
82. R.E. Franklin, Acta. Cryst., 4, 253, 1951.
83. G.E. Bacon, Acta. Cryst., 4, 558, 1951.
84. G.E. Bacon and R.E. Franklin, Acta Cryst., 4, 561, 1951.
85. H.P. Klug and L.E. Alexander, X-ray Diffraction Procedures, John Wiley & Sons, 1959.
86. O.J. Guentert and S. Cvikevich, Proc. of the 5th Conf. on Carbon, p473, Pergamon Press, New York, 1962.
87. B.E. Warren, Proc. of the 1st and 2nd Conf. on Carbon, p49, Pergamon Press, New York, 1956.

88. C.R. Houska and B.E. Warren, J. Appl. Phys., 25, 1503, 1954.
89. B.E. Warren and B.C. Averbach, J. Appl. Phys., 23, 497, 1952.
90. B.E. Warren, J. Appl. Phys., 12, 375, 1941.
91. W.A. Rachinger, J. Sci. Instr., 25, 524, 1948.
92. O.J. Guentert and S. Cvikevich, Carbon, 1, 309, 1964.
93. R.H. Bragg and C.M. Packer, Rev. Sci. Instr., 34, 1202, 1963.
94. R.H. Bragg and C.M. Packer, Nature, 195, 1080, 1962.
95. R.H. Bragg, M.L. Hammond, J.C. Robinson, and P.L. Anderson, Nature, 200, 555, 1963.
96. Data on Hg Porosimetry Studies of PG by M.L. Hammond and K.A. Till, reported in this thesis.
97. G.A. Slack, Phys. Rev., 127, 694, 1962.
98. C.A. Klein, J. Appl. Phys., 35, 2947, 1964.
99. E.R. Stover, General Electric Report 60-RL-2564M
100. W.V. Kotlensky, Jet Propulsion Laboratory Space Program Summary, No. 37-25, Vol. IV.
101. D.B. Fischbach, Appl. Phys. Letts., 3, 168, 1963.
102. S. Glasstone, Textbook of Physical Chemistry, 2nd ed., Van Nostrand Pub. Co., New York, 1946.
103. J.E. Hughes, J. Less Com. Metals, 1, 377, 1959.
104. Catalog of Radio and Stable Isotopes, Isotope Development Center, Oak Ridge National Laboratory, Oak Ridge, Tenn.
105. Private communication with W.C. Coons, Chief Metallographer, Lockheed Missiles & Space Co., Palo Alto, Calif.
106. B.D. Cullity, Elements of X-ray Diffraction, Addison-Wesley Publ. Co., Inc., Mass., 1956.

107. C.S. Barrett, Structure of Metals, 2nd ed., McGraw-Hill Book Co., Inc., 1952.
108. P. Schwartzkopf and R. Keiffer, Refractory Hard Metals, The MacMillan Co., New York, 1953.
109. M. Hansen and K. Anderko, Constitution of Binary Alloys, McGraw-Hill Book Co., 1958.
110. R.F. Havell and Y. Baskin, J. Electrochem. Soc., 108, 1068, 1961.
111. C.P. Kempter and M.R. Nadler, J. Chem. Phys., 33, 1580, 1960.
112. A.W. Searcy and L.N. Finnie, J. Amer. Ceram. Soc., 45, 268, 1962.
113. R.M. Brick and A. Phillips, Structure and Properties of Alloys, McGraw-Hill Book Co., 1949.
114. W.C. Coons, Metals Prog., 81, n6, 83, 1962.
115. A. Taylor and H. Sinclair, Proc. Phys. Soc., London, 57, 126, 1945.
116. D.W. Scott and D.A. Sachman, Remote Time Sharing Computer System, General Electric Computer Dept., Computer Laboratory, Sunnyvale, Calif.
117. D.R. Chipman, J. Appl. Phys., 26, 1387, 1955.
118. R.H. Bragg and L.E. Copeland, AFOSR-TN60-1235, Oct 1960.
119. J. Cadek, Atomic Energy Research Establishment, GT-Brit.-AERE-Trans. 840, 1959.
120. Y. Beers, Introduction to the Theory of Error, Addison-Wesley Pub. Co., Inc., Mass., 1962.
121. M.L. Hammond, Lockheed Missiles & Space Co., Report 6-74-64-28, 1964.
122. M.P. Gomez, Self-Diffusion of Lead and Tellurium in Lead Telluride, Ph.D. Thesis, Stanford Univ., 1964. Also available as Lockheed Missiles & Space Co., Report A-034298.
123. B. Goldstein, Rev. Sci. Instr., 28, 289, 1957.
124. M.R. Nadler and C.P. Kempter, J. Phys. Chem., 64, 1468, 1960.

125. G.C. Chase and J.L. Rabinowitz, Principles of Radioisotope Methodology, Burgess Pub. Co., Philadelphia, Pa, 1962.
126. A. Guiner and G. Fournet, Small Angle Scattering of X-rays, trans. by C.B. Walker, J. Wiley & Sons, New York, 1955.
127. R.H. Bragg, Chapter in Encyclopedia of X-rays and Gamma Rays, p974, Reinhold Pub. Co., 1963.
128. R.H. Bragg, Amer. Cryst. Assoc. Ann. Meeting, Milwaukee, June 1958.
129. R.H. Bragg, M.L. Hammond, and J.C. Robinson, work in progress, Lockheed Missiles & Space Co., Palo Alto, Calif.
130. B.E. Warren, Proc. of the 4th Conf. on Carbon, p351, Permagon Press, New York, 1960.
131. R.M. Barrer, Diffusion In and Through Solids, Cambridge Univ. Press, 1941.
132. J. Crank, The Mathematics of Diffusion, Oxford, Clarendon Press, 1957.
133. R.A. Reynolds, Self-Diffusion of Zinc and Tellurium in Zinc Telluride, Ph.D. Thesis, Stanford Univ., 1965.
134. R. Sh. Malkovich, Sov. Phys. - Solid State (trans.), 1, 548, 1959.
135. W.E. Deming, Statistical Adjustment of Data, John Wiley & Sons, Inc., 1948.
136. F.G. Shewmon, Diffusion in Solids, McGraw-Hill Book Co., Inc., New York, 1963.
137. E.A. Kellet, B.P. Jackets, and B.B. Richards, Carbon, 2, 175, 1964.
138. R.T.P. Whipple, Phil. Mag., 45, 1225, 1954.
139. H.S. Levine and C.J. MacCallum, J. Appl. Phys., 31, 595, 1960.
140. T. Suuoka, Trans. Japan Inst. Metals, 2, 25, 1961.
141. A.E. Austin and N.A. Richards, J. Appl. Phys., 32, 1463, 1961.
142. A.D. LeClaire, Brit. J. Appl. Phys., 14, 351, 1963.

143. L. Slifkin, D. Lazarus and T. Tomisuka, J. Appl. Phys., 23, 1032, 1952.

144. D. Lazarus, Chapter in Solid State Physics, Vol. 10, Academic Press,
New York, 1960.